Chapter 3

The Alpha-Magnet

As will be discussed fully in Chapter 4, the beam directly out of the gun is not suitable for injection into a S-band linear accelerator section. Doing so would produce an accelerated beam with a large energy spread because of the large phase-spread the particles coming into the accelerator section would have in the absence of compression. Magnetic bunch compression is one solution to this problem, and the one which is most suitable for use with the RF gun. Indeed, the possibility of using magnetic compression, as opposed to RF bunching, is one of the attractive features of the RF gun.

The theory of magnetic compression will be discussed fully in the next chapter, along with the motivation for using an alpha-magnet. In this chapter, I will describe the alpha-magnet and derive its main properties. First, I will discuss the magnetic design of the SSRL alpha-magnet, which is an asymmetric quadrupole, and contrast this design with an alternative design, namely a Panofsky quadrupole. Second, I will present the equation of motion in an alpha magnet, and show how a scaled form of the differential equation can be used to deduce some of the magnet's properties, without integration. I will prove that the transport matrices for any alpha magnet can be expressed in terms of transport matrices for this scaled equation of motion. I will show how these latter transport matrices can be derived from fits to the results of numerical integration of the scaled equation of motion for an appropriately selected ensemble of particles. I will present the results of a calculation of alpha-magnet transport matrices to third order, along with discussion of the accuracy of the results. Having calculated matrices for a perfect alpha-magnet, I then discuss how to extend the treatment to imperfect alpha-magnets, specifically those with multipole and beam-hole-induced field errors. Finally, I present the results of experimental measurements of the SSRL alpha-magnet, including magnetic measurements and measurements of some first-order matrix elements.

3.1 Magnetic Characteristics and Design of the Alpha-Magnet

The alpha-magnet and its properties were first described by Enge[45]. It is essentially half of a quadrupole magnet, with a symmetry plane at $q_1 = 0$, i.e., with a vertical mirror plane along the longitudinal axis. This mirror plane provides the symmetry necessary to obtain quadrupole-like fields in the interior of the magnet. Figure 3.1, a simplified cross-sectional view of the alpha-magnet designed for the SSRL project, illustrates these points and anticipates the discussion to follow. Rather than inject the beam along the quadrupole axis (as might be done if the magnet where to be used as a combined-function dipole and quadrupole), the beam is injected through the "front-plate", i.e., through the iron piece that functions as an approximation to an ideal magnetic mirror-plane.

3.1.1 Asymmetric Quadrupole Design

To understand this in more detail, it is convenient to use the approximation that the permeability of iron is infinite. In this case, Maxwell's equations at a material boundary mandate that the magnetic field **H** just outside the iron be perpendicular to the iron surface. (For a full discussion of several of the points that follow, see J.D.Jackson, [31].) It follows that the iron surfaces are equipotentials of the magnetic scalar potential Φ_M, which is related to the magnetic field by

$$\mathbf{B} = \mathbf{H} = -\nabla\Phi_M, \tag{3.1}$$

where I employ Gaussian units, and use the fact that $\mathbf{B} = \mathbf{H}$ in air.

An infinitely-long quadrupole magnet is defined as one that has a magnetic field given by

$$\mathbf{B} = g(q_1\hat{q}_3 + q_3\hat{q}_1), \tag{3.2}$$

where g is the quadrupole gradient, and where $\hat{q}_1, \hat{q}_2,$ and$\hat{q}_3$ form a right-handed coordinate system (The reason for the unusual choice of coordinates—(q_1, q_2, q_3) instead of the usual (x, y, z)—is for consistency with subsequent sections of this chapter.) The

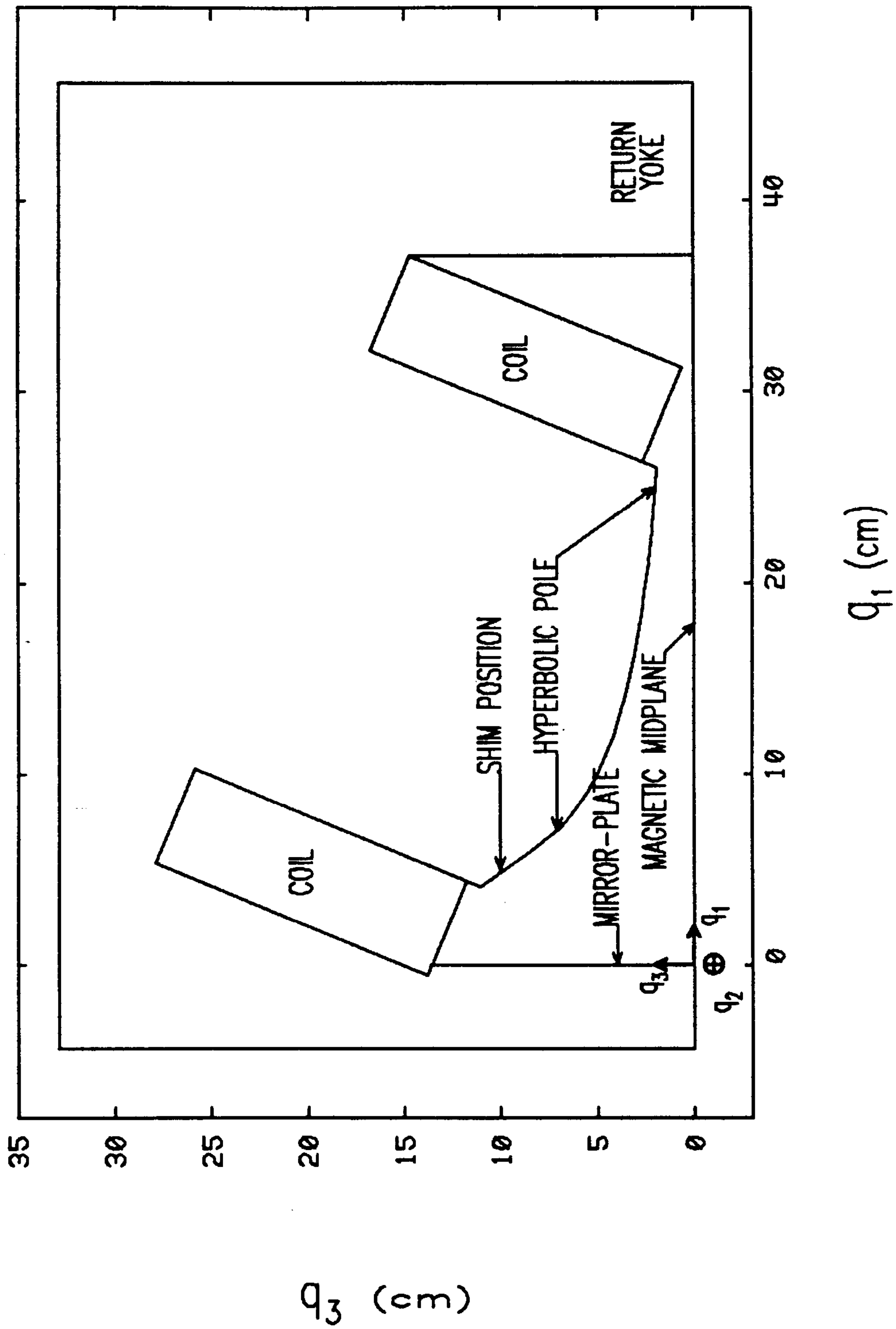

Figure 3.1: Simplified Cross-sectional view of the SSRL alpha-magnet.

reader can verify that this field satisfies Maxwell's equations, and also that it can be derived from the magnetic potential

$$\Phi_Q = -g q_1 q_3. \tag{3.3}$$

Knowing the magnetic potential necessary to produce quadrupolar magnetic fields allows one to specify the location of equipotential surfaces that will produce such a field. That is, if one arranges magnetic surfaces and suitable driving currents so as to obtain equipotentials of a quadrupolar field on the magnetic surfaces, then the region inside the boundary formed by the magnetic surfaces will contain a quadrupolar field distribution. While it is by no means essential to do so, this is typically accomplished by a four-fold symmetric arrangement of iron, where alternate poles of the magnet have the same potential except for a change in sign. Since the magnet poles are equipotentials, they must be hyperbolic in shape. (This brief exposition does not show the full power of the equipotential method in treating multi-pole fields, for which the reader should consult other sources.[6])

From the definition of the quadrupole field, it follows that the lines $q_1 = 0$ and $q_3 = 0$ are equipotentials with $\Phi = 0$. Hence, if a magnetic surface is placed along the line $q_1 = 0$ extending into $q_1 < 0$, then the field in the region $q_1 > 0$ is unchanged, since the locations and shapes of the equipotentials are unchanged. This is what is done for the asymmetric quadrupole alpha-magnet design used for the SSRL project. The reader is referred again to Figure 3.1, which exhibits the truncated hyperbolic poles and the mirror-plate along $q_1 = 0$. This design is called "asymmetric" because the hyperbola extends further horizontally than vertically, in order to obtain a large horizontal good field region. The deviation from the hyperbolic equipotential surface that is implied by truncation of the hyperbola is made up for by "shiming" the pole with additional magnetic material near the upper end of the hyperbola. This is a trail-and-error process that was carried out using the magnet code POISSON[66].

The resultant calculated gradient in the $q_3 = 0$ plane is shown in Figure 3.2, along with measurements performed on the magnet before the beam entrance/exit hole was cut in the mirror plate. Note that the way the data is normalized means that one should compare the shapes of the curves rather than the absolute agreement. I used a linearized Hall probe for these measurements (as well as those presented below),

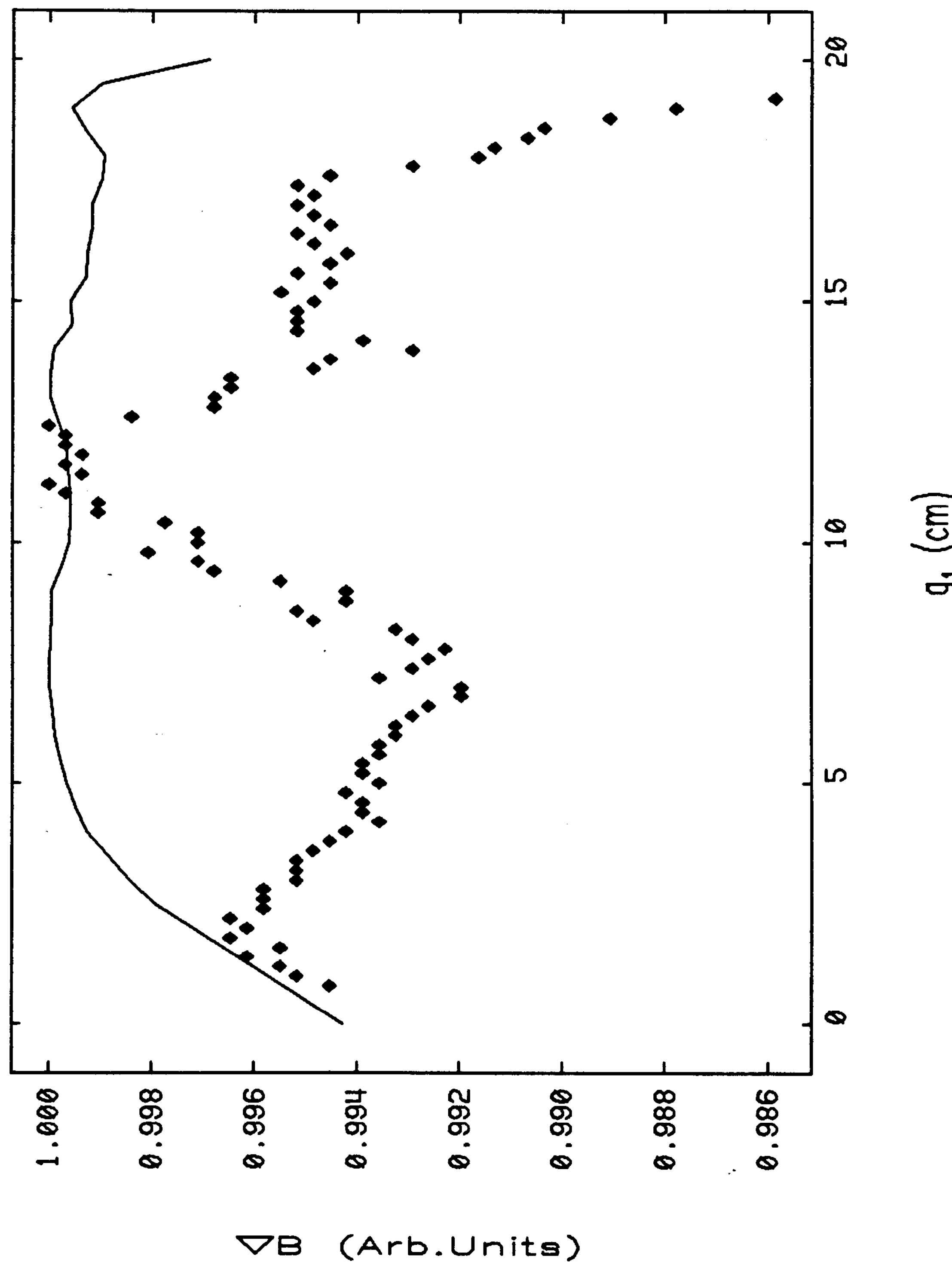

Figure 3.2: Computed and Measured Gradient of the SSRL Alpha-Magnet

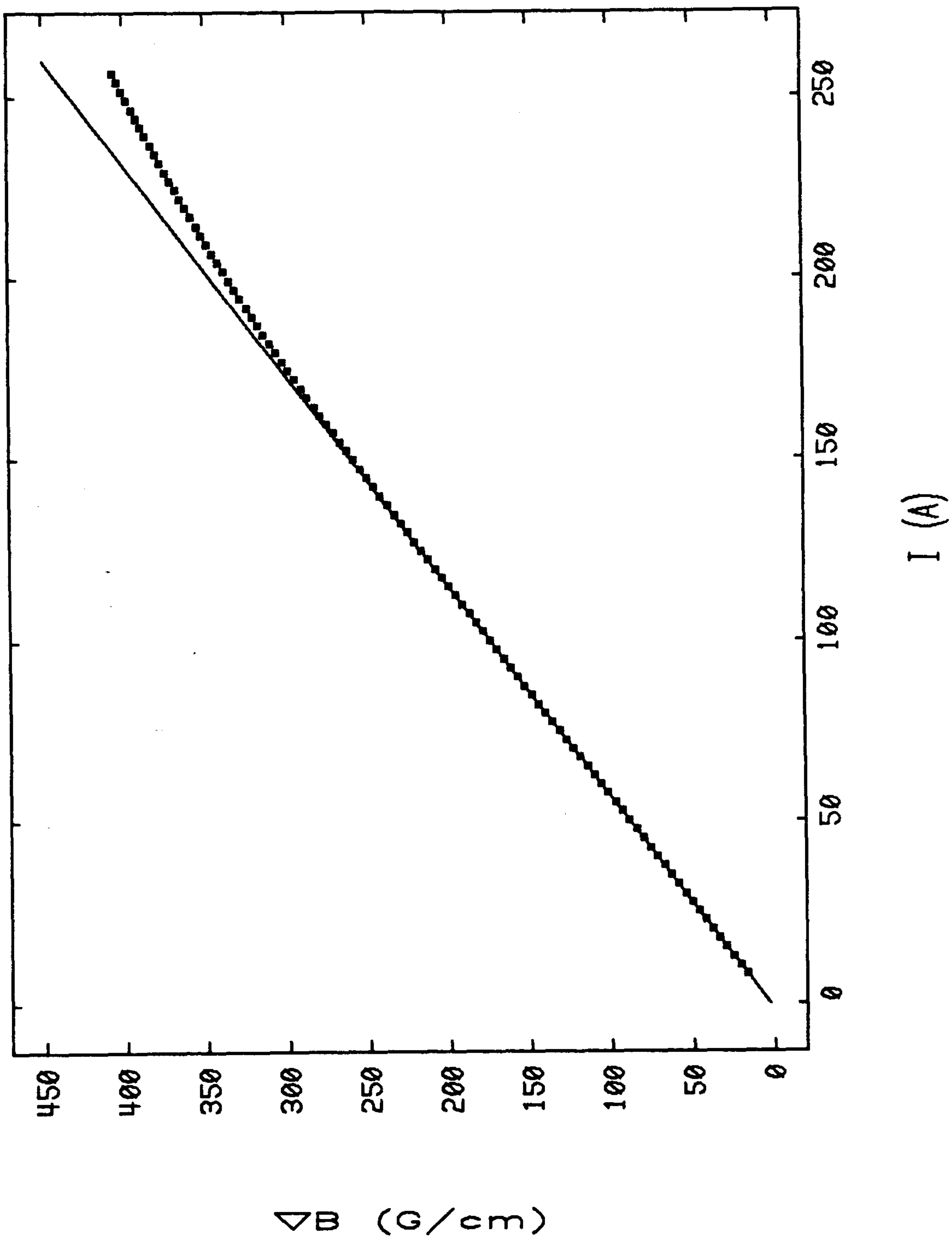

Figure 3.3: Measured Excitation Curve of the SSRL Alpha-Magnet

to ensure that spurious non-linearities did not appear in the data. The discrepancies are believed to be due in part to construction errors in the magnet, which resulted in deviations of the pole profile from the design. Some of the discrepancies are also due to round-off errors and convergence problems in POISSON, which cause the gradient near $q_1 = 0$ to become non-uniform. In any case, the non-uniformities of the gradient for the magnet without a beam port are dwarfed by those introduced when the beam port is cut into the front plate. I will return to this topic later in this chapter. Figure 3.3 shows the measured excitation curve, along with a line showing extrapolating the low-current region of the curve to high currents, which illustrates the effect of saturation. Selected magnet parameters are listed in Table 3.1.

Table 3.1: **SSRL Alpha-Magnet Design Parameters.**

number of turns	80
maximum current	260 A
maximum gradient	405 G/cm
inscribed pole radius	10 cm
good-field region (extent in q_1)	20 cm
gradient uniformity without beam port	.5%
depth (extent in q_2)	40 cm
resistance per coil @ 45°C	40 mΩ

3.1.2 Panofsky Quadrupole Design

Another magnet design that might be employed instead of the asymmetric quadrupole used here is a half Panofsky quadrupole [67] depicted in Figure 3.4. Unlike standard quadrupole designs where the quadrupole field is obtained through the approximately hyperbolic shape of the poles, the Panofsky quadrupole relies on uniform sheets of current to produce a quadrupole field. From 3.4 it can be seen that $J \neq 0$ at the pole surfaces, from which it follows that the fields in the magnet gap are *not* determined solely by the shape of the poles, in contrast to the situation for a standard quadrupole design. The most straight-forward way to calculate the fields in a Panofsky

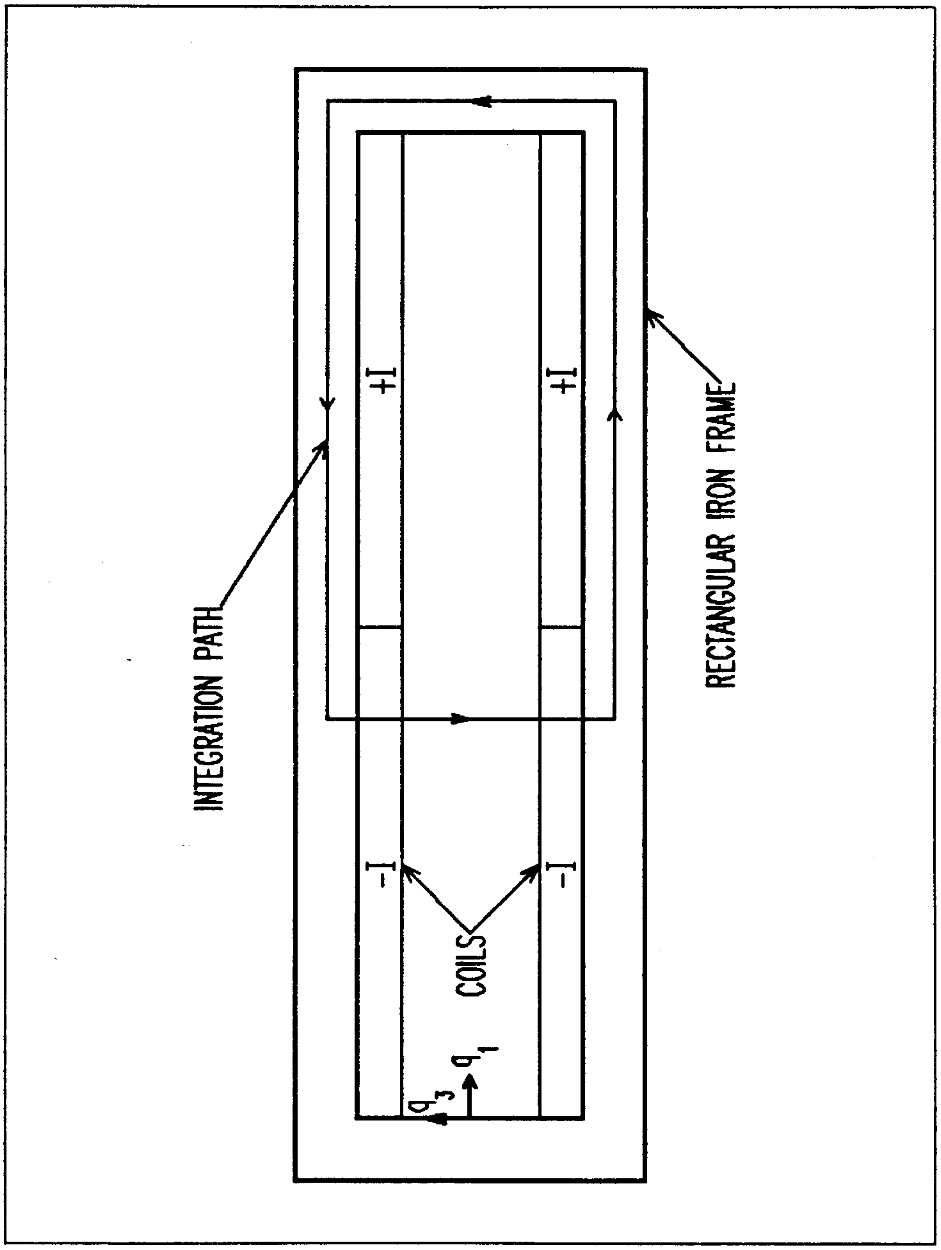

Figure 3.4: Panofsky quadrupole

quadrupole is to use the integral form of Ampere's law:

$$\int \mathbf{H} \cdot \mathbf{dl} = \frac{4\pi}{c} I. \tag{3.4}$$

In more practical units, this can be written as[6]:

$$\int \mathbf{H} \cdot \mathbf{dl} = 0.4\pi I, \tag{3.5}$$

where $\mathbf{H}$ is in Gauss, l is in cm, and I is in Ampere-turns. Taking the integration loop as shown in 3.4 and assuming infinite permeability and that H_y is a function of x only (which must be approximately true for a magnet that is wide compared to its gap-height), one obtains

$$H_3 = 0.8\pi \frac{Jtq_1}{h}, \tag{3.6}$$

where h is the full gap of the magnet, J is the current density in the current sheets, and t is the thickness of the current sheets. The linear dependence of H_3 on q_1 demonstrates that this is indeed a quadrupole. In order to obtain H_1, one employs $\nabla \times \mathbf{H} = 0$, from which it follows that

$$\mathbf{H} = \frac{8\pi}{ch} Jt(q_1\hat{q}_3 + q_3\hat{q}_1). \tag{3.7}$$

By comparison with equation (3.2), it is seen that the magnet in Figure 3.4 is, in fact, a quadrupole, with gradient

$$g = \frac{0.4\pi}{h} Jt, \tag{3.8}$$

where J is in A/cm^2, g is in G/cm and t and h are in cm.

3.1.3 Comparison of the Two Designs

A major difference between the Panofsky and asymmetric quadrupole designs for the alpha magnet is the amount of power consumed to produce a given gradient in a specified region. It is this difference that lead to the adoption of the asymmetric design for the SSRL project.

To investigate this, I will assume that what is desired is an alpha magnet with depth D (as perceived in Figures 3.1 and 3.4), useful gap h_u, and good field region G, using coils made from a metal with resistivity ρ and metal packing-fraction f. Then for the Panofsky quadrupole design, the power consumed is

$$P_{PQ} = 10fJ^2Ggh_u\rho\frac{D+G}{2fJ\pi - 5g}, \tag{3.9}$$

where J is the current density in the conductors, and where I have made the optimistic assumption that the good-field region is the same as the half-width of the coil window. The thickness of the current sheets is

$$t = \frac{5}{2}\frac{gh_u}{2fJ\pi - 5g}, \tag{3.10}$$

where

$$J > \frac{5}{2}\frac{g}{f\pi} \tag{3.11}$$

must hold in order to obtain a meaningful solution. Taking J as a free parameter of the design, the minimum power consumption is obtained when J takes the value

$$J_{PQ,opt} = 5\frac{g}{f\pi}, \tag{3.12}$$

for which the power is

$$P_{PQ,min} = \frac{50g^2Gh_u\rho(D+G)}{f\pi^2}. \tag{3.13}$$

For an asymmetric quadrupole design, the power consumed is

$$P_{AQ} = \frac{5}{\pi}K_1Ggh_u\rho J(D + K_2G), \tag{3.14}$$

where K_1 and K_2 are constants that give, respectively, the ratios of the maximum x extent of the pole and the pole-root-width to the good-field region. For the SSRL alpha-magnet, we have $K_1 \approx 1.3$ and $K_2 \approx 1$. Note that the power consumption of the asymmetric quadrupole can be decreased indefinitely by decreasing J (which is not the same as the current density in the Panofsky quadrupole), at the expense of larger coils; obviously, this is limited by practical considerations such as the cost of materials, water pressure drop, etc.

If one takes the ratio of P_{AQ} to $P_{PQ,min}$, one obtains

$$\frac{P_{AQ}}{P_{PQ,min}} = \frac{\pi K_1 f(D + K_2G)}{10(D+G)}\frac{J}{g} \approx \frac{J}{3g}, \tag{3.15}$$

where I ignore factors of order unity in making the approximation. The maximum gradient desired in the SSRL application was 350 G/cm^2. Hence, the Panofsky quadrupole would have used more power unless the current density for the asymmetric quadrupole were above about 1000 A/cm^2. In fact, the coils in the magnet could be made large enough to achieve $J \leq 175\text{A/cm}^2$, from which one can conclude that a comparable Panofsky quadrupole would consume about six times as much power as the design used.

3.2 Particle Motion in the Alpha-Magnet

3.2.1 Scaled Equation of Motion

Particle motion in the alpha-magnet is best described with the aid of a diagram such as Figure 3.5, which shows the central particle trajectory and the coordinate system. In terms of these coordinates, the magnetic field for $q_1 > 0$ is

$$\mathbf{B} = g(q_3\mathbf{q}_1 + q_1\mathbf{q}_3), \tag{3.16}$$

where the constant g is the alpha-magnet gradient. The equation of motion is obtained from the Lorentz force

$$\mathbf{F} = -e\mathbf{E} + \frac{q}{c}\mathbf{v} \times \mathbf{B}, \tag{3.17}$$

with $\mathbf{E} = 0$, and is

$$\frac{d\gamma\mathbf{v}}{dt} = -\frac{e}{m_e c}\mathbf{v} \times \mathbf{B}. \tag{3.18}$$

Since the magnetic field does no work, γ is constant and can be taken outside the derivative. Since the magnitude of the velocity is also constant, one can rewrite the derivatives as derivatives with respect to path-length, $s = \beta ct$, instead of time. Combining these, one obtains

$$\frac{d^2\mathbf{q}}{ds^2} = -\frac{e}{m_e c^2 \beta\gamma}\frac{d\mathbf{q}}{ds}\times\mathbf{B}. \tag{3.19}$$

I now define a constant α by

$$\alpha^2 = \frac{eg}{m_e c^2 \beta\gamma}, \tag{3.20}$$

or, in more practical units

$$\alpha^2 = 5.86674 \times 10^{-4}\text{cm}^{-2}\frac{g(\text{G/cm})}{\beta\gamma}. \tag{3.21}$$

The equation of motion becomes

$$\begin{aligned}
\frac{d^2\mathbf{q}}{ds^2} &= -\alpha^2\frac{d\mathbf{q}}{ds}\times\frac{\mathbf{B}(\mathbf{q})}{g} && (3.22)\\
&= -\alpha^2\frac{d\mathbf{q}}{ds}\times(q_3, 0, q_1) && (3.23)\\
&= -\alpha^2\left(\frac{dq_2}{ds}q_1, \frac{dq_3}{ds}q_3 - \frac{dq_1}{ds}q_1, -\frac{dq_2}{ds}q_3\right) && (3.24)
\end{aligned}$$

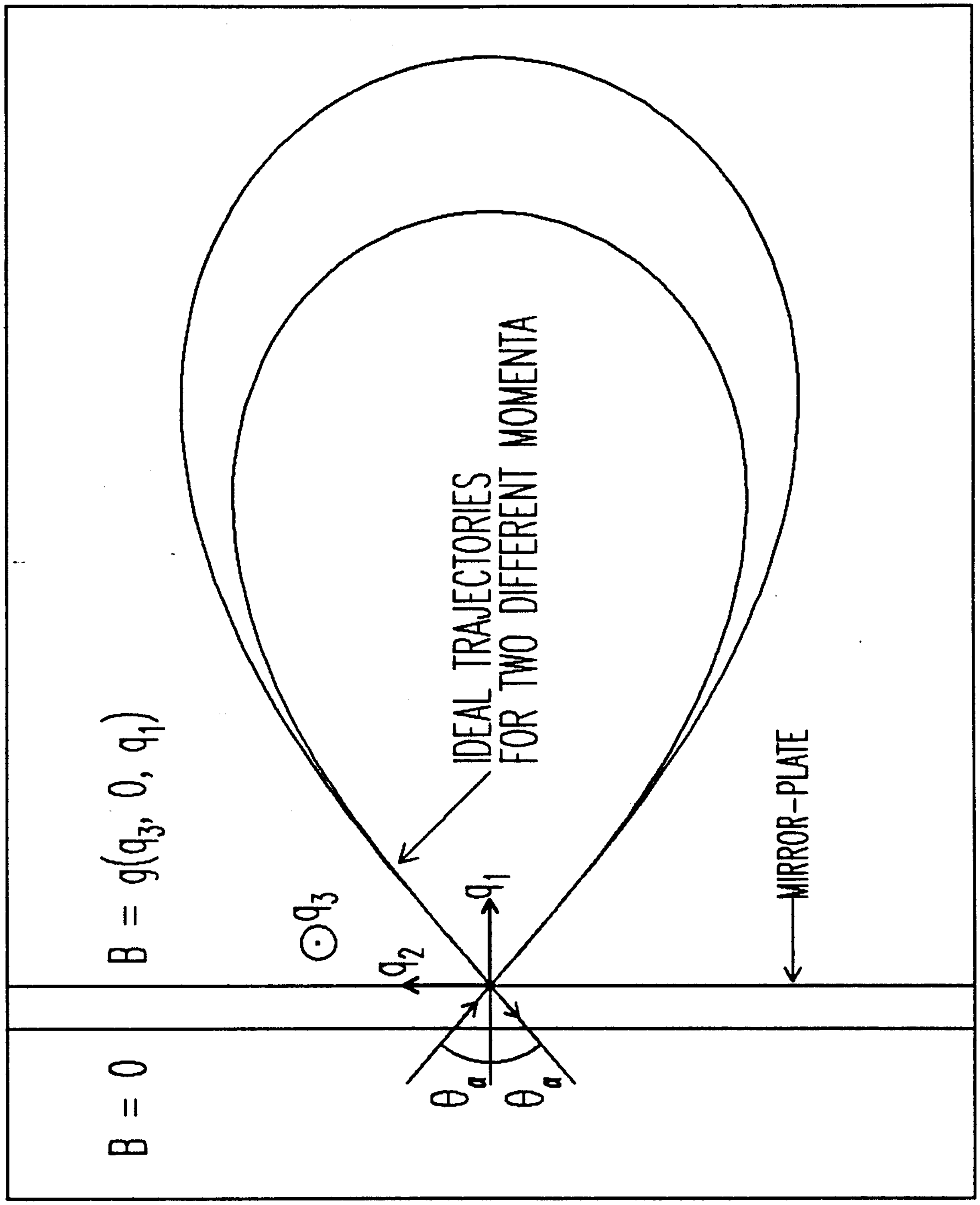

Figure 3.5: Alpha-magnet coordinate system

I chose by convention to make $g > 0$, i.e., I define the $\mathbf{e}_3$ axis to obtain $B_3 > 0$ inside the magnet. This also ensures that $\alpha^2 > 0$, so that α is real and positive. To obtain an α-like trajectory like that exhibited in Figure 3.5, it is then necessary to have initial velocities such that

$$\frac{dq_1}{ds} > 0 \quad \text{and} \quad \frac{dq_2}{ds} < 0. \tag{3.25}$$

I wish to rewrite this equation of motion once more, in such a way as to scale out all explicit dependence on g and $\beta\gamma$. To do this, I define scaled coordinates $\mathbf{Q} = \mathbf{q}\alpha$ and scaled path-length $S = s\alpha$. Using this, I obtain

$$\begin{aligned} \frac{d^2\mathbf{Q}}{dS^2} &= -\frac{d\mathbf{Q}}{dS} \times \mathbf{B}(\frac{\mathbf{Q}}{\alpha})\frac{\alpha}{g} && (3.26) \\ &= -\frac{d\mathbf{Q}}{dS} \times (Q_3, 0, Q_1) && (3.27) \\ &= -\left(\frac{dQ_2}{dS}Q_1, \frac{dQ_3}{dS}Q_3 - \frac{dQ_1}{dS}Q_1, -\frac{dQ_2}{dS}Q_3\right) && (3.28) \end{aligned}$$

Note that

$$\left(\frac{dQ_1}{dS}\right)^2 + \left(\frac{dQ_2}{dS}\right)^2 + \left(\frac{dQ_3}{dS}\right)^2 = 1, \tag{3.29}$$

a result which will be useful latter, and which in fact does not depend on the scaling (it is true of $\frac{dq}{ds}$ as well).

3.2.2 Ideal Trajectory

From this result, one can deduce that an alpha-magnet can act like an achromatic magnetic mirror, that is, that a zero-emittance beam injected at a specific angle, θ_α, to the normal into a perfect alpha-magnet will emerge at the point of injection, at the same angle to the normal and undispersed in momentum.

To see this, first note that the scaled form of the equation of motion does not display any dependence on momentum. Hence, the trajectories of particles with various momenta injected into the magnet at the same angle are simply magnifications or demagnifications of one another. Since the scaled equation likewise does not exhibit any dependence on gradient, the same can be said of particles injected into alpha magnets with differing gradients. Because the scaling involves all coordinates, it leaves angles unchanged. Hence, if a closed, α-like trajectory does exist, it has the same shape and the same incident and final angles for all values of α (i.e., for particles of all momenta in alpha magnets of all gradients).

Note that the scaling alone is not sufficient to ensure that the magnet can be operated as an achromat. It is also necessary that a trajectory exists which exits at the injection point, since otherwise the scaling would change the exit location relative to the injection point. This would, of course, imply non-zero dispersion upon exiting the magnet.

Next, set $Q_3 = 0$ and note that for trajectories started at $Q_2 = 0$ with $\frac{dQ_1}{dS} = 0$ (implying $\frac{dQ_2}{dS} = 1$) there is some initial value, $\hat{Q}_1$, of Q_1 that results in a trajectory that crosses $Q_1 = Q_2 = 0$. To see that this must be so, imagine starting trajectories from $Q_2 = 0$ at various initial values of Q_1. A trajectory started at infinitesimally small $Q_1 > 0$ will cross $Q_1 = 0$ at infinity, since it "sees" very little magnetic field, and hence is bent toward $Q_1 = 0$ only very gradually. As the starting Q_1 is increased, the trajectory crosses $Q_1 = 0$ at less and less positive values of Q_2, until eventually, for initial $Q_1 = \hat{Q}_1$, the trajectory crosses $Q_1 = 0$ at $Q_2 = 0$.

I will denote this trajectory by $\overline{\mathbf{Q}}(S) = (\overline{Q}_1(S), \overline{Q}_2(S), 0)$, and let $S = 0$ at the start of the trajectory, which is formally defined only for $S > 0$. By construction, $\overline{\mathbf{Q}}(S)$ is a solution to the equations of motion. Consider a new trajectory $\tilde{\mathbf{Q}}(S)$ defined for $S < 0$ as $(\overline{Q}_1(-S), -\overline{Q}_2(-S), 0)$. Upon inserting this trajectory into the equation of motion (with $Q_3 = \frac{dQ_3}{dS} = 0$), one obtains for the left-hand side of equation (3.26), for component 1:

$$\frac{d^2\tilde{Q}_1(S)}{dS^2} = \frac{d^2\overline{Q}_1(-S)}{dS^2} \tag{3.30}$$

$$= \frac{d^2\overline{Q}_1(-S)}{d(-S)^2}\left(\frac{d(-S)}{dS}\right)^2 \tag{3.31}$$

$$= \left(\frac{d^2\overline{Q}_1(S)}{dS^2}\right)_{(S\to -S)} \tag{3.32}$$

$$\tag{3.33}$$

Similarly, for component 2, one obtains

$$\frac{d^2\tilde{Q}_2(S)}{dS^2} = -\left(\frac{d^2\overline{Q}_1(S)}{dS^2}\right)_{(S\to -S)}. \tag{3.34}$$

For the right-hand-side of equation (3.28), one obtains for components 1 and 2, respectively:

$$-\left(\frac{d}{dS}(-\overline{Q}_2(-S))\right)\overline{Q}_1(-S) = \left(-\frac{d\overline{Q}_2(S)}{dS}\overline{Q}_1(S)\right)_{(S\to -S)} \tag{3.35}$$

$$\left(\frac{d}{dS}\overline{Q}_1(-S)\right)\overline{Q}_1(-S) = -\left(\frac{d\overline{Q}_1(S)}{dS}\overline{Q}_1(S)\right)_{(S\to -S)} \tag{3.36}$$

(3.37)

Combining these last results, one sees that except for the change of variable S to -S, the resultant equations are just those that would be obtained by inserting $\overline{\mathbf{Q}}$ into the equation of motion. Hence, $\tilde{\mathbf{Q}}$ is a solution to the equation of motion, since $\overline{\mathbf{Q}}$ is. Further, the trajectory $\mathbf{Q}_\alpha(S)$, defined by joining $\overline{\mathbf{Q}}$ to $\tilde{\mathbf{Q}}$ at S=0, is also a solution. The subscript α is used from here on to represent properties of the solution $\mathbf{Q}_\alpha(S)$, which is the "α-shaped" trajectory. There should be no confusion with the scaling parameter α, defined by equation (3.20), since the later is not used as a subscript.

A trajectory has thus been demonstrated to exist which starts at $Q_1 = Q_2 = 0$ with such values of $\frac{dQ_1}{dS}$ and $\frac{dQ_2}{dS}$ so as reach $Q_1 = \hat{Q}_1$ and $Q_2 = 0$ with $\frac{dQ_1}{dS} = 0$, and which continues in a mirror symmetric fashion, crossing $Q_1 = Q_2 = 0$ with the negative of the slope with which it started. The absolute value of this slope is denoted by $\tan(\theta_\alpha)$.

Corresponding to $Q_\alpha(S)$ is an alpha-shaped trajectory for any gradient and particle momentum. These trajectories enter and exit at the angle θ_α, since slopes are not changed by the coordinate scaling.

3.2.3 Numerical Solution of the Equations

It is possible to solve for $\mathbf{Q}_\alpha(S)$ in terms of elliptic integrals[32]. However, this is unproductive, since in the end one obtains a result that can only be used by consulting numerical tables or doing numerical integration. It is better to go directly to numerical integration, especially since the scaled form of the equation allows one to apply the results of a single numerical integration to an infinite number of combinations of $\beta\gamma$ and g.

In order to find the angle θ_α and the maximum value of Q_1 for the trajectory $\mathbf{Q}_\alpha(S)$, I used numerical integration starting at $Q_1 = Q_2 = 0$ and searched for the value of θ_α that resulted in $\frac{dQ_1(S)}{dS} = 0$ when the trajectory crosses the $Q_2 = 0$ axis again. To gauge the accuracy of the numerical integration, note that at that

$$\begin{aligned} \left|\frac{dQ}{dS} - 1\right| &< 5 \times 10^{-16} &\quad (3.38)\\ \left(\frac{dQ_1}{dQ_2}\right)_{\text{midplane}} &< 5 \times 10^{-15}, &\quad (3.39)\end{aligned}$$

where the average are taken over the entire integration, which shows that the integration is accurate to 14 decimal places. The Bulirsch-Stoer integration method was employed [61]. Briefly, Bulirsch-Stoer uses the modified midpoint method with polynomial extrapolation of the solution to zero step-size, along with adaptive step-size control.

In this fashion, I obtained

$$\begin{aligned} \theta_\alpha &= 0.71052198004575 &\quad (3.40)\\ &= 40.709910707900^\circ &\quad (3.41)\\ S_\alpha &= 4.64209946506084 &\quad (3.42)\\ \hat{Q}_1 &= 1.81781711509708 &\quad (3.43)\end{aligned}$$

θ_α is the injection angle for achromatic mirror operation, i.e., the injection angle that results in the trajectory $\mathbf{Q}_\alpha(S)$. S_α is the path length of $\mathbf{Q}_\alpha(S)$ through the entire magnet. $\hat{Q}_1$ is the maximum value of Q_1 reached by $\mathbf{Q}_\alpha(S)$. These quantities are illustrated in Figure 3.6.

3.2.4 Dispersion and Achromatic Path-Length

While these results are not sufficient to fully characterize the optics of the alpha-magnet (see the next section for this), they do allow one to deduce some of the magnet's most important optical properties, namely the dispersion at the vertical midplane and the dependence of path-length on momentum. For this, I revert to unscaled coordinates, and write

$$\begin{aligned} s_\alpha(\alpha) &= \frac{S_\alpha}{\alpha} . &\quad (3.44)\\ \hat{q}_1(\alpha) &= \frac{\hat{Q}_1}{\alpha}. &\quad (3.45)\end{aligned}$$

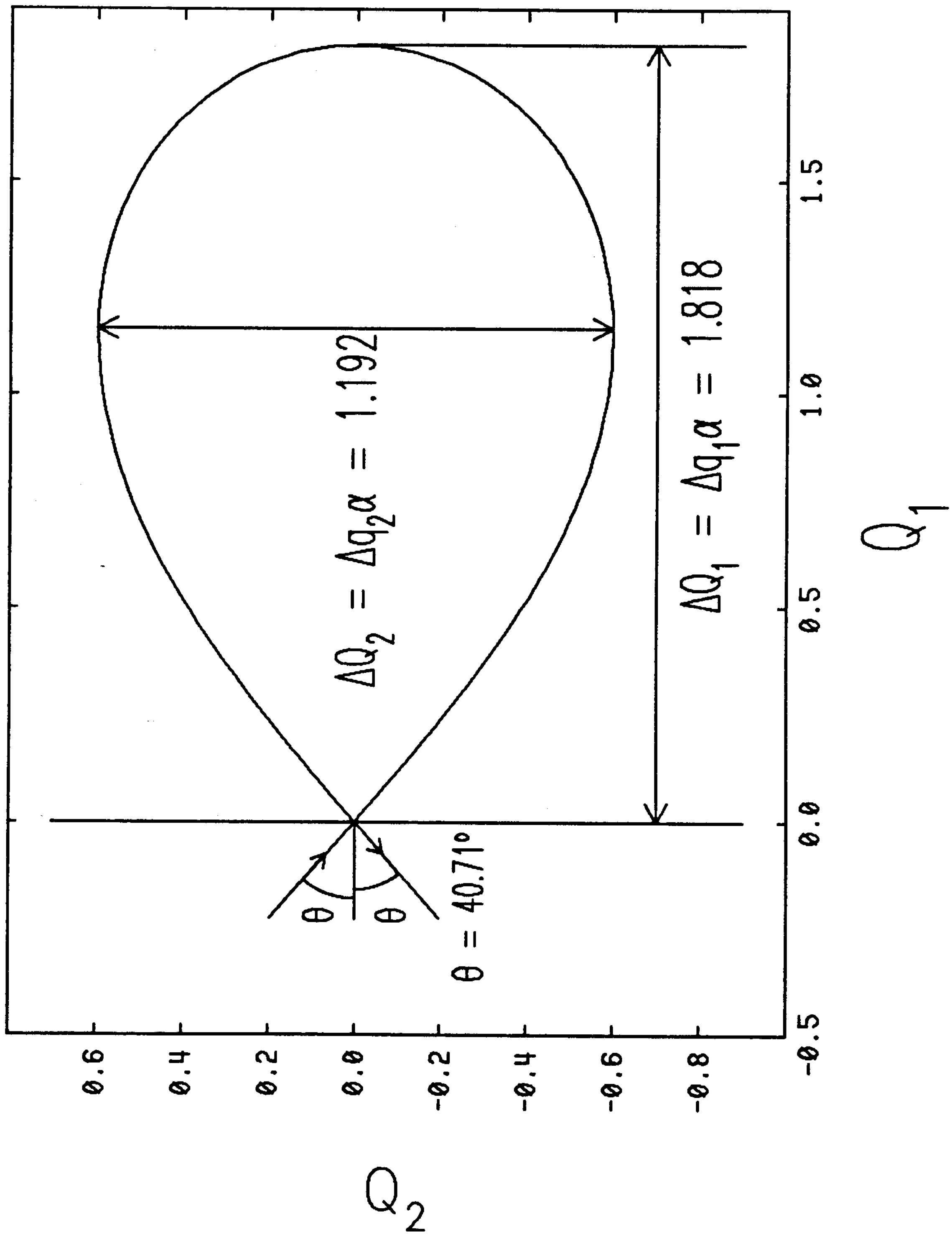

Figure 3.6: Ideal Trajectory in the Alpha-Magnet

In more practical units, and using the numerical values of S_α and $\hat{Q}_1$ given above

$$s_\alpha(\mathrm{cm}) = 191.655\sqrt{\frac{\beta\gamma}{g(\mathrm{G/cm})}} \tag{3.46}$$

$$\hat{q}_1(\mathrm{cm}) = 75.0513\sqrt{\frac{\beta\gamma}{g(\mathrm{G/cm})}} \tag{3.47}$$

Assuming that the gradient g is fixed, and letting α_o be the value of α for the central particle, of momentum $p_o = (\beta\gamma)_o$, the previous equations imply that

$$s(\alpha) = s(\alpha_o)\frac{\alpha_o}{\alpha} \tag{3.48}$$

$$\hat{q}_1(\alpha) = \hat{q}_1(\alpha_o)\frac{\alpha_o}{\alpha}. \tag{3.49}$$

Expanding in $\delta = (p - p_o)/p$, one obtains

$$\frac{\alpha_o}{\alpha} = \sqrt{\frac{p}{p_o}} \tag{3.50}$$

$$\approx 1 + \frac{1}{2}\delta - \frac{1}{8}\delta^2 + \frac{1}{16}\delta^3. \tag{3.51}$$

Using this expansion the dispersive terms of the transport matrix (see the next section) from the entrance of the magnet to the "vertical midplane" (where the ideal trajectory crosses $q_2 = 0$ with $q_1 = \hat{q}_1$) are seen to be

$$r_{16} \equiv -\left(\frac{\partial \hat{q}_1}{\partial \delta}\right)_{\delta=0} \tag{3.52}$$

$$= -\frac{1}{2}\hat{q}_1(\alpha_o) \tag{3.53}$$

$$t_{166} \equiv -\frac{1}{2!}\left(\frac{\partial^2 \hat{q}_1}{\partial \delta^2}\right)_{\delta=0} \tag{3.54}$$

$$= \frac{1}{8}\hat{q}_1(\alpha_o) \tag{3.55}$$

$$u_{1666} \equiv -\frac{1}{3!}\left(\frac{\partial^3 \hat{q}_1}{\partial \delta^3}\right)_{\delta=0} \tag{3.56}$$

$$= -\frac{1}{16}\hat{q}_1(\alpha_o) \tag{3.57}$$

Similarly, the path-length terms for transport through the entire magnet are

$$r_{56} = \frac{1}{2}s(\alpha_o) \tag{3.58}$$

$$t_{566} = -\frac{1}{8}s(\alpha_\circ) \tag{3.59}$$

$$u_{5666} = \frac{1}{16}s(\alpha_\circ) \tag{3.60}$$

These will prove useful in checking the results of detailed transport matrix calculations. They are also of interest because the dispersion at the vertical midplane and the momentum-dependence of the path-length are two of the alpha-magnet's most useful features. The dispersion at the vertical midplane allows for momentum selection via a slit or scraper placed at the vertical midplane. The momentum-dependence of the path-length is, of course, necessary for bunch compression, as indicated in the introduction to this chapter.

3.3 Alpha-Magnet Transport Matrix Scaling

In this section I derive results that provide the basis for a calculation of alpha-magnet transport matrices to third order. Transport matrices express particle motion between two points in a beamline as a series expansion about the trajectory of a hypothetical particle that travels along what is considered to be the ideal trajectory for the beamline. Typically this ideal trajectory passes through the center of focusing elements, down the center of the beam-pipe, and so forth. In the case of the alpha-magnet, the ideal trajectory enters and exits at the angle θ_α, with $q_3 = \frac{dq_3}{ds} = 0$.

3.3.1 Curvilinear Coordinates and Matrix Notation

The coordinates used for the transport matrix expansion[10] specify offsets in six-dimensional phase-space of a particle from the ideal trajectory. The coordinate system is curvilinear; i.e., it follows the ideal trajectory. This subject is treated completely in publications on particle beam dynamics, listed in the references. Here, I will simply state that the position of any particle relative to the fiducial particle can be specified in terms of two transverse coordinates, x and y, their derivatives with respect to path length (s_c) for the central trajectory,

$$x' = \frac{dx}{ds_c} \qquad\qquad y' = \frac{dy}{ds_c}, \tag{3.61}$$

the longitudinal distance s traveled, and the momentum deviation δ, introduced in the last section. As is usually done, I form a six-dimensional vector from these coordinates:

$$\mathbf{x} = \begin{pmatrix} x \\ x' \\ y \\ y' \\ s \\ \delta \end{pmatrix}. \tag{3.62}$$

This vector gives information about a particle as it crosses a reference plane somewhere in the beamline. The reference plane is constructed so that the fiducial particle passes through it perpendicularly. I emphasize that the path-length s is *not* the distance of a particle behind the fiducial particle; I depart from convention here in keeping track of the total path-length, for reasons that will be apparent later. This carries no penalty for a beamline composed of static elements, since the expansions in $s - s_o$ are then of no importance.

Transformation of this vector by beamline elements is expressed as a series expansion:

$$x_i \longrightarrow c_i + \sum_j r_{ij} x_j + \sum_{j \geq k} t_{ijk} x_j x_k + \sum_{j \geq k \geq l} u_{ijkl} x_j x_k x_l, \tag{3.63}$$

where c, r, t, and u are the transport matrices for some element, and summation indices run from 1 to 6 unless otherwise indicated. (The reason for the lower-case letters will be seen presently.) The restricted sums are used to obtain expressions that contain only one instance of any term $x_j x_k$ or $x_j x_k x_l$. This is consistent with K.Brown[10], but differs from the definition used by TRANSPORT[68] and some other computer programs, where the matrices are defined in terms of symmetric sums over all indices. The unsymmetric form also has advantages in a computer program, namely reduction of storage used and reduction of the number of arithmetic operations needed to transform particle coordinates. I employ the unsymmetric form exclusively in this work.

The element c is unconventional, and is used to keep track of centroid offsets. It finds application in three ways. First, when used in a tracking program, associating a centroid offset matrix with an element allows one to implement beam misalignments and steering in a straight-forward fashion. In addition, time-of-flight calculations are facilitated by the path-length centroid element, which is useful in a simulation that has time-dependent elements [49]. Second, it is a necessary corrolary of my use of total path-length instead of differential path-length in the vector **x**. Third, in the particular case of the alpha-magnet, the centroid matrix can be used to calculate higher-order dispersive path-length terms, as will be seen below. For the alpha-magnet and all other elements that do not produce orbit distortions, only the c_5 element is non-zero.

3.3.2 Relationships Between Curvilinear and Fixed Coordinates

At this point, the reader might expect the equation of motion to be rewritten in terms of the curvilinear coordinates. This is unnecessary for my purposes. All that I will need in order calculate the matrices (c, r, t, u) is to express the relationship between the curvilinear coordinates $\mathbf{x}$ and the coordinates of the equation of motion, $\mathbf{q}$, at the entrance, vertical midplane, and exit of the alpha-magnet, since it is between these reference planes that I wish to know the transport matrices.

At the entrance of the alpha-magnet (i.e., when the particle crosses the reference plane shown in Figure 3.7), the correspondence between $\mathbf{x}$ and $\mathbf{q}$ is given by

$$\begin{pmatrix} \mathrm{x} \\ \mathrm{x}' \\ \mathrm{y} \\ \mathrm{y}' \\ \tau \\ \delta \end{pmatrix} = \begin{pmatrix} \mathrm{sign}(\mathrm{q}_1)\sqrt{\mathrm{q}_1^2 + \mathrm{q}_2^2} \\ \tan(\mathrm{atan}(-\mathrm{q}_1'/\mathrm{q}_2') - \bar{\theta}_\alpha) \\ \mathrm{q}_3 \\ \mathrm{q}_3' \\ \mathrm{s} \\ (\mathrm{p} - \mathrm{p}_\circ)/\mathrm{p}_\circ \end{pmatrix}, \tag{3.64}$$

where I have used

$$\bar{\theta}_\alpha \equiv \frac{\pi}{2} - \theta_\alpha. \tag{3.65}$$

The slopes q_1' and q_3' are given by

$$\mathrm{q}_1' = \sqrt{1 - (\mathrm{q}_3')^2}\sin(\bar{\theta}_\alpha + \mathrm{atan}(\mathrm{x}')) \tag{3.66}$$

and

$$\mathrm{q}_2' = \sqrt{1 - (\mathrm{q}_3')^2}\cos(\bar{\theta}_\alpha + \mathrm{atan}(\mathrm{x}')), \tag{3.67}$$

while the coordinates q_1 and q_2 are given by

$$\mathrm{q}_1 = \mathrm{x}\sin\theta_\alpha \tag{3.68}$$

and

$$\mathrm{q}_2 = \mathrm{x}\cos\theta_\alpha. \tag{3.69}$$

The reader may have noticed that the reference plane in Figure 3.7 is partially inside and partially outside the alpha-magnet. Hence, it would seem that in reaching

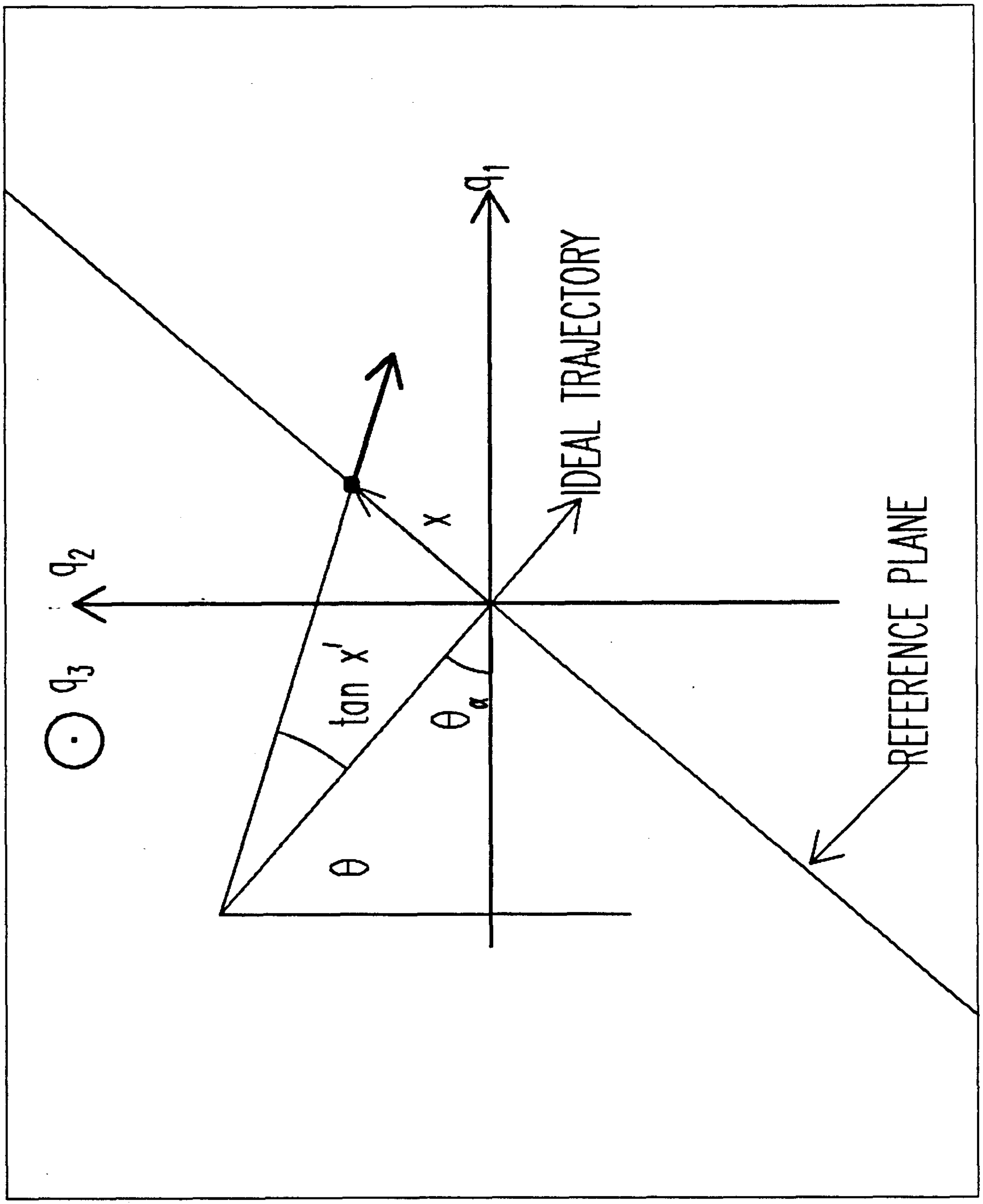

Figure 3.7: Reference plane and coordinates at the entrance

the reference plane, from which transport through the alpha-magnet nominally starts in the transport matrix formalism, some particles have already traversed part of the alpha-magnet's magnetic field. Others (those for which $x < 0$ in figure 3.7), will not yet be inside the alpha-magnet. It would seem that the length of a drift space, for example, prior to the alpha magnet would need to be modified according to the coordinates of the particle, and this is effectively what is done. The prior element in the transport line (presumably a drift space) is considered to deliver all of the particles to the reference plane, with no account taken of the alpha-magnet fields. The computation of the alpha-magnet matrices (see the subsequent sections of this chapter) takes this into account, so that particles that are delivered inside (outside) the alpha-magnet are drifted backward (forward) to the field boundary of the alpha-magnet before numerical integration. As will be seen presently, similar considerations apply at the exit of the alpha-magnet, and an identical procedure is followed for this case.

One could also consider constructing an edge-matrix for the alpha-magnet, similar to what is done for bending magnets, but since the entrance and exit angles for the alpha-magnet do not vary between applications (as they do for bending magnets), this is neither necessary nor useful.

At the vertical midplane of the magnet (i.e., when the particle crosses $q_2 = 0$ inside the magnet, see Figure 3.8), a different relationship holds:

$$\begin{pmatrix} x \\ x' \\ y \\ y' \\ \tau \\ \delta \end{pmatrix} = \begin{pmatrix} \hat{q}_1 - q_1 \\ -q_1'/q_2' \\ q_3 \\ q_3' \\ s \\ (p - p_o)/p \end{pmatrix}. \tag{3.70}$$

The slopes q_1' and q_3' are given by

$$q_1' = -\sqrt{1 - (q_3')^2}\,\sin\left(\mathrm{atan}(x')\right) \tag{3.71}$$

and

$$q_2' = \sqrt{1 - (q_3')^2}\,\cos\left(\mathrm{atan}(x')\right), \tag{3.72}$$

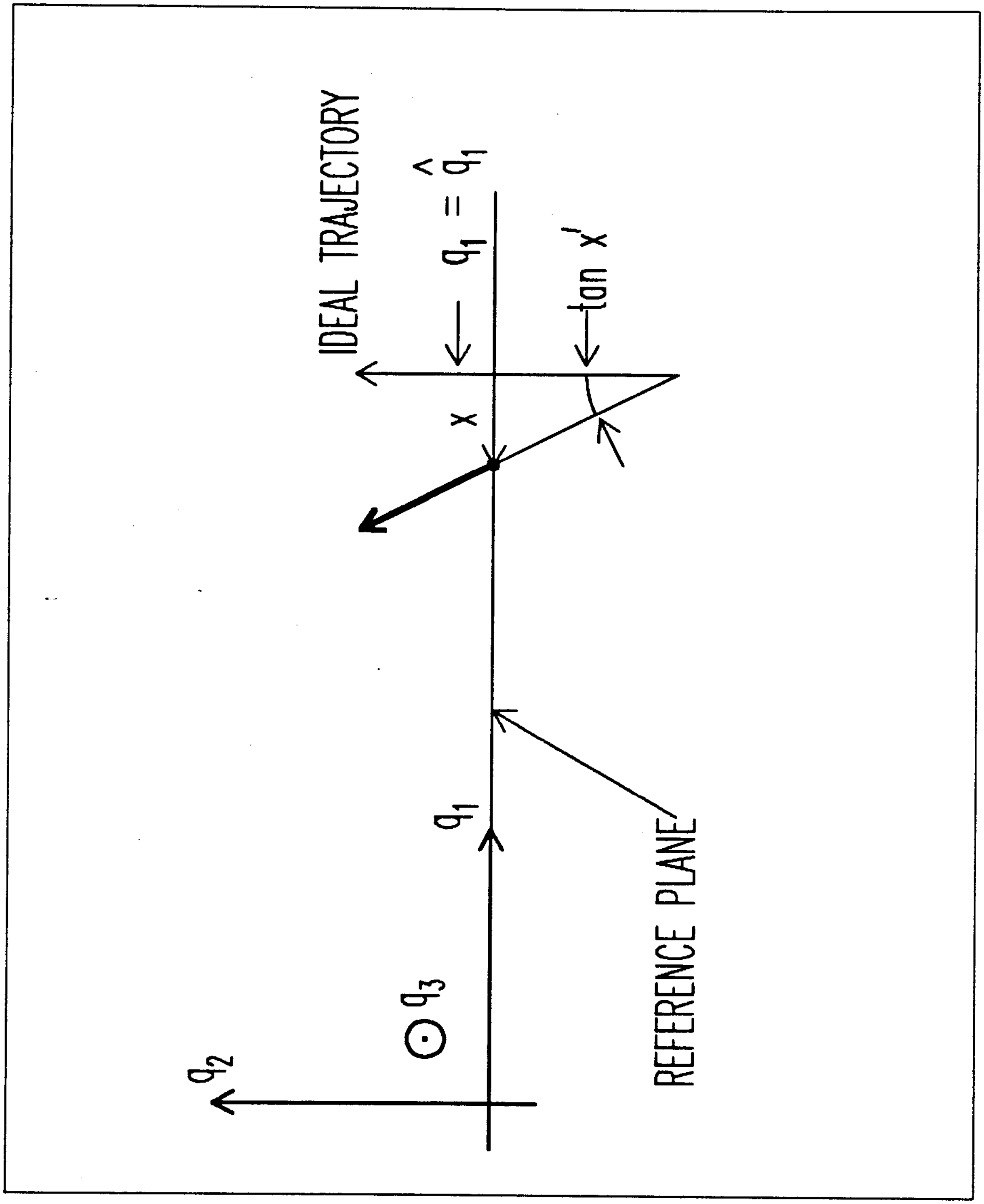

Figure 3.8: Reference plane and coordinates at the vertical midplane

while the coordinates q_1 and q_2 are given by

$$q_1 = \hat{q}_1 - x \tag{3.73}$$

and

$$q_2 = 0. \tag{3.74}$$

Finally, at the exit of the magnet (i.e., when the particle crosses the reference plane shown in Figure 3.9), one obtains:

$$\begin{pmatrix} x \\ x' \\ y \\ y' \\ \tau \\ \delta \end{pmatrix} = \begin{pmatrix} \mathrm{sign}(q_1)\sqrt{q_1^2 + q_2^2} \\ \tan(\bar{\theta}_\alpha - \mathrm{atan}(q_1'/q_2')) \\ q_3 \\ q_3' \\ s \\ (p - p_\circ)/p \end{pmatrix}. \tag{3.75}$$

The slopes q_1' and q_3' are given by

$$q_1' = -\sqrt{1 - (q_3')^2}\sin(\bar{\theta}_\alpha - \mathrm{atan}(x')) \tag{3.76}$$

and

$$q_2' = -\sqrt{1 - (q_3')^2}\cos(\bar{\theta}_\alpha - \mathrm{atan}(x')), \tag{3.77}$$

while the coordinates q_1 and q_2 are given by

$$q_1 = x \sin\theta_\alpha \tag{3.78}$$

and

$$q_2 = -x\cos\theta_\alpha. \tag{3.79}$$

3.3.3 Coordinate Scaling

Let the gradient in the alpha-magnet and the momentum of the fiducial particle be specified, so that the scaling parameter α takes a definite value, α_o. Then it is possible to define a new vector $\mathbf{X}$ that has the same relationship to $\mathbf{Q}$ that $\mathbf{x}$ has to $\mathbf{q}$. $\mathbf{X}$ is obtained from $\mathbf{x}$ by the transformation

$$\mathbf{X} = \mathbf{A}(\alpha_\circ) \cdot \mathbf{x}, \tag{3.80}$$

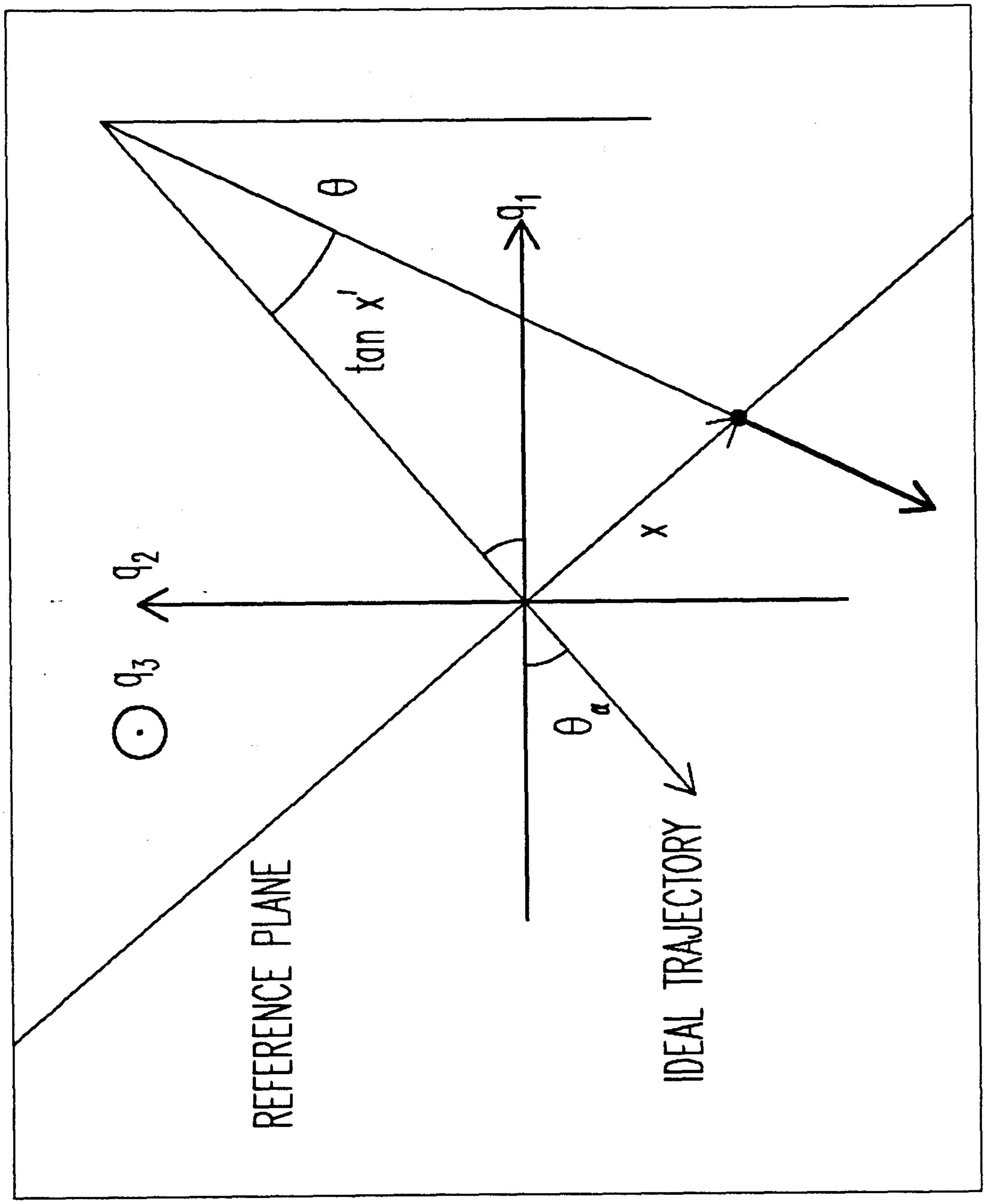

Figure 3.9: Reference plane and coordinates at the exit

where $\mathbf{A}(\alpha_o)$ is a diagonal matrix, given by

$$\mathbf{A}(\alpha_o) = \begin{pmatrix} \alpha_o & 0 & 0 & 0 & 0 & 0 \\ 0 & 1 & 0 & 0 & 0 & 0 \\ 0 & 0 & \alpha_o & 0 & 0 & 0 \\ 0 & 0 & 0 & 1 & 0 & 0 \\ 0 & 0 & 0 & 0 & \alpha_o & 0 \\ 0 & 0 & 0 & 0 & 0 & 1 \end{pmatrix}. \tag{3.81}$$

The transformation from $\mathbf{x}$ to $\mathbf{X}$ transforms the fiducial particle, which traveled a particular α-like trajectory $\mathbf{Q}_\alpha(\mathrm{s}\alpha_o)/\alpha_o$, into the particle that follows the universal trajectory $\mathbf{Q}_\alpha(\mathrm{S})$. To see this more clearly, note that the expression for $\mathbf{X}$ at the vertical midplane is

$$\begin{pmatrix} \mathrm{X} \\ \mathrm{X}' \\ \mathrm{Y} \\ \mathrm{Y}' \\ S \\ \delta \end{pmatrix} = \begin{pmatrix} \hat{\mathrm{Q}}_1 - \mathrm{Q}_1 \\ -\mathrm{atan}(\mathrm{Q}_1'/\mathrm{Q}_2') \\ \mathrm{Q}_3 \\ \mathrm{Q}_3' \\ \mathrm{S} \\ (\mathrm{p}-\mathrm{p}_o)/\mathrm{p} \end{pmatrix}, \tag{3.82}$$

where $\mathbf{Q}' \equiv \frac{\mathrm{d}\mathbf{Q}}{\mathrm{dS}}$. (Since angles are unchanged by the scaling, I am free to express the slopes in terms of either the Q_i''s or the q_i''s, even though this "transformation" is not in the matrix $\mathbf{A}$.)

3.3.4 Scaled Equation of Motion with Dispersive Terms

The reader may have noted an apparent inconsistency here: this vector, which is in scaled coordinates, refers to the momentum error, but the scaling was explicitly constructed so as to remove all reference to momentum. The apparent inconsistency stems from the fact that, as developed in the last section, the scaled equation of motion treats every particle (each characterized by some particular scaling constant α) as the fiducial particle (at least as far as momentum is concerned). What is needed to incorporate momentum errors into the scaled equation of motion is to realize that one scales the equation with α_o, the α value for the central momentum, and not with the particular α of every particle under consideration. The resultant scaled equation, with dispersive effects included exactly, is

$$\mathbf{Q}'' = -\frac{1}{1+\delta}\mathbf{Q}' \times \mathbf{B}(\frac{\mathbf{Q}}{\alpha})\frac{\alpha}{g} \quad (3.83)$$

$$= -\frac{1}{1+\delta}\frac{d\mathbf{Q}}{dS}\times(Q_3, 0, Q_1) \quad (3.84)$$

As foreshadowed at the end of the last section, it is not entirely necessary to include dispersive effects in this fashion. One can obtain all dispersive terms in the matrices by taking derivatives with respect to δ after reverting to unscaled coordinates, though this requires some care if it is to be done correctly. This will be discussed in more detail below. One reason for inserting dispersive effects at this point is to retain the six-dimensional transport matrix formalism. Another reason, as indicated at the end of the last section and as will become more apparent below, is that putting dispersive effects into the formalism provides a check on the calculation of the matrix.

3.3.5 Scaling of the Transport Matrices

One can define transformation matrices for the vector $\mathbf{X}$, with the realization that these transformation matrices apply to the scaled form of the equation of motion:

$$X_I \longrightarrow C_I + \sum_I R_{IJ}X_J + \sum_{J\geq K} T_{IJK}X_JX_K + \sum_{J\geq K\geq L} U_{IJKL}X_JX_KX_L. \quad (3.85)$$

If I now substitute into this relation the definition of $\mathbf{X}$, equation (3.80), I obtain

$$\sum_m A_{Im}x_m \longrightarrow C_I + \sum_{Jj} R_{IJ}A_{Jj}x_j + \sum_{J\geq K}\sum_{jk} T_{IJK}A_{Jj}x_jA_{Kk}x_k + \quad (3.86)$$

$$\sum_{J\geq K\geq L}\sum_{jkl} U_{IJKL}A_{Jj}x_jA_{Kk}x_kA_{Ll}x_l. \quad (3.87)$$

Multiplying from the left by $\mathbf{A}_{iI}^{-1}$ and summing over I yields

$$x_i \longrightarrow \sum_I A_{iI}^{-1}C_I + \sum_{IJj} A_{iI}^{-1}R_{IJ}A_{Jj}x_j + \sum_{J\geq K}\sum_{Ijk} A_{iI}^{-1}T_{IJK}A_{Jj}x_jA_{Kk}x_k +$$

$$\sum_{J\geq K\geq L}\sum_{Ijkl} A_{iI}^{-1}U_{IJKL}A_{Jj}x_jA_{Kk}x_kA_{Ll}x_l. \quad (3.88)$$

Using the fact that **A** is a diagonal matrix, this becomes

$$x_i \longrightarrow A_{ii}^{-1}C_i + \sum_j A_{ii}^{-1}R_{ij}A_{jj}x_j + \sum_{j\geq k} A_{ii}^{-1}T_{ijk}A_{jj}x_jA_{kk}x_k + \sum_{j\geq k\geq l} A_{ii}^{-1}U_{ijkl}A_{jj}x_jA_{kk}x_kA_{ll}x_l. \tag{3.89}$$

Comparison with the definition of the matrices (c, r, t, u), equation (3.63), for the normal coordinates gives

$$\begin{aligned} c_i &= A_{ii}^{-1}(\alpha_o)C_i && (3.90)\\ r_{ij} &= A_{ii}^{-1}(\alpha_o)R_{ij}A_{jj}(\alpha_o) && (3.91)\\ t_{ijk} &= A_{ii}^{-1}(\alpha_o)T_{ijk}A_{jj}(\alpha_o)A_{kk}(\alpha_o) && (3.92)\\ u_{ijkl} &= A_{ii}^{-1}(\alpha_o)U_{ijkl}A_{jj}(\alpha_o)A_{kk}(\alpha_o)A_{ll}(\alpha_o), && (3.93) \end{aligned}$$

where there are no sums in these relations, in spite of the many repeated indices. I have reasserted the dependence of **A** on α_o to emphasize it, since the importance of this result stems from this dependence. Specifically, if the matrices (C, R, T, U) for the scaled equation of motion can be found, then this last result allows one to find the matrices (c, r, t, u) for an alpha magnet run at some gradient g and for some central momentum $p_o = (\beta\gamma)_o$ such that

$$\alpha_o = \sqrt{\frac{eg}{m_e c^2 p_o}}. \tag{3.94}$$

A more easily used form of this result can be obtained by noting that

$$A_{ii} = \frac{1}{A_{ii}^{-1}} = \alpha O_i + \bar{O}_i, \tag{3.95}$$

where O_i ($\bar{O}_i$) is 1 (0) if the index i is an odd (even) integer.

The expression for the matrices becomes

$$\begin{aligned} c_i &= \frac{C_i}{O_i\alpha_o + \bar{O}_i} && (3.96)\\ r_{ij} &= \frac{R_{ij}}{O_i\alpha_o + \bar{O}_i}(O_j\alpha_o + \bar{O}_j) && (3.97)\\ t_{ijk} &= \frac{T_{ijk}}{O_i\alpha_o + \bar{O}_i}(O_j\alpha_o + \bar{O}_j)(O_k\alpha_o + \bar{O}_k) && (3.98)\\ u_{ijkl} &= \frac{U_{ijkl}}{O_i\alpha_o + \bar{O}_i}(O_j\alpha_o + \bar{O}_j)(O_k\alpha_o + \bar{O}_k)(O_l\alpha_o + \bar{O}_l). && (3.99) \end{aligned}$$

From this one can see that c_i elements may be independent of α_o or else inversely proportional to it. r_{ij} may be proportional to $\alpha_o^{-1}, \alpha_o^0$, or α_o^1. t_{ijk} may be proportional to $\alpha_o^{-1}, \alpha_o^0, \alpha_o^1$, or α_o^2. u_{ijkl} may be proportional to $\alpha_o^{-1}, \alpha_o^0, \alpha_o^1, \alpha_o^2$, or α_o^3.

3.3.6 Alternative Treatment of Dispersive Terms

I indicated above that it is not necessary to include dispersive effects in the matrix formalism for the scaled equation. The reason is that in reverting to $\mathbf{x}$, one may use α (which is a function of δ, as seen from equation (3.51)) rather than α_o, to obtain the non-dispersive matrix elements as a function of δ. This allows one to calculate the dispersive matrix elements from non-dispersive matrix elements, provided one compensates for the fact that the scaling changes the coordinate system at the vertical midplane as well as the momentum of the particle under consideration. That is, different values of α correspond to different values of $\hat{q}_1$, which enters the definition of the coordinates at the vertical midplane via equation (3.70) so that one cannot simply take derivatives of the non-dispersive matrix elements.

Let $\tilde{c}_i(\delta)$, $\tilde{r}_{ij}(\delta)$, $\tilde{t}_{ijk}(\delta)$, and $\tilde{u}_{ijkl}(\delta)$ be the matrices obtained by scaling with α, where δ is defined with respect to α_o by equation (3.51). All chromatic terms $\tilde{r}_{i6}$, $\tilde{t}_{i6k}$, $\tilde{u}_{i6kl}$, and $\tilde{u}_{i66l}$ are zero, since the chromatic dependence is now taken care of by the functional form of $\tilde{c}_i(\delta)$, $\tilde{r}_{ij}(\delta)$, $\tilde{t}_{ijk}(\delta)$, and $\tilde{u}_{ijkl}(\delta)$. The expression for transformation of a vector $\mathbf{x}$ into a vector $\bar{\mathbf{x}}$ is now

$$\bar{x}_i = \tilde{c}_i(\delta) + \sum_{4\geq j} \tilde{r}_{ij}(\delta)x_j + \sum_{4\geq j\geq k} \tilde{t}_{ijk}(\delta)x_jx_k + \sum_{4\geq j\geq k\geq l} \tilde{u}_{ijkl}(\delta)x_jx_kx_l. \tag{3.100}$$

If the matrices are for the transformation from the entrance to the exit, then there is no modification of the coordinate system with scaling, and no qualifications of this expression are needed. If the matrices are for the transformation from the entrance to the vertical midplane, then the coordinate system with respect to which $\bar{x}_i$ is defined is a function of δ also, and this must be taken into account in interpreting the results, as will be done below. If the matrices are for the transformation from the vertical midplane to the exit, then the coordinate system with respect to which x_i is defined is a function of δ; this case will not be pursued here.

Assuming, then, that the initial coordinates are not dependent (through their coordinate system or otherwise) on δ, then upon expanding $\tilde{r}_{ij}(\delta)$, $\tilde{t}_{ijk}(\delta)$, and $\tilde{u}_{ijkl}(\delta)$ in δ, one obtains

$$\begin{aligned}\bar{x}_i \;=\; & (\tilde{c}_i)_{\delta=0} + \delta\left(\frac{\partial \tilde{c}_i}{\partial \delta}\right)_{\delta=0} + \frac{1}{2!}\delta^2\left(\frac{\partial^2 \tilde{c}_i}{\partial \delta^2}\right)_{\delta=0} + \frac{1}{3!}\delta^3\left(\frac{\partial^3 \tilde{c}_i}{\partial \delta^3}\right)_{\delta=0} \\ & + \sum_{4\geq j}\left\{(\tilde{r}_{ij})_{\delta=0} + \delta\left(\frac{\partial \tilde{r}_{ij}}{\partial \delta}\right)_{\delta=0} + \frac{1}{2!}\delta^2\left(\frac{\partial^2 \tilde{r}_{ij}}{\partial \delta^2}\right)_{\delta=0}\right\} x_j \\ & + \sum_{4\geq j\geq k}\left\{\left(\tilde{t}_{ijk}\right)_{\delta=0} + \delta\left(\frac{\partial \tilde{t}_{ijk}}{\partial \delta}\right)_{\delta=0}\right\} x_j x_k + \sum_{4\geq j\geq k\geq l}(\tilde{u}_{ijkl})_{\delta=0}\, x_j x_k x_l,\end{aligned} \tag{3.101}$$

where I work to third order and where $\bar{x}_i$ may contain effects of coordinate system changes with δ. For transformations from the entrance to the exit, the $\bar{x}_i$ are unaffected by coordinate system changes. For transformations to the vertical midplane, it is only $\bar{x}_1$ that is affected by coordinate system scaling, through scaling of $\hat{q}_1$. Hence, I shall momentarily ignore coordinate system dependencies and equate $\bar{x}_i$ with the true coordinates in the proper reference frame. I shall then return to treat the case of $\bar{x}_1$ for transport to the vertical midplane separately.

Taking equation (3.102) literally, then, one can identify the chromatic matrix elements as

$$r_{i6} = \left(\frac{\partial}{\partial \delta}\tilde{c}_i(\alpha)\right)_{\delta=0} \tag{3.102}$$

$$t_{i66} = \frac{1}{2!}\left(\frac{\partial^2}{\partial \delta}\tilde{c}_i(\alpha)\right)_{\delta=0} \tag{3.103}$$

$$u_{i666} = \frac{1}{3!}\left(\frac{\partial^3}{\partial \delta^3}\tilde{c}_i(\alpha)\right)_{\delta=0} \tag{3.104}$$

$$t_{i6j} = \left(\frac{\partial}{\partial \delta}\tilde{r}_{ij}(\alpha)\right)_{\delta=0} \tag{3.105}$$

$$u_{i66j} = \frac{1}{2!}\left(\frac{\partial^2}{\partial \delta^2}\tilde{r}_{ij}(\alpha)\right)_{\delta=0} \tag{3.106}$$

$$u_{i6kj} = \left(\frac{\partial}{\partial \delta}\tilde{t}_{ijk}(\alpha)\right)_{\delta=0} \tag{3.107}$$

To treat the case of $\bar{x}_1$ for transport to the vertical midplane, I rewrite equation (3.100) for $i = 1$ as

$$\bar{x}_1 = \hat{q}_1(\alpha) - q_1^{\text{midplane}} = \tilde{c}_1(\delta) + \sum_{6>j}\tilde{r}_{1j}(\delta)x_j + \sum_{6>j\geq k}\tilde{t}_{1jk}(\delta)x_j x_k + \sum_{6>j\geq k\geq l}\tilde{u}_{1jkl}(\delta)x_j x_k x_l, \tag{3.108}$$

The actual coordinate of interest is not $\bar{x}_1$ but rather $\check{x}_1 \equiv \hat{q}_1(\alpha_o) - q_1^{\mathrm{midplane}}$, where q_1^{midplane} is, of course, a function of α. Adding $\hat{q}_1(\alpha_o) - \hat{q}_1(\alpha)$ to both sides of equation (3.108), I obtain

$$\check{x}_1 = \hat{q}_1(\alpha_o) - \hat{q}_1(\alpha) + \tilde{c}_1(\delta) + \sum_{6>j} \tilde{r}_{1j}(\delta)x_j + \sum_{6>j\geq k} \tilde{t}_{1jk}(\delta)x_jx_k + \sum_{6>j\geq k\geq l} \tilde{u}_{1jkl}(\delta)x_jx_kx_l, \tag{3.109}$$

which, when expanded in δ, yields additional terms not listed in equations (3.102) through (3.107), without modifying those that are listed. These additional matrix elements are none other than those resulting from the expansion of $-\hat{q}_1(\alpha)$, which have already been exhibited in the last section, as equations (3.53) through (3.57).

So far, these results would seem to apply only to the matrices (c, r, t, u) and not to (C, R, T, U). However, if one takes $\alpha_o = 1$, one sees that the matrices (c, r, t, u) are numerically equal to (C, R, T, U), from which it follows that the numerical relationships between the chromatic and non-chromatic elements are the same for (C, R, T, U) as for the (c, r, t, u). Another way of realizing that this is so is to notice that c_i, r_{i6}, t_{i66}, and u_{i666} all have the same scaling with α_o, as do r_{ij}, t_{i6j}, and u_{i6jk}, and also t_{ijk} and u_{i6jk} This can be seen from equations (3.96) through (3.99).

An example may make all this clearer. Consider the element t_{162}, which is given by

$$t_{162}(\alpha_o) = \left(\frac{\partial}{\partial\delta} r_{12}(\alpha)\right)_{(\delta=0)} \tag{3.110}$$

$$= \left(\frac{\partial}{\partial\delta}(r_{12}(\alpha_o)\sqrt{1+\delta})\right)_{(\delta=0)} \tag{3.111}$$

$$= \frac{1}{2} r_{12}(\alpha_o). \tag{3.112}$$

Since

$$T_{162} = \frac{t_{162}(\alpha_o)}{\alpha_o} \tag{3.113}$$

and

$$R_{12} = \frac{r_{12}(\alpha_o)}{\alpha_o}, \tag{3.114}$$

it also follows that

$$T_{162} = \frac{1}{2} R_{12}. \tag{3.115}$$

For rapid checks on calculated matrices, or for inclusion in a computer program, it is convenient to work out the consequences of these relations for the matrices (C, R, T, U). I have done this, and the results are

$$\mathrm{R}_{56} = \frac{1}{2}\mathrm{C}_5, \tag{3.116}$$

$$\mathrm{T}_{566} = -\frac{1}{8}\mathrm{C}_5, \tag{3.117}$$

$$\mathrm{U}_{5666} = \frac{1}{16}\mathrm{C}_5, \tag{3.118}$$

$$\mathrm{T}_{\mathrm{I6J}} = \frac{1}{2}\mathrm{R}_{\mathrm{IJ}}(\mathrm{O}_\mathrm{I}\bar{\mathrm{O}}_\mathrm{J} - \bar{\mathrm{O}}_\mathrm{I}\mathrm{O}_\mathrm{J}), \tag{3.119}$$

$$\mathrm{U}_{\mathrm{I66J}} = \frac{1}{8}\mathrm{R}_{\mathrm{IJ}}(3\bar{\mathrm{O}}_\mathrm{I}\mathrm{O}_\mathrm{J} - \mathrm{O}_\mathrm{I}\bar{\mathrm{O}}_\mathrm{J}), \tag{3.120}$$

and

$$\mathrm{U}_{\mathrm{I6JK}} = \frac{1}{2}\mathrm{T}_{\mathrm{IJK}}\left[\mathrm{O}_\mathrm{I}\bar{\mathrm{O}}_\mathrm{J}\bar{\mathrm{O}}_\mathrm{K} - \mathrm{O}_\mathrm{I}\mathrm{O}_\mathrm{J}\mathrm{O}_\mathrm{K} - \bar{\mathrm{O}}_\mathrm{I}(\mathrm{O}_\mathrm{J}\bar{\mathrm{O}}_\mathrm{K} + \bar{\mathrm{O}}_\mathrm{J}\mathrm{O}_\mathrm{K}) - 2\bar{\mathrm{O}}_\mathrm{I}\mathrm{O}_\mathrm{J}\mathrm{O}_\mathrm{K}\right], \tag{3.121}$$

where O_I ($\bar{\mathrm{O}}_\mathrm{I}$) is 1 if I is odd (even) and zero otherwise, and where $6 > \mathrm{J} \geq \mathrm{K}$. (I emphasize again that these results are invalid for transport from the vertical midplane to the exit, which is a case I have not treated here.)

3.4 Transport Matrices from Numerical Integration

The scaled transport matrices (C, R, T, U) for the alpha-magnet can be found from numerical integration of the scaled equation of motion (equation (3.83)) and fitting. The technique I have used is not confined in its application to the alpha-magnet, though it is most appropriate for elements for which there exists an equivalent of the scaled equation of motion for the alpha magnet. Essentially, an ensemble of N initial vectors, labeled $\mathbf{X}^{(i)}$, $i = 1, 2, \ldots N$ is mapped into an ensemble of final vectors, labeled $\mathbf{Y}^{(i)}$, by numerical integration starting and ending at the appropriate reference planes. These vectors are then required to satisfy

$$\mathrm{Y}_{\mathrm{I}}^{(i)} = \mathrm{C}_{\mathrm{I}} + \sum_{\mathrm{J}} \mathrm{R}_{\mathrm{IJ}} \mathrm{X}_{\mathrm{J}}^{(i)} + \sum_{\mathrm{J} \geq \mathrm{K}} \mathrm{T}_{\mathrm{IJK}} \mathrm{X}_{\mathrm{J}}^{(i)} \mathrm{X}_{\mathrm{K}}^{(i)} + \sum_{\mathrm{J} \geq \mathrm{K} \geq \mathrm{L}} \mathrm{U}_{\mathrm{IJKL}} \mathrm{X}_{\mathrm{J}}^{(i)} \mathrm{X}_{\mathrm{K}}^{(i)} \mathrm{X}_{\mathrm{L}}^{(i)} +$$

$$\sum_{\mathrm{J} \geq \mathrm{K} \geq \mathrm{L} \geq \mathrm{M}} \mathrm{V}_{\mathrm{IJKLM}} \mathrm{X}_{\mathrm{J}}^{(i)} \mathrm{X}_{\mathrm{K}}^{(i)} \mathrm{X}_{\mathrm{L}}^{(i)} \mathrm{X}_{\mathrm{M}}^{(i)} + \mathcal{O}((\mathbf{X}^{(i)})^5), \tag{3.122}$$

which is essentially the definition of the transport matrices, where I've included a fourth-order matrix V. I emphasize that the $\mathbf{Y}^{(i)}$ are not *calculated from* this matrix expression, but are rather being approximated by it, having been calculated by numerical integration of the equation of motion with initial condition $\mathbf{X}^{(i)}$. I am including the fourth-order terms explicitly in order to show how to prevent fourth-order influences from corrupting the computation of (C, R, T, U). The fifth-order terms will be assumed to be negligible.

3.4.1 One-Variable Terms

In principle, one could fit this by finding the (C, R, T, U) that minimized the sum of the squared deviations of the right-hand-side from the left-hand-side. In practice, this is computationally difficult and also extremely inefficient. To see a more efficient procedure, imagine that one was only interested in calculating C_{I}. Clearly, one would only need to track the fiducial particle.

At first sight, one might think that one could then go on to find R_{IJ} by finding $\mathbf{Y}$ for each vector of an ensemble, $\mathbf{X}^{(\mathrm{J})}$, of initial vectors, each of which had only a non-zero J^{th} component:

$$\mathbf{X}^{(J)} = a_J \mathbf{e}_J, \tag{3.123}$$

with $J = 1\ldots6$, a_J a constant, and $\mathbf{e}_J$ the unit vector for the J^{th} component of $\mathbf{X}$. In fact, the $Y_I^{(J)}$ values thus obtained would include the influence of not only R_{IJ}, but also of all non-zero T_{IJJ}, U_{IJJJ}, and V_{IJJJJ} matrix elements:

$$Y_I^{(i)} = C_I + R_{IJ}a_J + T_{IJJ}a_J^2 + U_{IJJJ}a_J^3 + V_{IJJJJ}a_J^4 + \mathcal{O}(a_J^5). \tag{3.124}$$

Obviously, one can extract C_I, R_{IJ}, T_{IJJ}, and U_{IJJJ} by fitting a fourth-order polynomial to this form (assuming that terms of fifth-order and higher can be ignored), if one takes a sufficient number of values of a_J for each J. A minimum of five initial vectors are needed for each value of J. Since I consider only static systems, J=5 (i.e., path-length dependent) terms are all zero, so a minimum of twenty-five vectors needs to be integrated. As I will discuss below, I use N vectors per component J, with N odd and $N \geq 5$:

$$\mathbf{X}^{(J,j)} = (j - \frac{N+1}{2})a_J\mathbf{e}_J, \quad j = 1\ldots5. \tag{3.125}$$

The reason for this particular choice of $\mathbf{X}^{(J,j)}$, which is symmetric about and includes the origin, will become apparent below. a_J is chosen sufficiently small so as to avoid large contributions to $\mathbf{Y}$ from terms higher than fifth order, while obtaining reasonable influence from third order terms, so that fitting will yield sufficiently precise values for the third-order coefficients. This step gives all elements C_I, R_{IJ}, T_{IJJ}, U_{IJJJ}, and, as a useful bonus, V_{IJJJJ}. It remains to find $T_{IJK} = T_{IKJ}$, $U_{IJKK} = U_{IKJK} = U_{IKKJ}$, and U_{IJKL}, for $J > K$ and $K > L$.

3.4.2 Two-Variable Terms

To find T_{IJK} and U_{IJKK}, I integrate the equations of motion for a new ensemble of initial vectors for each (J, K) pair with $J > K$, described by

$$\mathbf{X}^{(J,j,K,k)} = (j - \frac{N+1}{2})a_J\mathbf{e}_J + (-1)^k a_K\mathbf{e}_K, \tag{3.126}$$

where $j = 1\ldots N$, $k = 1$ or 2, N is an odd integer, and a_J and a_K are constants.

I now construct a residual final vector, $\Delta\mathbf{Y}^{(J,j,K,k)}$ for each $\mathbf{X}^{(J,j,K,k)}$ by subtracting off the contributions of the known matrix elements.

$$\begin{aligned}\Delta Y_I^{(J,j,K,k)} &= Y_I^{(J,j,K,k)} - C_I - \sum_M \left\{R_{IM}X_M + T_{IMM}X_M^2 + U_{IMMM}X_M^3 + V_{IMMM}X_M^4\right\} \\ &= T_{IJK}X_JX_K + U_{IJJK}(X_J)^2X_K + U_{IJKK}X_J(X_K)^2 \\ &\quad +V_{IJJJK}(X_J)^3X_K + V_{IJJKK}(X_JX_K)^2 + V_{IJKKK}X_J(X_K)^3 \\ &\quad +\mathcal{O}(\mathbf{X}^5), \end{aligned} \tag{3.127}$$

where for brevity $\mathbf{X} \equiv \mathbf{X}^{(J,j,K,k)}$ in this equation. Using equation (3.126) and dropping terms of fifth order and higher, this becomes

$$\begin{aligned}\Delta Y_I^{(J,j,K,k)} &= T_{IJK}(j - \frac{N+1}{2})a_J(-1)^k a_K + U_{IJJK}((j - \frac{N+1}{2})a_J)^2(-1)^k a_K + \\ &\quad U_{IJKK}(j - \frac{N+1}{2})a_J a_K^2 + V_{IJKKK}(j - \frac{N+1}{2})a_J(-1)^k a_K^3 + \\ &\quad V_{IJJKK}((j - \frac{N+1}{2})a_J)^2 a_K^2 + V_{IJJJK}((j - \frac{N+1}{2})a_J)^3(-1)^k a_K \end{aligned} \tag{3.128}$$

I define the sum and difference of the residuals for k=1 and k=2 as

$$\Delta\mathbf{Y}^{(J,j,K,S)} \equiv \Delta\mathbf{Y}^{(J,j,K,2)} + \Delta\mathbf{Y}^{(J,j,K,1)} \tag{3.129}$$

and

$$\Delta\mathbf{Y}^{(J,j,K,D)} \equiv \Delta\mathbf{Y}^{(J,j,K,2)} - \Delta\mathbf{Y}^{(J,j,K,1)}. \tag{3.130}$$

Using equation (3.128), these evaluate to

$$\Delta\mathbf{Y}^{(J,j,K,S)} = 2U_{IJKK}(j - \frac{N+1}{2})a_J a_K^2 + 2V_{IJJKK}((j - \frac{N+1}{2})a_J)^2 a_K^2 \tag{3.131}$$

and

$$\begin{aligned}\Delta\mathbf{Y}^{(J,j,K,D)} &= 2T_{IJK}(j - \frac{N+1}{2})a_J a_K + 2U_{IJJK}((j - \frac{N+1}{2})a_J)^2 a_K + \\ &\quad 2V_{IJKKK}(j - \frac{N+1}{2})a_J a_K^3 + 2V_{IJJJK}((j - \frac{N+1}{2})a_J)^3 a_K \end{aligned} \tag{3.132}$$

From equation (3.131), one can find U_{IJKK} and V_{IJJKK} from the linear and quadratic terms, respectively, of a fit that is quadratic in $(j - \frac{N+1}{2})a_J$. Similarly, equation (3.132) indicates that one can find $T_{IJK} + a_K^2 V_{IJKKK}$ and U_{IJJK} from the linear and quadratic terms of a fit that is cubic in $(j - \frac{N+1}{2})a_J$. By doing the analysis for two different values of a_K, one can separate T_{IJK} from $T_{IJK} + a_K^2 V_{IJKKK}$. For a general element, then, at the very least one needs twenty integrations (i.e., N=5, two values of a_K, j=1,2) for every pair (J, K), for $J > K$, or $20 * 15 = 300$ integrations. (The twenty is the number of integrations per pair; the fifteen is the number of (J, K) pairs such that $6 \geq J > K \geq 1$.) Since the elements with J=5 or K=5 are known beforehand to be zero for a static element, this is reduced to a minimum of $20 * 10 = 200$ integrations for the alpha-magnet.

3.4.3 Three-Variable Terms

Having completed this step, only the elements U_{IJKL} with $J > K$ and $K > L$ remain to be found. To obtain these, new initial vectors are chosen for each triplet (J, K, L) with $J > K > L$:

$$\mathbf{X}^{(J,K,L,i)} = (-1)^i (a_J \mathbf{e}_J + a_K \mathbf{e}_K + a_L \mathbf{e}_L), \tag{3.133}$$

where i is 1 or 2, and a_J, a_K, and a_L are constants.

Again, I compute residual final vectors $\Delta\mathbf{Y}^{(J,K,L,i)}$ by subtracting off the contributions of all R, T, and U matrix elements calculated so far:

$$\begin{aligned}
\Delta Y_I^{(J,K,L,i)} \equiv\ & Y_I^{(J,K,L,i)} - C_I - \sum_N \left\{ R_{IN}X_N + T_{INN}X_N^2 + U_{INNN}X_N^3 + V_{INNNN}X_N^4 \right\} \\
& - \sum_{N>M} \left\{ T_{INM}X_N X_M + (U_{INMM}X_N(X_M)^2 + U_{INNM}(X_N)^2 X_M) \right\} \\
=\ & \sum_{N>M>P} U_{INMP}X_N X_M X_P + \sum_{N>M} V_{INNMM}(X_N X_M)^2 \\
& + \sum_{N>M>P} \left\{ V_{INMPP}X_N X_M X_P^2 + V_{INMMP}X_N X_M^2 X_P + V_{INNMP}X_N^2 X_M X_P \right\} \\
& + \mathcal{O}(\mathbf{X}^5),
\end{aligned} \tag{3.134}$$

where for brevity $\mathbf{X} \equiv \mathbf{X}^{(J,K,L,i)}$ in this equation. Using equation (3.133) and dropping terms of fifth order and higher, this becomes

$$\begin{aligned}
\Delta Y_I^{(i)} =\ & U_{IJKL}a_J a_K a_L (-1)^i + \\
& (V_{IJJKK}a_J^2 a_K^2 + V_{IJJLL}a_J^2 a_L^2 + V_{IKKLL}a_K^2 a_L^2) + \\
& (V_{IJKLL}a_J a_K a_L^2 + 12V_{IJKKL}a_J a_K^2 a_L^2 + V_{IJJKL}a_J^2 a_K a_L).
\end{aligned} \tag{3.135}$$

I now form the difference of the residuals for i=2 and i=1, obtaining

$$\Delta Y_I^{(D)} \equiv Y_I^{(2)} - Y_I^{(1)} = 2U_{IJKL}a_J a_K a_L. \tag{3.136}$$

Thus, one can obtain the U_{IJKL} with $J > K$ and $K > L$ by integrating a two additional vectors for each triplet $J > K > L$, requiring 40 additional integrations for a general element. For a static element, $U_{IJKL} = 0$ for J=5, K=5, or L=5, which reduces the number of additional integrations to 20.

3.4.4 Initial-Vector Ensemble

The reader may have noticed that the ensembles specified by equations (3.125), (3.126), and (3.133) overlap. Because of this, it is possible to use the ensemble of vectors defined by

$$\mathbf{X}^{(J,j,K,k,L,l)} = (\frac{N_J+1}{2} - j)a_J\mathbf{e}_J + (\frac{N_K+1}{2} - k)a_K\mathbf{e}_K + (\frac{N_L+1}{2} - l)a_L\mathbf{e}_L, \tag{3.137}$$

with N_J odd, $6 \geq J > K > L \geq 1$, and j, k, and l taking integer values between $-(N-1)/2$ and $(N-1)/2$ (where $N = N_J$, N_K, or N_L, for j, k, and l, respectively) except that $j = k = l = 0$ (the null vector) appears only once for all triplets (J, K, L). The maximum amplitude of the J^{th} vector component is

$$M_J = \frac{N_J - 1}{2}a_J. \tag{3.138}$$

Since for a static element, X_5 is irrelevant, one can choose $N_5 = 1$ and $a_5 = 0$. It is also convenient to choose $N_J = N$ for all $J \neq 5$. Given both of these choices, the number of vectors in the ensemble is

$$10(N^3 - 1) + 10(N^2 - 1) + 1, \tag{3.139}$$

where I count ten (J, K, L) triplets with neither J, K, nor L equal to 5, contributing $N^3 - 1$ vectors each, exclusive of the null vector; ten (J, K, L) triplets with one of J, K, or L equal to 5, contributing $N^2 - 1$ vectors each, exclusive of the null vector; plus one null vector.

For $N = 5$ this ensemble contains about 6 times as many vectors as the minimum needed, but using it has the advantage of simplicity of coding and also of providing additional data to improve the accuracy of some of the elements by averaging.

Doubtless a more computationally efficient ensemble could be coded than I have used in my codes.

Having assembled this ensemble, one integrates each initial vector to obtain the corresponding final vector. One then selects out the necessary sub-ensembles corresponding to equation (3.125), (3.126), or (3.133)) for each stage of the analysis.

3.4.5 Accuracy Considerations and Limits

I have taken pains in the above analysis to eliminate the influence of fourth-order terms in order to increase the accuracy of the third-order matrix. In addition, suitable choice of the constants a_J can ensure that the effects of fourth and higher-order terms are negligible. "Suitable" must be determined empirically, or by reference to the magnitude of the matrix elements once they are roughly known. A starting point is to assume that the dominant fourth-order matrix elements have magnitudes similar to those of dominant matrix elements of third-order, from which one would conclude that that $M_J = 10^{-3}$ would be suitable to obtain 0.1% accuracy of the third-order results, even without the corrections for the V matrix that are included in the equations. Further, fifth order terms would be expected have an influence of one part in a million relative to the third-order. If similar results are obtained for a wide range of values of M_J, then one can conclude that the influence of higher-order terms is indeed negligible. In addition, if the contributions of the first, second, and third-order matrices to the final coordinates $\mathbf{Y}$ are seen to be different by several orders of magnitude between successive orders, then one can reasonably conclude that higher-order effects are several orders of magnitude below the third-order effects.

Invariably the above procedure will yield some small, non-zero matrix elements which may or may not be genuine, due to the accumulation of inaccuracies in the integration, subtraction of higher-order terms, and fitting. If one knows that the accuracy of any integration is of order 10^{-p}, where p is an integer, then one can conclude that a computed matrix element is spurious if it fails to satisfy the appropriate criterion (depending on the order of the matrix element) from the following list:

$$R_{IJ}M_J > 10^{-p} \tag{3.140}$$

$$T_{IJK}M_JM_K > 10^{-p} \tag{3.141}$$

$$U_{IJKL} M_J M_K M_L \quad > \quad 10^{-p}. \tag{3.142}$$

One can also use these same relations to estimate the resolution with which genuine non-zero matrix elements could be calculated.

$$\Delta R_{IJ} \quad > \quad \frac{10^{-p}}{M_J} \tag{3.143}$$

$$\Delta T_{IJK} \quad > \quad \frac{10^{-p}}{M_J M_K} \tag{3.144}$$

$$\Delta U_{IJKL} \quad > \quad \frac{10^{-p}}{M_J M_K M_L}. \tag{3.145}$$

One expects that this resolution will not be achieved, since it does not consider the inaccuracies in fitting and subtraction to obtain residuals. Nevertheless, these criteria do provide a solid lower bound on the precision of the matrix elements. In the case of the alpha-magnet, I have shown above that the accuracy of integrations is 10^{-14}.

3.5 Transport Matrices for the Alpha Magnet

I have written a computer program, **salpha_matrix**, that implements the ideas of the previous two sections. Matrices up to third order have been computed for transport from the entrance of the alpha-magnet to the exit, from the entrance to the vertical midplane, and from the vertical midplane to the exit.

3.5.1 Program Tests and Choice of Initial Amplitudes

For purposes of testing the coding and the method of obtaining the matrix, the program has the option of generating C, R, T, and U matrices with all components given by random numbers between -1 and 1, and then tracking vectors through these matrices instead of integrating the equations of motion for the alpha magnet. It then attempts to recover the random matrices by analyzing the initial and final vectors only, just as would be done for initial and final vectors obtained by integration. This tests the ability of the program to separate various orders, but does not test its ability to suppress the effects of orders higher than third. Table 3.2 summarizes the results of this test. As will be seen, the errors are below those that are encountered in fitting matrices for the alpha-magnet, as would be expected. The errors from this procedure can be considered to place the ultimate limit on the accuracy with which matrices for the alpha-magnet can be calculated.

Table 3.2: **Accuracy of Recovery of a Randomly Generated Matrix**

matrix	maximum error of fit for any matrix element	average deviation of fit for all matrix elements
C	$1.38 \cdot 10^{-17}$	$7.59 \cdot 10^{-18}$
R	$8.87 \cdot 10^{-14}$	$2.71 \cdot 10^{-14}$
T	$1.13 \cdot 10^{-10}$	$2.48 \cdot 10^{-11}$
U	$1.47 \cdot 10^{-7}$	$1.77 \cdot 10^{-8}$

An initial round of computations for the alpha-magnet were done with N = 5 and with all M_J values equal, for a series of different values from 10^{-2} to 10^{-5}. After the matrix was obtained, the average of the absolute values of the residuals of the final vectors for all initial vectors were computed to assess the degree to which the fits contained sufficiently high-order terms to match the actual final vectors. Residuals were computed by successively adding linear, second-order, and third-order terms to assess the effect of each order. The average absolute residuals for n^{th} order are simply

$$\mathcal{R}_I^{(n)} = \frac{1}{M}\sum_i \left| Y_I^{(i)} - \left\{ C_I + \sum_J R_{IJ} X_J^{(i)} + (n > 1?) \sum_{J \geq K} T_{IJK} X_J^{(i)} X_K^{(i)} + \right.\right. \quad (3.146)$$

$$\left.\left. (n > 2?) \sum_{J \geq K \geq L} U_{IJKL} X_I^{(i)} X_J^{(i)} X_K^{(i)} \right\} \right|, \quad (3.147)$$

where the index i runs over all M initial vectors in the ensemble specified by equation (3.137), and $(n > m?)$ represents a function that returns 1 if $n > m$ and 0 otherwise. Table 3.3 summarizes some of the results. ($\mathcal{R}_6^{(n)}$ is identically zero, since the momentum is not changed by the magnet, and hence is not listed.) It is no coincidence that for any particular I and n, $\mathcal{R}_I^{(n)}$ varies with M_J according to M_J^{n+1}, since for valid fits (i.e., those that don't err by compromising lower order coefficients in order to match higher-order contributions) $\mathcal{R}_I^{(n)}$ is simply the average contribution of the $(n+1)^{th}$ order terms.

Table 3.3: **Residuals from Matrix Fits**

n	M_J	$\mathcal{R}_1^{(n)}$	$\mathcal{R}_2^{(n)}$	$\mathcal{R}_3^{(n)}$	$\mathcal{R}_4^{(n)}$	$\mathcal{R}_5^{(n)}$
1	10^{-2}	$1.84 \cdot 10^{-3}$	$1.89 \cdot 10^{-3}$	$4.51 \cdot 10^{-4}$	$3.79 \cdot 10^{-4}$	$7.63 \cdot 10^{-5}$
1	10^{-3}	$1.84 \cdot 10^{-5}$	$1.89 \cdot 10^{-5}$	$4.49 \cdot 10^{-6}$	$3.53 \cdot 10^{-6}$	$7.76 \cdot 10^{-7}$
1	10^{-4}	$1.84 \cdot 10^{-7}$	$1.90 \cdot 10^{-7}$	$4.49 \cdot 10^{-8}$	$3.51 \cdot 10^{-8}$	$7.76 \cdot 10^{-9}$
2	10^{-2}	$3.44 \cdot 10^{-5}$	$2.39 \cdot 10^{-5}$	$4.59 \cdot 10^{-5}$	$1.43 \cdot 10^{-4}$	$6.38 \cdot 10^{-6}$
2	10^{-3}	$3.44 \cdot 10^{-8}$	$2.39 \cdot 10^{-8}$	$4.61 \cdot 10^{-8}$	$1.43 \cdot 10^{-7}$	$6.34 \cdot 10^{-9}$
2	10^{-4}	$3.44 \cdot 10^{-11}$	$2.39 \cdot 10^{-11}$	$4.61 \cdot 10^{-11}$	$1.42 \cdot 10^{-10}$	$6.34 \cdot 10^{-12}$
3	10^{-2}	$9.40 \cdot 10^{-7}$	$8.78 \cdot 10^{-7}$	$2.08 \cdot 10^{-6}$	$2.37 \cdot 10^{-6}$	$7.19 \cdot 10^{-7}$
3	10^{-3}	$8.98 \cdot 10^{-11}$	$8.43 \cdot 10^{-11}$	$2.08 \cdot 10^{-10}$	$2.36 \cdot 10^{-10}$	$7.21 \cdot 10^{-11}$
3	10^{-4}	$1.14 \cdot 10^{-14}$	$1.01 \cdot 10^{-14}$	$2.07 \cdot 10^{-14}$	$2.36 \cdot 10^{-14}$	$7.40 \cdot 10^{-15}$

Table 3.3 shows that for $M_J = 10^{-4}$, the third-order residuals are of order 10^{-14}, which is the accuracy limit of the integrations. Hence, fourth-order contributions are "in the noise", and third-order contributions are three orders of magnitude above it. I find that for such small M_J values, the chromatic terms do not follow equations (3.102)

through (3.107) as well as for $M_J = 10^{-3}$. For this reason, I choose the matrices computed with $M_J = 10^{-3}$ as the most accurate. Analysis of the chromatic terms indicates that the T matrix elements are accurate to about 10^{-6}, indicating that p in equations (3.143) through (3.145) is 12 (rather than 14 as would be thought from the accuracy of the integration). I use this value of p in order to "filter" small T_{IJK} and U_{IJKL} values for significance, as per equations (3.140) through (3.142). That is, T_{IJK} values smaller than 10^{-6} and U_{IJKL} values smaller than 10^{-3} are taken to be zero.

3.5.2 Final Results

Having verified the program's matrix-fitting algorithm and found the limits of its accuracy, I computed the matrices for the alpha magnet using N = 7. I used an accuracy limit of 5×10^{-13} to filter out spurious non-zero matrix elements. This limit is a compromise between one that is somewhat too large for the T matrix elements, and somewhat too small for the U matrix elements. Hence, some small, dubious U matrix elements will appear in the results that follow.

Checks of the Results

A number of checks have been made on these matrices. The determinants of the first order matrices for entrance-to-exit, entrance-to-vertical midplane, and vertical midplane-to-exit have been found to be 1 to within 2×10^{-12}. (This accuracy is not fully reflected in the results given below, since I have not quoted a sufficient number of significant figures. Also, the reader should beware of checking this claim with a hand calculator, since many use only 10 or 11 digits.)

The relationships between the non-chromatic and chromatic terms were used to evaluate the accuracy of the method, as discussed above; the reader is invited to use equations (3.102) through (3.107) and (3.53) through (3.60) to verify for himself that the results do indeed satisfy the expected numerical ratios. As a sample, for the matrix from the entrance to the vertical midplane, I find that

$$\frac{R_{56}}{C_5} = \frac{1}{2} + 2 \cdot 10^{-12} \tag{3.148}$$

$$\frac{T_{566}}{C_5} = -\frac{1}{8} - 6 \cdot 10^{-10} \tag{3.149}$$

$$\frac{U_{5666}}{C_5} = \frac{1}{16} - 2 \cdot 10^{-8} \tag{3.150}$$
$$\frac{T_{162}}{R_{12}} = \frac{1}{2} - 2 \cdot 10^{-9} \tag{3.151}$$
$$\frac{U_{1662}}{R_{12}} = -\frac{1}{8} - 6 \cdot 10^{-6}. \tag{3.152}$$

The reader will see below that the computed entrance-to-vertical midplane and vertical midplane-to-exit R matrices satisfy the expected relationship for two elements that are the reverse of each other[6], namely

$$\tilde{R} = \begin{pmatrix} R_{22} & R_{12} \\ R_{21} & R_{11} \end{pmatrix}, \tag{3.153}$$

where $\tilde{R}$ is the matrix for system that is reversed in order relative to the system for which R is the matrix.

The matrices for the first and second parts of the alpha-magnet were concatenated (using a third-order matrix concatenation program written by the author) and compared to the matrices computed for the full magnet. No significant discrepancies were found for the R matrix. The only discrepancies found in the T matrix were fractional variations of 10^{-5} in the two smallest elements; all other T matrix elements either showed no discrepancy, or discrepancies only in the last decimal place. For most U matrix elements, the discrepancy was less than .1 %, while for a few of the smallest U matrix elements, the error was between 1 and 10 %.

In order to ensure that there were no transcription errors made, `salpha_matrix` provided output in LaTeX format, which was included in this document with only minor editing to properly columnate the data.

Entrance-to-Exit Transport

For transport from the entrance to the exit, tables 3.4 and 3.5 list non-zero T and U matrix elements, respectively. The following are the centroid and R matrix elements (unlisted elements are zero):

$$C_5 = 4.642099465061 \tag{3.154}$$

$$R_{56} = 2.321049733 \tag{3.155}$$

$$\begin{pmatrix} R_{11} & R_{12} \\ R_{21} & R_{22} \end{pmatrix} = \begin{pmatrix} -1.000000000 & -2.321049733 \\ 0.000000000 & -1.000000000 \end{pmatrix} \tag{3.156}$$

$$\begin{pmatrix} R_{33} & R_{34} \\ R_{43} & R_{44} \end{pmatrix} = \begin{pmatrix} -0.7371140937 & 7.618204274 \\ -0.05994362928 & -0.7371140937 \end{pmatrix} \tag{3.157}$$

Table 3.4: **Non-zero T Matrix Elements from Entrance to Exit**

$T_{122} = -9.985582 \cdot 10^{-1}$	$T_{133} = -6.047097 \cdot 10^{-1}$	$T_{143} = -6.415746$
$T_{144} = 3.782911 \cdot 10^{1}$	$T_{162} = -1.160525$	$T_{233} = -2.996743 \cdot 10^{-1}$
$T_{243} = -7.370063$	$T_{244} = 3.808545 \cdot 10^{1}$	$T_{331} = -5.157770 \cdot 10^{-2}$
$T_{332} = 9.264364$	$T_{342} = 6.892273$	$T_{364} = 3.809102$
$T_{432} = -1.750135$	$T_{441} = 5.157770 \cdot 10^{-2}$	$T_{442} = 9.384079$
$T_{463} = 2.997181 \cdot 10^{-2}$	$T_{522} = 5.802624 \cdot 10^{-1}$	$T_{533} = 1.104632 \cdot 10^{-2}$
$T_{543} = -2.283314 \cdot 10^{-1}$	$T_{544} = -1.403871$	$T_{566} = -5.802624 \cdot 10^{-1}$

Table 3.5: **Non-zero U Matrix Elements from Entrance to Exit**

$U_{1222} = 9.634 \cdot 10^{-1}$	$U_{1331} = -2.579 \cdot 10^{-1}$	$U_{1332} = -8.573$
$U_{1431} = -5.301$	$U_{1432} = 8.263 \cdot 10^{1}$	$U_{1441} = 3.829 \cdot 10^{1}$
$U_{1442} = 9.435 \cdot 10^{1}$	$U_{1622} = -4.993 \cdot 10^{-1}$	$U_{1633} = 3.023 \cdot 10^{-1}$
$U_{1644} = 1.891 \cdot 10^{1}$	$U_{1662} = 2.901 \cdot 10^{-1}$	$U_{2332} = -8.779$
$U_{2431} = 5.157 \cdot 10^{-1}$	$U_{2432} = 9.310 \cdot 10^{1}$	$U_{2441} = 6.341$
$U_{2442} = 4.557 \cdot 10^{1}$	$U_{2633} = 2.997 \cdot 10^{-1}$	$U_{2643} = 3.685$
$U_{3321} = -1.462$	$U_{3322} = -4.979 \cdot 10^{-1}$	$U_{3333} = 1.047$
$U_{3411} = 4.431 \cdot 10^{-2}$	$U_{3421} = 1.033 \cdot 10^{-1}$	$U_{3422} = 1.101 \cdot 10^{1}$
$U_{3432} = -2.705 \cdot 10^{-3}$	$U_{3433} = -2.310$	$U_{3443} = 2.220 \cdot 10^{1}$
$U_{3444} = -1.075 \cdot 10^{2}$	$U_{3631} = 2.579 \cdot 10^{-2}$	$U_{3642} = 3.446$
$U_{3664} = -9.523 \cdot 10^{-1}$	$U_{4322} = 1.285 \cdot 10^{1}$	$U_{4333} = -4.323 \cdot 10^{-1}$
$U_{4421} = 1.463$	$U_{4422} = 2.946$	$U_{4432} = -1.636 \cdot 10^{-3}$
$U_{4433} = -1.441$	$U_{4443} = 8.688 \cdot 10^{1}$	$U_{4444} = -3.156 \cdot 10^{2}$
$U_{4632} = 8.751 \cdot 10^{-1}$	$U_{4641} = -2.575 \cdot 10^{-2}$	$U_{4663} = -2.248 \cdot 10^{-2}$
$U_{5222} = 4.993 \cdot 10^{-1}$	$U_{5331} = 1.546 \cdot 10^{-3}$	$U_{5332} = 2.469 \cdot 10^{-2}$
$U_{5431} = 1.873 \cdot 10^{-2}$	$U_{5432} = -4.126 \cdot 10^{-1}$	$U_{5441} = 9.242 \cdot 10^{-4}$
$U_{5442} = -2.145 \cdot 10^{1}$	$U_{5622} = 2.901 \cdot 10^{-1}$	$U_{5633} = -5.524 \cdot 10^{-3}$
$U_{5644} = -7.019 \cdot 10^{-1}$	$U_{5666} = 2.901 \cdot 10^{-1}$	

Entrance-to-Midplane Transport

For transport from the entrance to the vertical midplane, tables 3.6 and 3.7 list non-zero T and U matrix elements, respectively. The following are the centroid and R matrix elements (unlisted elements are zero):

$$C_5 = 2.321049732530 \tag{3.158}$$

$$R_{51} = -2.179660432 \tag{3.159}$$

$$R_{52} = -2.529550131 \tag{3.160}$$

$$R_{16} = -9.089085575 \cdot 10^{-1} \tag{3.161}$$

$$R_{56} = 1.160524866 \tag{3.162}$$

$$R_{66} = 1.000000000 \tag{3.163}$$

$$\begin{pmatrix} R_{11} & R_{12} \\ R_{21} & R_{22} \end{pmatrix} = \begin{pmatrix} 0.000000000 & 0.4169954844 \\ -2.398107503 & -2.783063390 \end{pmatrix} \tag{3.164}$$

$$\begin{pmatrix} R_{33} & R_{34} \\ R_{43} & R_{44} \end{pmatrix} = \begin{pmatrix} 0.07531765053 & 2.182639820 \\ -0.3979387890 & 1.745181272 \end{pmatrix} \tag{3.165}$$

Table 3.6: **Non-zero T Matrix Elements from Entrance to Vertical Midplane**

$T_{111} = 1.581820$	$T_{121} = 3.671483$	$T_{122} = 2.357651$
$T_{133} = 3.170513 \cdot 10^{-1}$	$T_{143} = -4.724714 \cdot 10^{-1}$	$T_{144} = -2.932169 \cdot 10^{-1}$
$T_{162} = 2.084977 \cdot 10^{-1}$	$T_{166} = 2.272271 \cdot 10^{-1}$	$T_{221} = 2.613530$
$T_{222} = 1.835742$	$T_{233} = -3.739056 \cdot 10^{-1}$	$T_{243} = 9.437959 \cdot 10^{-1}$
$T_{244} = 7.286366 \cdot 10^{-1}$	$T_{261} = 1.199054$	$T_{331} = 5.249703 \cdot 10^{-1}$
$T_{332} = 3.240582$	$T_{341} = -2.367091$	$T_{342} = -1.933840$
$T_{364} = 1.091320$	$T_{431} = -9.936083 \cdot 10^{-2}$	$T_{432} = 2.168953$
$T_{441} = -2.536989$	$T_{442} = -2.015590$	$T_{463} = 1.989694 \cdot 10^{-1}$
$T_{521} = 1.875460$	$T_{522} = 1.378390$	$T_{533} = -3.473390 \cdot 10^{-1}$
$T_{543} = 4.235456 \cdot 10^{-1}$	$T_{544} = 1.614540$	$T_{562} = -1.264775$
$T_{566} = -2.901312 \cdot 10^{-1}$		

Table 3.7: **Non-zero U Matrix Elements from Entrance to Vertical Midplane**

$U_{1211} = -3.085$	$U_{1221} = -5.581$	$U_{1222} = -2.478$
$U_{1331} = 4.933 \cdot 10^{-1}$	$U_{1332} = 3.610 \cdot 10^{-2}$	$U_{1431} = -1.791$
$U_{1432} = -2.841$	$U_{1441} = -5.547 \cdot 10^{-1}$	$U_{1442} = -1.004$
$U_{1611} = -7.909 \cdot 10^{-1}$	$U_{1622} = 1.179$	$U_{1633} = -1.585 \cdot 10^{-1}$
$U_{1644} = -1.466 \cdot 10^{-1}$	$U_{1662} = -5.213 \cdot 10^{-2}$	$U_{1666} = -1.136 \cdot 10^{-1}$
$U_{2111} = -6.200$	$U_{2211} = -2.159 \cdot 10^{1}$	$U_{2221} = -2.700 \cdot 10^{1}$
$U_{2222} = -9.493$	$U_{2331} = 2.284 \cdot 10^{-1}$	$U_{2332} = 1.145$
$U_{2421} = -1.025 \cdot 10^{-8}$	$U_{2431} = 1.686$	$U_{2432} = 1.572$
$U_{2441} = -4.851$	$U_{2442} = -4.688$	$U_{2621} = -1.307$
$U_{2633} = 3.739 \cdot 10^{-1}$	$U_{2643} = -4.719 \cdot 10^{-1}$	$U_{2661} = -8.993 \cdot 10^{-1}$
$U_{3311} = 6.554 \cdot 10^{-2}$	$U_{3321} = -3.313$	$U_{3322} = -4.769$
$U_{3333} = 3.965 \cdot 10^{-1}$	$U_{3411} = 1.448$	$U_{3421} = 1.908$
$U_{3422} = 3.934 \cdot 10^{-1}$	$U_{3433} = -1.195$	$U_{3443} = -8.190 \cdot 10^{-1}$
$U_{3444} = 1.457$	$U_{3631} = -2.625 \cdot 10^{-1}$	$U_{3642} = -9.669 \cdot 10^{-1}$
$U_{3664} = -2.728 \cdot 10^{-1}$	$U_{4311} = -3.463 \cdot 10^{-1}$	$U_{4321} = -4.190$
$U_{4322} = -4.777$	$U_{4333} = 2.704 \cdot 10^{-1}$	$U_{4411} = 1.604$
$U_{4421} = 2.868$	$U_{4422} = 1.015$	$U_{4433} = -9.890 \cdot 10^{-1}$
$U_{4443} = 1.350 \cdot 10^{-1}$	$U_{4444} = 5.265 \cdot 10^{-1}$	$U_{4631} = 9.936 \cdot 10^{-2}$
$U_{4632} = -1.084$	$U_{4641} = 1.268$	$U_{4663} = -1.492 \cdot 10^{-1}$
$U_{5111} = -1.264$	$U_{5211} = -4.402$	$U_{5221} = -7.153$
$U_{5222} = -2.112$	$U_{5331} = -1.045 \cdot 10^{-1}$	$U_{5332} = 1.548 \cdot 10^{-1}$
$U_{5431} = 1.514$	$U_{5432} = 3.542$	$U_{5441} = -2.804$
$U_{5442} = -1.689$	$U_{5622} = 6.892 \cdot 10^{-1}$	$U_{5633} = 1.737 \cdot 10^{-1}$
$U_{5644} = 8.073 \cdot 10^{-1}$	$U_{5662} = 3.162 \cdot 10^{-1}$	$U_{5666} = 1.451 \cdot 10^{-1}$

Midplane to Exit Transport

For transport from the vertical midplane to the exit, tables 3.8 and 3.9 list non-zero T and U matrix elements, respectively. The following are the centroid and R matrix elements (unlisted elements are zero):

$$C_5 = 2.321049732530 \tag{3.166}$$

$$R_{16} = -2.529550131 \tag{3.167}$$

$$R_{26} = -2.179660432 \tag{3.168}$$

$$R_{52} = -0.9089085575 \tag{3.169}$$

$$R_{56} = 1.160524866 \tag{3.170}$$

$$R_{66} = 1.000000000 \tag{3.171}$$

$$\begin{pmatrix} R_{11} & R_{12} \\ R_{21} & R_{22} \end{pmatrix} = \begin{pmatrix} -2.783063390 & 0.4169954844 \\ -2.398107503 & 0.0000000000 \end{pmatrix} \tag{3.172}$$

$$\begin{pmatrix} R_{33} & R_{34} \\ R_{43} & R_{44} \end{pmatrix} = \begin{pmatrix} 1.745181272 & 2.182639820 \\ -0.3979387890 & 0.07531765053 \end{pmatrix} \tag{3.173}$$

Table 3.8: **Non-zero T Matrix Elements from Vertical Midplane to Exit**

$T_{111} = 7.654960 \cdot 10^{-1}$	$T_{121} = 1.089830$	$T_{122} = 7.654960 \cdot 10^{-1}$
$T_{133} = 1.491568$	$T_{143} = 4.885853$	$T_{144} = 3.609338$
$T_{161} = 1.391532$	$T_{162} = 1.199054$	$T_{166} = 1.264775$
$T_{211} = 3.133763$	$T_{222} = 6.596119 \cdot 10^{-1}$	$T_{233} = 1.417467$
$T_{243} = 4.999269$	$T_{244} = 3.804388$	$T_{261} = 6.895662$
$T_{266} = 4.223593$	$T_{331} = 2.227000$	$T_{332} = -1.057913$
$T_{341} = 1.950208$	$T_{342} = -9.870661 \cdot 10^{-1}$	$T_{363} = 2.024140$
$T_{364} = 2.863881$	$T_{431} = 5.477911$	$T_{432} = -4.143302 \cdot 10^{-2}$
$T_{441} = 6.310239$	$T_{442} = 2.189102 \cdot 10^{-1}$	$T_{463} = 5.177889$
$T_{464} = 5.735430$	$T_{511} = 1.668521$	$T_{521} = -5.000000 \cdot 10^{-1}$
$T_{533} = -1.736188 \cdot 10^{-1}$	$T_{543} = -4.342785 \cdot 10^{-1}$	$T_{544} = 4.109782 \cdot 10^{-2}$
$T_{561} = 3.033067$	$T_{562} = -9.089086 \cdot 10^{-1}$	$T_{566} = 1.088259$

Table 3.9: **Non-zero U Matrix Elements from Vertical Midplane to Exit**

$U_{1111} = -1.360$	$U_{1211} = -5.249 \cdot 10^{-1}$	$U_{1222} = -4.872 \cdot 10^{-1}$
$U_{1331} = 2.309$	$U_{1332} = -3.196$	$U_{1431} = 4.658$
$U_{1432} = -7.406$	$U_{1441} = 2.017$	$U_{1442} = -4.261$
$U_{1611} = -4.089$	$U_{1621} = -9.537 \cdot 10^{-1}$	$U_{1622} = 3.828 \cdot 10^{-1}$
$U_{1631} = 5.964 \cdot 10^{-4}$	$U_{1633} = 1.353$	$U_{1641} = 6.949 \cdot 10^{-4}$
$U_{1643} = 4.234$	$U_{1644} = 3.638$	$U_{1661} = -4.413$
$U_{1662} = -7.334 \cdot 10^{-1}$	$U_{1666} = -1.969$	$U_{2111} = -1.336 \cdot 10^{1}$
$U_{2221} = -1.361$	$U_{2331} = 2.331$	$U_{2332} = -2.750$
$U_{2431} = 1.181$	$U_{2432} = -5.745$	$U_{2441} = -2.352$
$U_{2442} = -2.750$	$U_{2611} = -3.957 \cdot 10^{1}$	$U_{2621} = -3.419 \cdot 10^{-3}$
$U_{2622} = -1.237$	$U_{2631} = -3.495 \cdot 10^{-3}$	$U_{2633} = 7.009 \cdot 10^{-1}$
$U_{2641} = -4.345 \cdot 10^{-3}$	$U_{2643} = -1.426$	$U_{2644} = -2.138$
$U_{2661} = -4.114 \cdot 10^{1}$	$U_{2666} = -1.528 \cdot 10^{1}$	$U_{3311} = 3.497$
$U_{3321} = -3.620$	$U_{3322} = -3.336 \cdot 10^{-1}$	$U_{3333} = -1.167$
$U_{3411} = 4.993$	$U_{3421} = -4.032$	$U_{3422} = -2.847 \cdot 10^{-1}$
$U_{3431} = 5.003 \cdot 10^{-4}$	$U_{3433} = -4.874$	$U_{3443} = -6.236$
$U_{3444} = -2.195$	$U_{3631} = 5.245$	$U_{3632} = -3.290$
$U_{3641} = 9.078$	$U_{3642} = -4.158$	$U_{3663} = 1.371$
$U_{3664} = 3.409$	$U_{4311} = -9.066$	$U_{4321} = -3.494$
$U_{4322} = -1.567$	$U_{4333} = -2.991$	$U_{4411} = -1.456 \cdot 10^{1}$
$U_{4421} = -2.893$	$U_{4422} = -1.724$	$U_{4431} = -5.345 \cdot 10^{-4}$
$U_{4433} = -1.323 \cdot 10^{1}$	$U_{4443} = -1.849 \cdot 10^{1}$	$U_{4444} = -8.388$
$U_{4631} = -2.196 \cdot 10^{1}$	$U_{4632} = -3.155$	$U_{4641} = -2.962 \cdot 10^{1}$
$U_{4642} = -2.630$	$U_{4643} = -5.769 \cdot 10^{-4}$	$U_{4663} = -1.386 \cdot 10^{1}$
$U_{4664} = -1.633 \cdot 10^{1}$	$U_{5111} = -9.178 \cdot 10^{-1}$	$U_{5211} = -1.307$
$U_{5221} = -9.179 \cdot 10^{-1}$	$U_{5222} = 4.545 \cdot 10^{-1}$	$U_{5331} = -2.232$
$U_{5332} = 2.105 \cdot 10^{-1}$	$U_{5431} = -6.162$	$U_{5432} = 1.565 \cdot 10^{-1}$
$U_{5441} = -4.254$	$U_{5442} = 4.173 \cdot 10^{-1}$	$U_{5611} = -3.337$
$U_{5621} = -2.375$	$U_{5622} = -8.343 \cdot 10^{-1}$	$U_{5633} = -1.941$
$U_{5643} = -5.601$	$U_{5644} = -3.846$	$U_{5661} = -4.550$
$U_{5662} = -8.523 \cdot 10^{-1}$	$U_{5666} = -1.923$	

3.6 Effects of Field Errors

All of the above analysis of the alpha-magnet assumes that the functional form of the magnetic field is that of a perfect quadrupole. In reality, no magnet is ideal. A review of the derivation of the scaled equation of motion shows that non-linear terms in the magnetic field will, strictly speaking, invalidate the scaling. In other words, the magnet will not be strictly achromatic, as a perfect alpha-magnet would be. One result of this is that the nominal ideal trajectory (i.e., the trajectory injected at incidence angle θ_α) will no longer exit the magnet at the same location that it entered at.

Magnetic field errors are a fact of life in accelerator physics. The favored approach to dealing with them is to evaluate the effect of specific types of errors (e.g., higher-order multipoles) with an eye toward what level of error one's application can tolerate. In accordance with this, I have studied the effect of certain types of field errors, such as sextupole terms, to find what effect they have on the performance of the alpha-magnet. (Similar, less complete work on this problem is reported in [32].) It has been found from computer studies that for a variety of errors, the residual dispersion after the alpha magnet can be reduced to acceptable levels by modifying the injection angle, θ_i, in such a way as to cause the ideal trajectory to once again exit at the entrance point. If the magnet retains reflection symmetry about the plane $q_2 = 0$, it is always possible to find such a value of θ_i, which I will call θ_m, or the "mirror angle". The reader can convince himself of this by reviewing the argument by which I proved that the perfect alpha-magnet has such an injection angle, namely θ_α.

The field in the imperfect alpha-magnet can be expressed as

$$\begin{aligned}\mathbf{B}(\mathbf{q}) &= \mathrm{g}(q_3, 0, q_1) + \Delta\mathbf{B}(\mathbf{q}) \\ &= \frac{\mathrm{g}}{\alpha}\left\{(Q_3, 0, Q_1) + \Delta\mathbf{B}(\frac{\mathbf{Q}}{\alpha})\frac{\alpha}{\mathrm{g}}\right\},\end{aligned} \tag{3.174}$$

where $\Delta\mathbf{B}(\mathbf{q})$ is the departure of the field from a true, uniform quadrupole field and, as before, $\mathbf{Q} \equiv \mathbf{q}\alpha$.

Comparison with equation (3.83) shows that the scaled equation of motion with field errors is

$$\mathbf{Q}'' = -\frac{1}{1+\delta}\mathbf{Q}' \times \mathbf{B}(\frac{\mathbf{Q}}{\alpha})\frac{\alpha}{g} \tag{3.175}$$

$$= -\frac{1}{1+\delta}\mathbf{Q}' \times \left\{(Q_3, 0, Q_1) + \Delta\mathbf{B}(\frac{\mathbf{Q}}{\alpha})\frac{\alpha}{g}\right\} \tag{3.176}$$

3.6.1 Multipole Errors

With this equation in hand, it is possible to evaluate the effect of various field errors. Note that since α appears only as a multiplicative factor for the field error, it is still possible to find results with some universality. In particular, if $\Delta\mathbf{B}$ is a pure multipole error, then the effect of the field error in the equation of motion will have a well-defined scaling with α and the multipole coefficient.

Multipole fields can be classified as upright or rotated[6], depending on whether the magnetic fields are changed in sign upon reflection of the magnet through the $q_3 = 0$ plane or not, respectively. Upright multipoles have field lines that cross the $q_3 = 0$ plane with normal incidence. For rotated multipoles, field lines do not cross the $q_3 = 0$ plane. Clearly the alpha-magnet has upright symmetry, and if one confines oneself to errors that do not alter this symmetry, then one can express errors in the alpha-magnet in terms of the upright multipoles. For example, any deviation of the poles from a hyperbola will produce only upright multipole errors, as will displacement of the mirror plane, since neither of these errors changes the fact that the field lines cross $q_3 = 0$ with normal incidence.

The field due to a pure upright multipole is[6]:

$$\Delta\mathbf{B}_n = A_n \sum_{m=1}^{\lfloor n/2 \rfloor} (-1)^{m-1} \frac{q_1^{n-2m}}{(n-2m)!} \frac{q_3^{2m-1}}{(2m-1)!}\hat{q}_1 + A_n \sum_{m=1}^{\lfloor (n+1)/2 \rfloor} (-1)^{m-1} \frac{q_1^{n-2m+1}}{(n-2m+1)!} \frac{q_3^{2m-2}}{(2m-2)!}\hat{q}_3, \tag{3.177}$$

where $n \geq 1$ is an integer, the "order" of the multipole. $n = 1$ is a dipole, $n = 2$ a quadrupole, and so forth.

For insertion into equation (3.176), this must be rewritten in terms of scaled coordinates, as

$$\frac{\alpha}{g}\Delta\mathbf{B}_n = M_n\sum_{m=1}^{\lfloor n/2\rfloor}(-1)^{m-1}\frac{Q_1^{n-2m}}{(n-2m)!}\frac{Q_3^{2m-1}}{(2m-1)!}\hat{\mathbf{Q}}_1 + M_n\sum_{m=1}^{\lfloor (n+1)/2\rfloor}(-1)^{m-1}\frac{Q_1^{n-2m+1}}{(n-2m+1)!}\frac{Q_3^{2m-2}}{(2m-2)!}\hat{\mathbf{Q}}_3, \tag{3.178}$$

where I have defined the dimensionless normalized multipole strength

$$M_n \equiv \frac{A_n}{g\alpha^{n-2}}. \tag{3.179}$$

Even without integration one can conclude that for the same fractional multipole error, $\frac{A_n}{g}$, the perturbation is stronger for smaller α, i.e., for alpha-magnets operated so as to obtain larger values of $\hat{q}_1$. This is as expected, since the multipole field grows as q_1^n. As expected, in the limit of very large α, i.e., very small $\hat{q}_1$, multipole errors have no effect.

It is of course possible to compute the matrices for equation (3.176) with $\Delta\mathbf{B}$ as given by (3.179) as was done for the equation of motion without field errors. The matrices thus obtained are to be considered functions of M_n, with M_n ultimately a function of α. Hence, if the matrices are found for some particular value of M_n for some particular n, then if the matrices are scaled to some particular value of α according to equation (3.93), the result is appropriate to a multipole strength of

$$A_n = M_n g\alpha^{n-2}. \tag{3.180}$$

I have written a computer program, **serrors**, which computes third-order scaled alpha-magnet matrices in the presence of various types of field errors, including multipole errors. Figures 3.10 through 3.12 show the effect of sextupole errors on the mirror-angle (θ_m), $\hat{Q}_1$, and the non-zero elements of the matrix R. Note the particularly strong effect in the vertical plane.

3.6.2 Entrance-Hole-Induced Errors

I performed magnetic measurements on the SSRL alpha-magnet to assess the deviation of the field from an ideal quadrupolar field. Figure 3.13 shows the measured

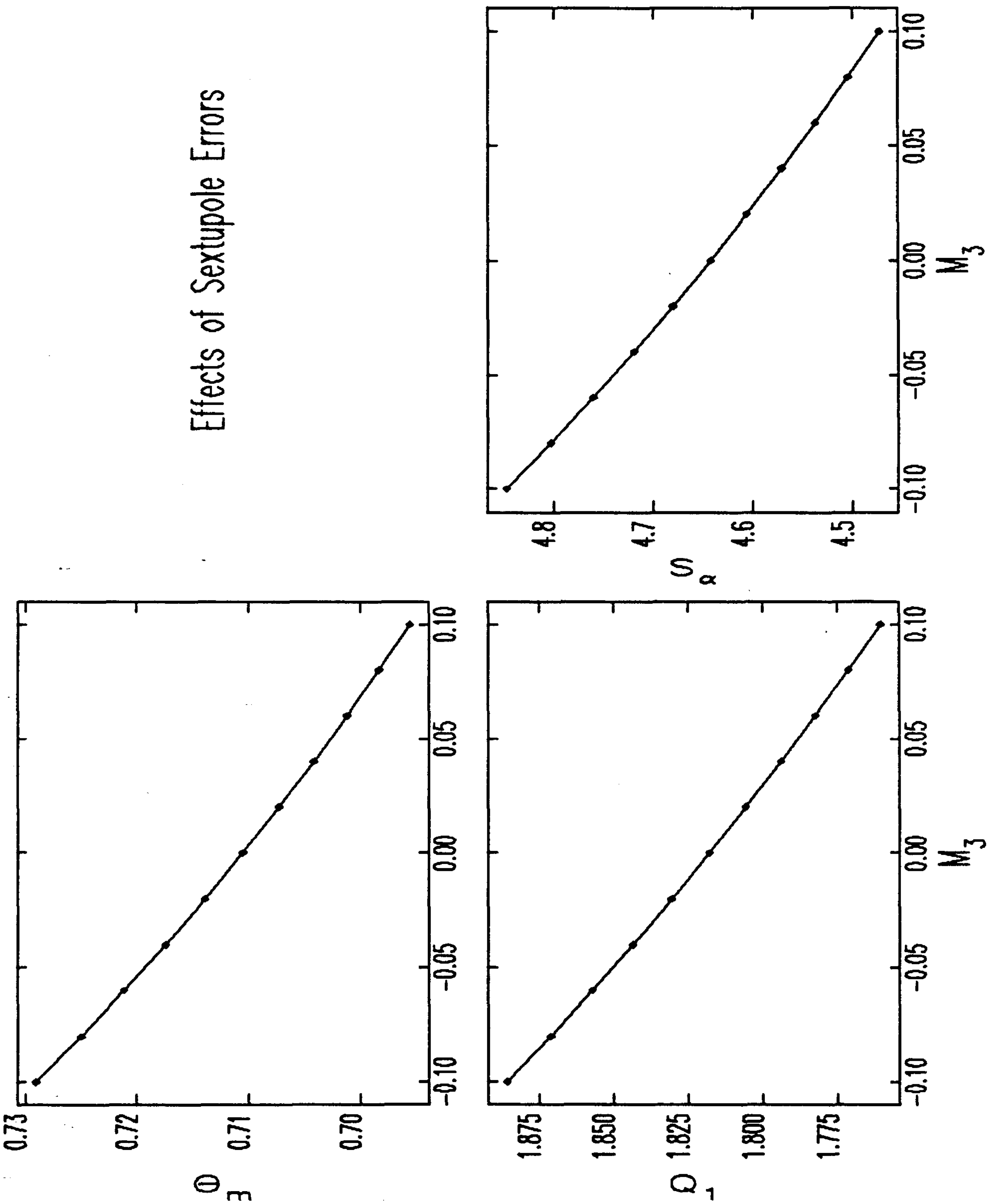

Figure 3.10: Effects of Sextupole Errors—Part 1

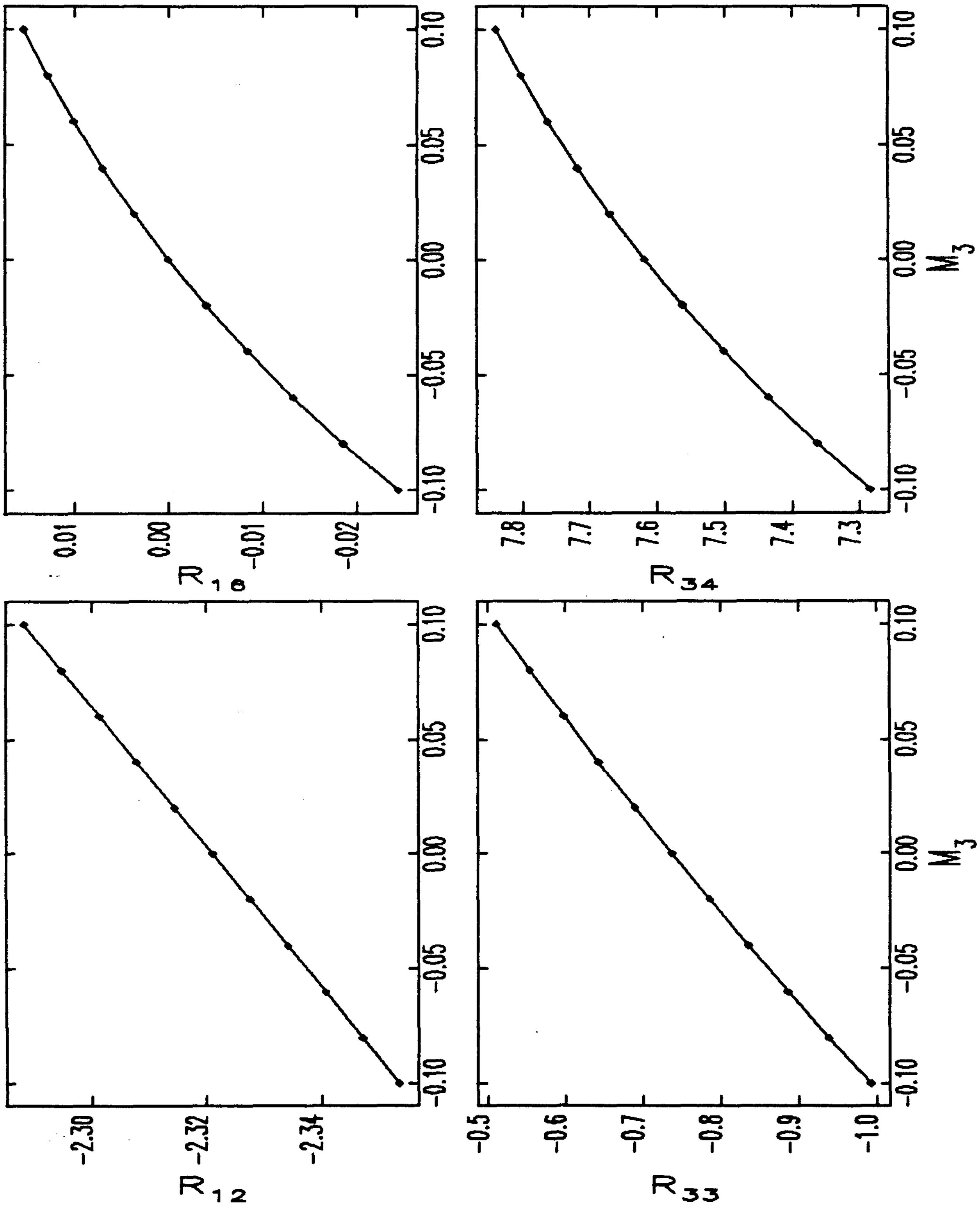

Figure 3.11: Effects of Sextupole Errors—Part 2

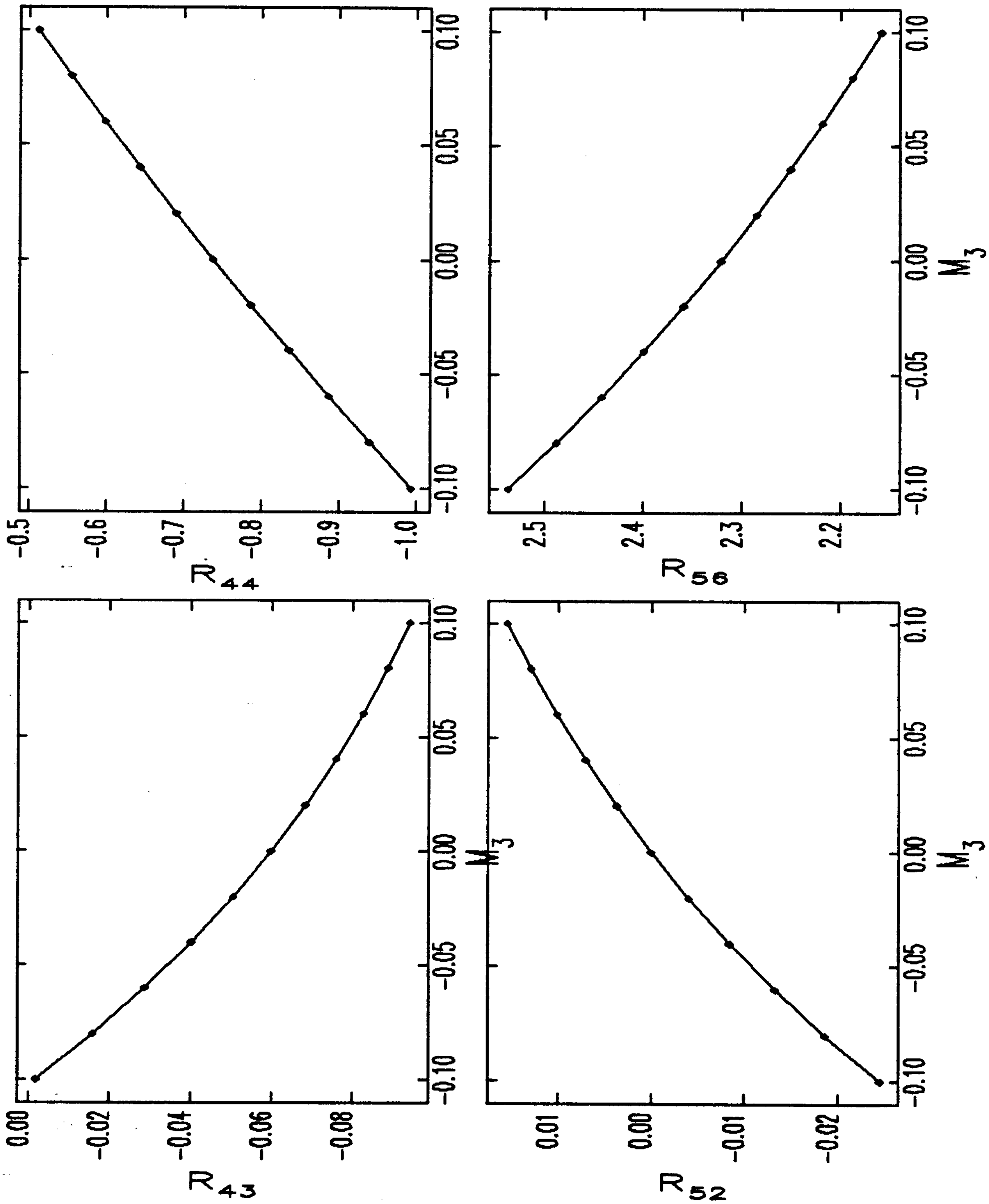

Figure 3.12: Effects of Sextupole Errors—Part 3

gradient vs q_1 for $q_2 = 0$, while figure 3.14 shows the measured gradient vs q_2 for $q_1 \approx 10$mm. The deviation of the field from a perfect quadrupole was dominated by perturbations from the beam aperture or "hole" cut in the magnetic mirror-plate of the alpha magnet. This can be appreciated by comparing Figure 3.13 with Figure 3.2, which shows the gradient before the hole was cut. This hole is, of course, necessary in order to get the beam into and out of the magnet. I have found that the field error in the $q_3 = 0$ plane is well approximated by

$$\Delta B_3 = g(K + Ee^{-q_1/d})F(q_2), \tag{3.181}$$

where K and E are positive constants, d is a decay constant for the field error, and F is the function

$$F(q_2) = \begin{cases} 1 & |q_2| < W_1 \\ \frac{W_2 - |q_2|}{W_2 - W_1} & W_1 \le |q_2| < W_2. \\ 0 & W_2 \le |q_2| \end{cases} \tag{3.182}$$

W_1 and W_2 are constants characterizing the width of the field perturbation in q_2. W_1 is roughly equal to the width of the hole in the midplane.

Fits to the data in the Figures give

$$\begin{array}{lll} K = 0.054\text{cm} & E = 0.39\text{cm} & d = 0.72\text{cm} \\ W_1 = 2.0\text{cm} & & W_2 = 3.6\text{cm}. \end{array} \tag{3.183}$$

Using Maxwell's curl equation, one can find an approximation to the full error field:

$$\frac{\alpha}{g}\Delta\mathbf{B} = E\alpha\left\{-\hat{q}_1\frac{Q_3}{\alpha d}e^{-\frac{Q_1}{\alpha d}}F(\frac{Q_2}{\alpha}) + -\hat{q}_2\frac{Q_3}{\alpha d}e^{-\frac{Q_1}{\alpha d}}F'(\frac{Q_2}{\alpha}) + \hat{q}_3(1 + \frac{K\alpha}{E\alpha})e^{-\frac{Q_1}{\alpha d}}F(\frac{Q_2}{\alpha})\right\} \tag{3.184}$$

(The possibility of dipole fields in the $\mathbf{q}_2$ and $\mathbf{q}_1$ directions can be eliminated by symmetry and by assuming that there are no rotated multipole fields present, respectively.) The constants K, E, and d occur in equation (3.184) only when multiplied by α. Similarly, the constants W_1 and W_2 occur only in the combinations $W_1\alpha$ and $W_2\alpha$, as seen from the definition of F. Any given magnet has fixed values for K, E, d, W_1, and W_2, while α will vary was the gradient of the magnet and the beam momentum are varied.

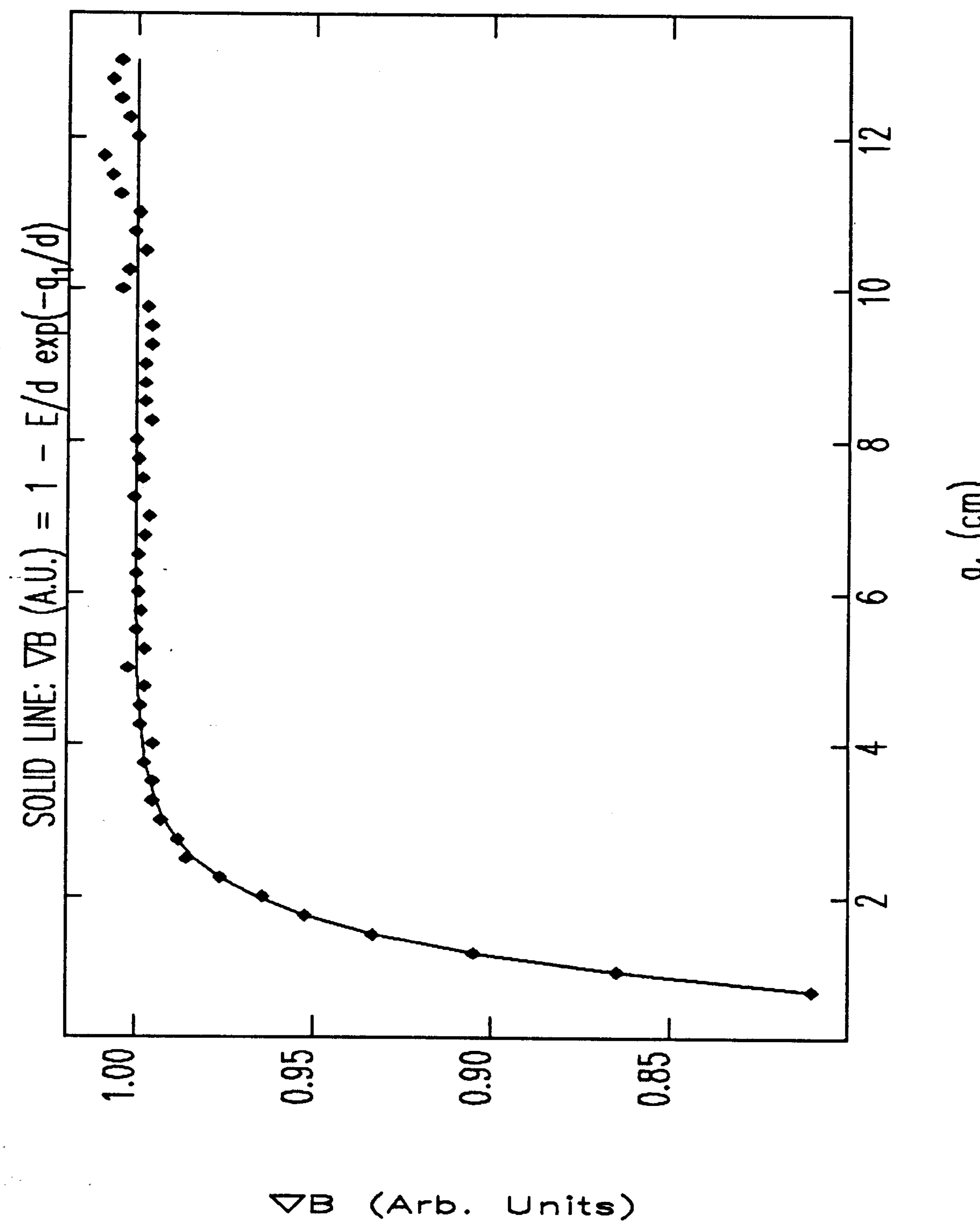

Figure 3.13: Hole-Induced Gradient Errors vs q_1

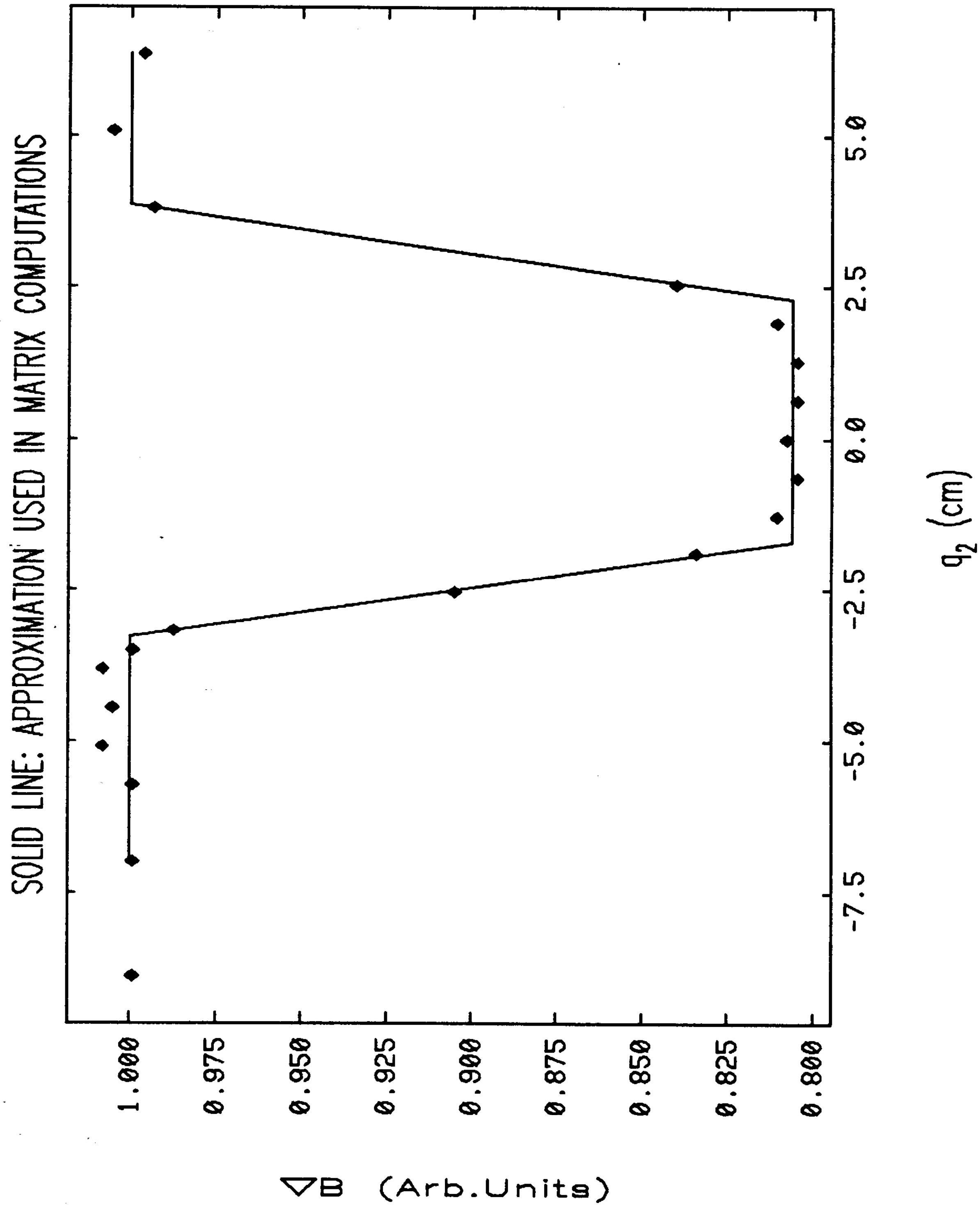

Figure 3.14: Hole-Induced Gradient Errors vs q_2

To show how it is possible to find matrices for the hole-induced error in a given alpha-magnet as a function of α it is convenient to define dimensionless error field parameters

$$\begin{array}{ccc} \tilde{K} \equiv \alpha K & \tilde{E} \equiv \alpha E & \tilde{d} \equiv \alpha d \\ \tilde{W}_1 \equiv \alpha W_1 & & \tilde{W}_2 \equiv \alpha W_2, \end{array} \tag{3.185}$$

and a function corresponding to F

$$\tilde{F}(Q_2) = \begin{cases} 1 & |Q_2| < \tilde{W}_1 \\ \frac{\tilde{W}_2 - |Q_2|}{\tilde{W}_2 - \tilde{W}_1} & \tilde{W}_1 \leq |Q_2| < \tilde{W}_2. \\ 0 & \tilde{W}_2 \leq |Q_2| \end{cases} \tag{3.186}$$

The hole-induced error field (equation (3.184)) is expressible as

$$\frac{\alpha}{g}\Delta\mathbf{B} = \tilde{E}\left\{-\hat{\mathbf{Q}}_1\frac{Q_3}{\tilde{d}}e^{-\frac{Q_1}{\tilde{d}}}\tilde{F}(Q_2) + -\hat{\mathbf{Q}}_2\frac{Q_3}{\tilde{d}}e^{-\frac{Q_1}{\tilde{d}}}\tilde{F}'(Q_2) + \hat{\mathbf{Q}}_3(1+\frac{\tilde{K}}{\tilde{E}})e^{-\frac{Q_1}{\tilde{d}}}\tilde{F}(Q_2)\right\}, \tag{3.187}$$

which is formally independent of α, as desired for insertion into equation (3.176).

serrors takes E, K, d, W_1, and W_2 as input, and computes the matrices as a function of a variable M, where $\tilde{E} = M * E$, $\tilde{K} = M * K$, etc. Clearly, by choosing the scaled matrices for $M = \alpha$ and scaling them according to equation (3.93) with $\alpha_o = \alpha$, one obtains the matrices for the magnet with errors for a given value of α.

While one chooses the value of M is equal the α value of interest, the reader should not make the mistake of concluding that **serrors** is varying α, or calculating matrices at a given value of α. **serrors** is scaling the spatial extent and magnitude of the error field in *scaled* coordinates, and calculating the matrices for the scaled equation of motion in the presence of these error fields. By choosing $M = \alpha$, one obtains matrices that correspond to a certain trajectory size relative to the fixed spatial extent of the error fields. Another way to use these **serrors** results is to view M as a quantity related to the size of the beam-hole, in which case $M \neq \alpha$.

Figures 3.15 through 3.17 show the effects of hole-induced errors on $\hat{Q}_1$, S_α, θ_m, and strongly-affected R-matrix elements, as calculated by **serrors**. Typical values of α for the SSRL magnet and RF gun are between 0.12cm and 0.18cm. Note the large effect on the vertical plane, similar to that seen for sextupole errors. Experiments show that the vertical plane R matrix deviates significantly from that for an ideal magnet, a subject to which I will return in the next section. Running experience shows that injection angle corrections of 10-20 mrad are needed, with the sign such as to make θ smaller. It is unclear, however, what part of this is due to field errors and what part is required by alignment errors. The real value of these calculations is to evaluate the magnitude of the effects of such errors, to see whether the injection angle correction required for realistic error levels is feasible or not.

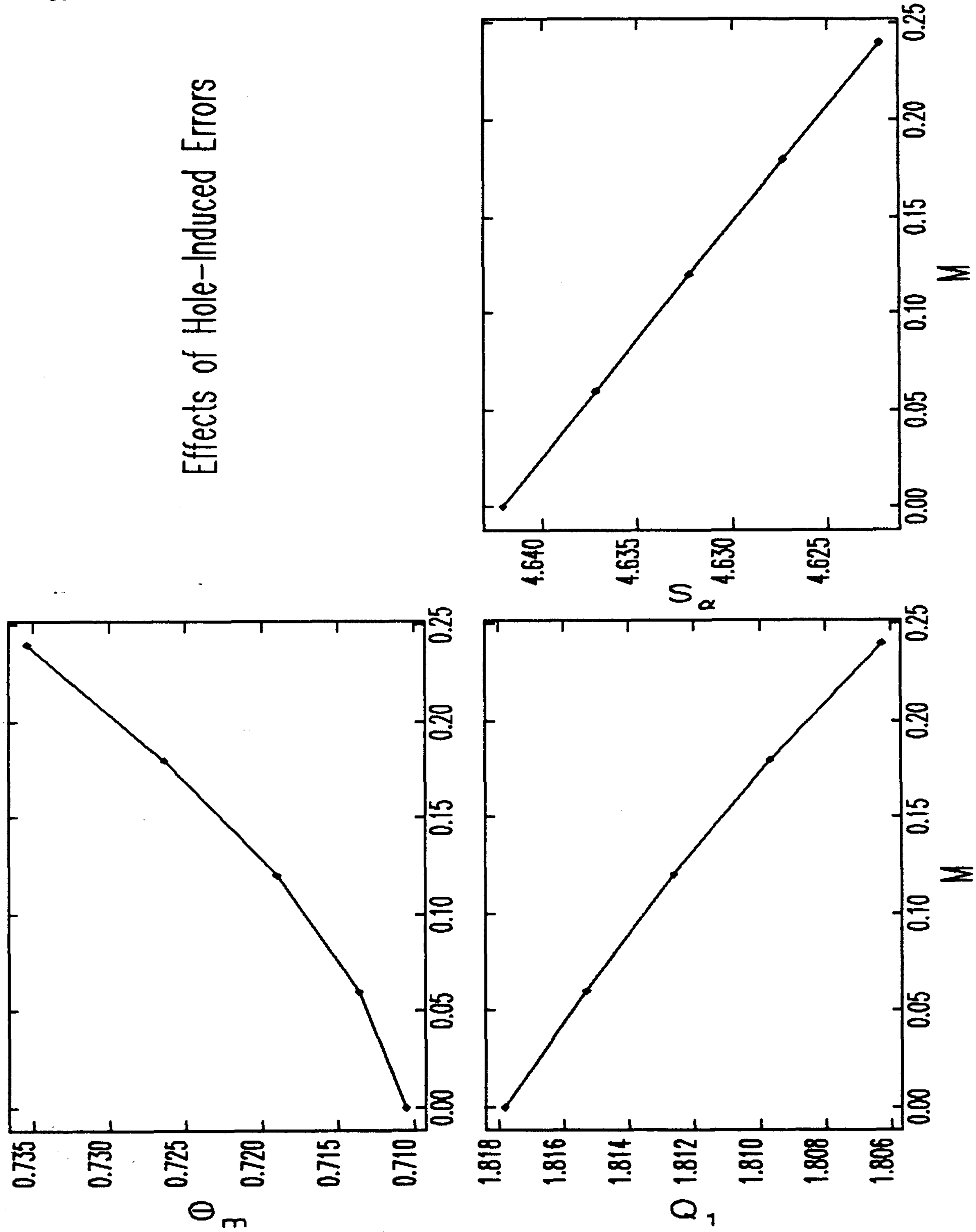

Figure 3.15: Effects of Hole-Induced Gradient Errors—Part 1

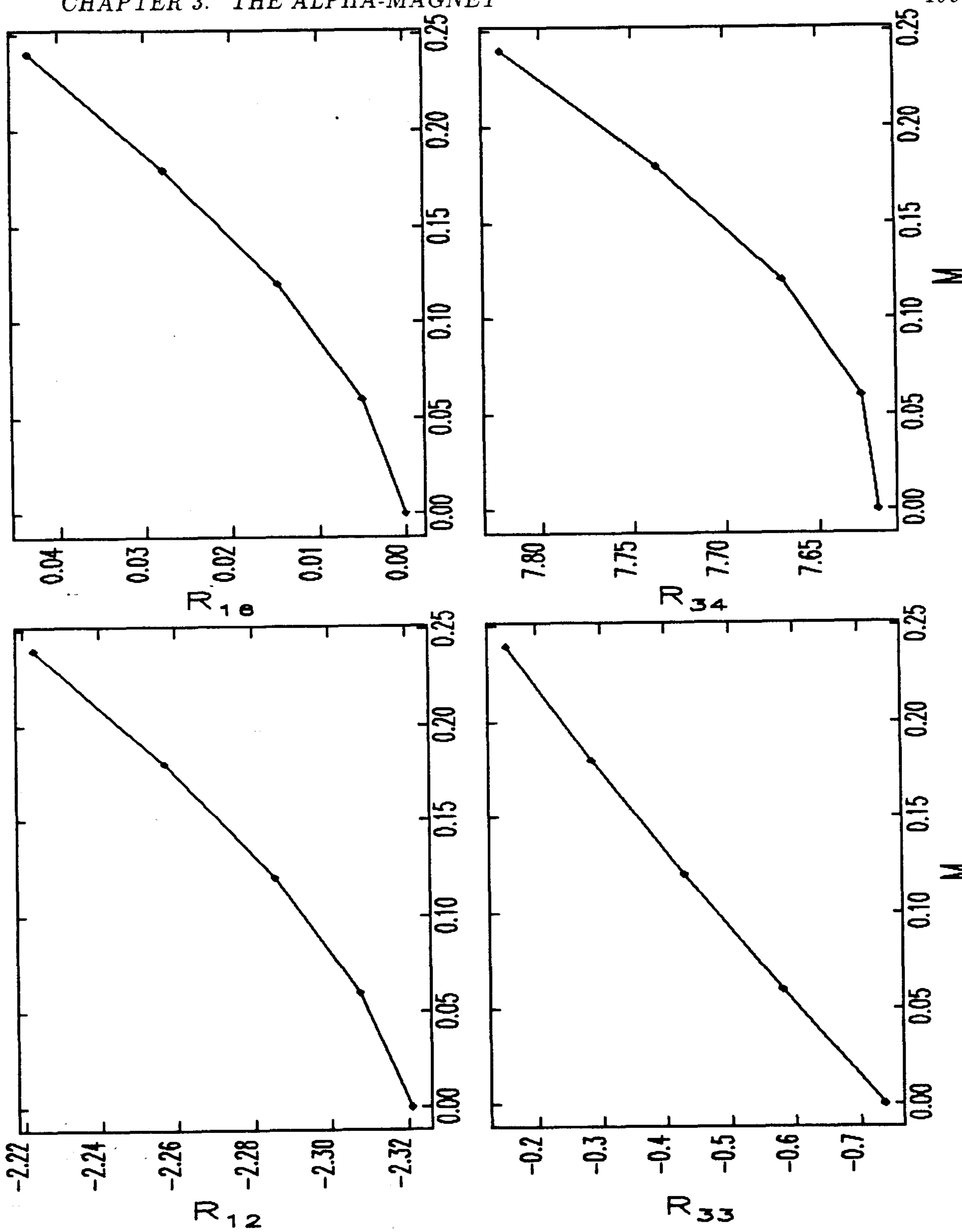

Figure 3.16: Effects of Hole-Induced Gradient Errors—Part 2

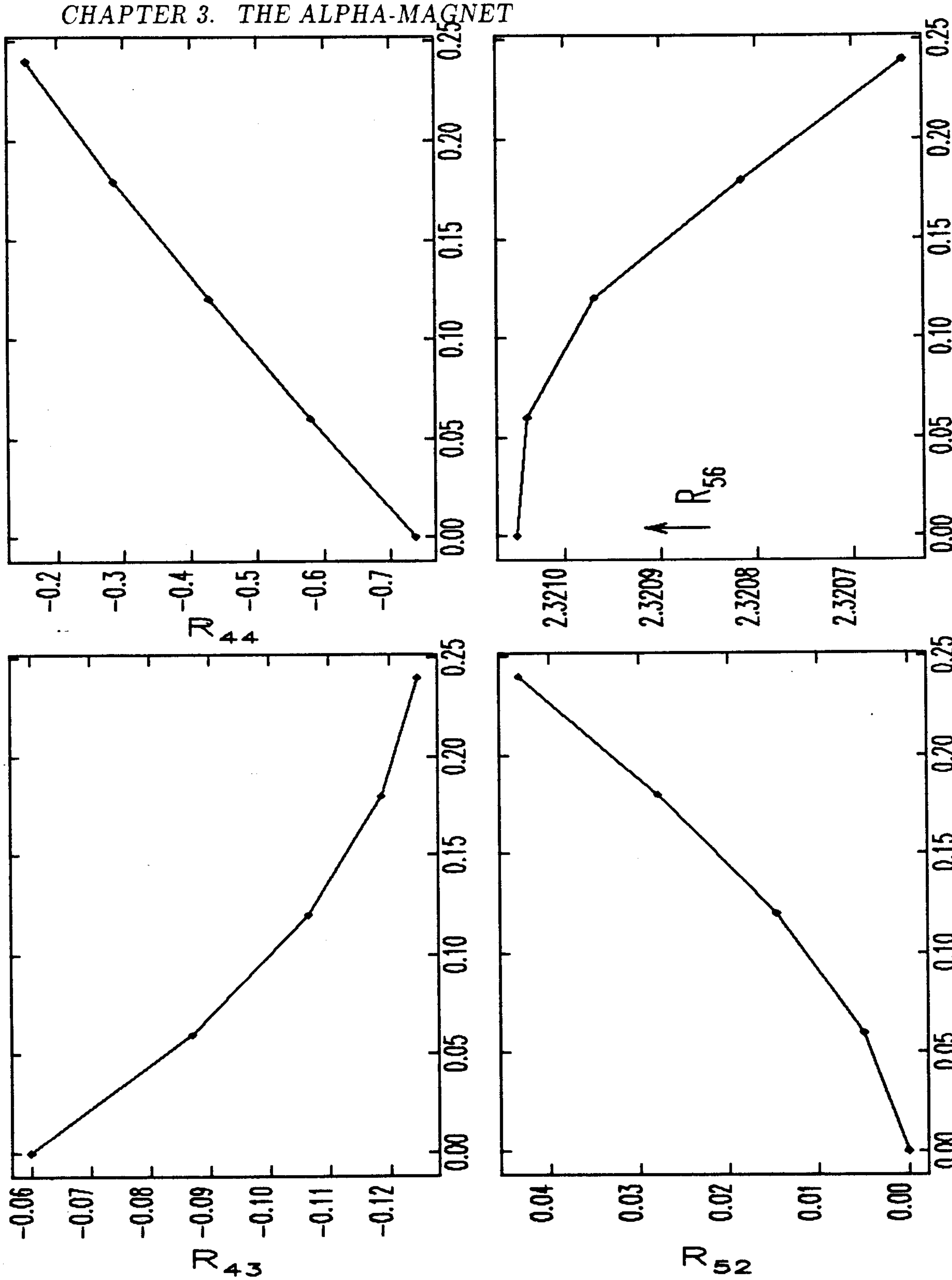

Figure 3.17: Effects of Hole-Induced Gradient Errors—Part 3

3.7 Alpha-Magnet Beam-Optics Experiments

A commonly-made measurement on beam-transport systems is that of determining the transverse centroid offset of the beam downstream from a steering magnet as a function of the angular kick imparted by that steering magnet. The linear term of a fit to the offset vs kick angle gives the r_{12} (or r_{34} for a vertically steering magnet) matrix element for transport from the steering magnet to the place where the centroid position is measured.

The Gun-to-Linac transport line (see Chapter 5) has horizontal and vertical steering just before the alpha-magnet, and a phosphorescent screen downstream of the alpha-magnet (the "chopper-screen", since it is part of the chopper tank). There is also a phosphorescent screen inside the alpha-magnet (the "alpha-magnet screen") that intercepts the beam when the alpha-magnet is turned off. These phosphorescent screens are viewed via closed-circuit TV. In addition, a Lecroy 9450 digital oscilloscope is available to digitize the TV scan, permitting accurate measurement of both horizontal and vertical beam positions. All that is required is to calibrate the TV sweep using features on the screens for which the positions are known (e.g., the edges of the screen).

I will let L_1 denote the distance from the center of this steering magnet, known as GTL_CORR2, to the "crossing-point" of the alpha-magnet ($q_1 = q_2 = q_3 = 0$). Also, L_2 and L_3 denote, respectively the distance from the crossing-point to the alpha-magnet screen, and from the crossing-point to the screen after the alpha-magnet. L_1 is found to be 117 mm, and L_3 to be 459 mm, where I use values from updated engineering drawings, checked by my own measurements with a ruler. The distance from the crossing-point to the screen in the alpha-magnet 200 $\pm$ 10mm, with the large uncertainty being due to the way the screen is held inside the alpha-magnet on long, easily-bent copper tubes.

3.7.1 Characterization of the Steering Magnet

I performed magnetic measurements on GTL_CORR2 with a quadrupole and an alpha-magnet-simulating iron plate in the proper positions relative to GTL_CORR2. The magnetic field as a function of longitudinal position z is shown in figure 3.18,

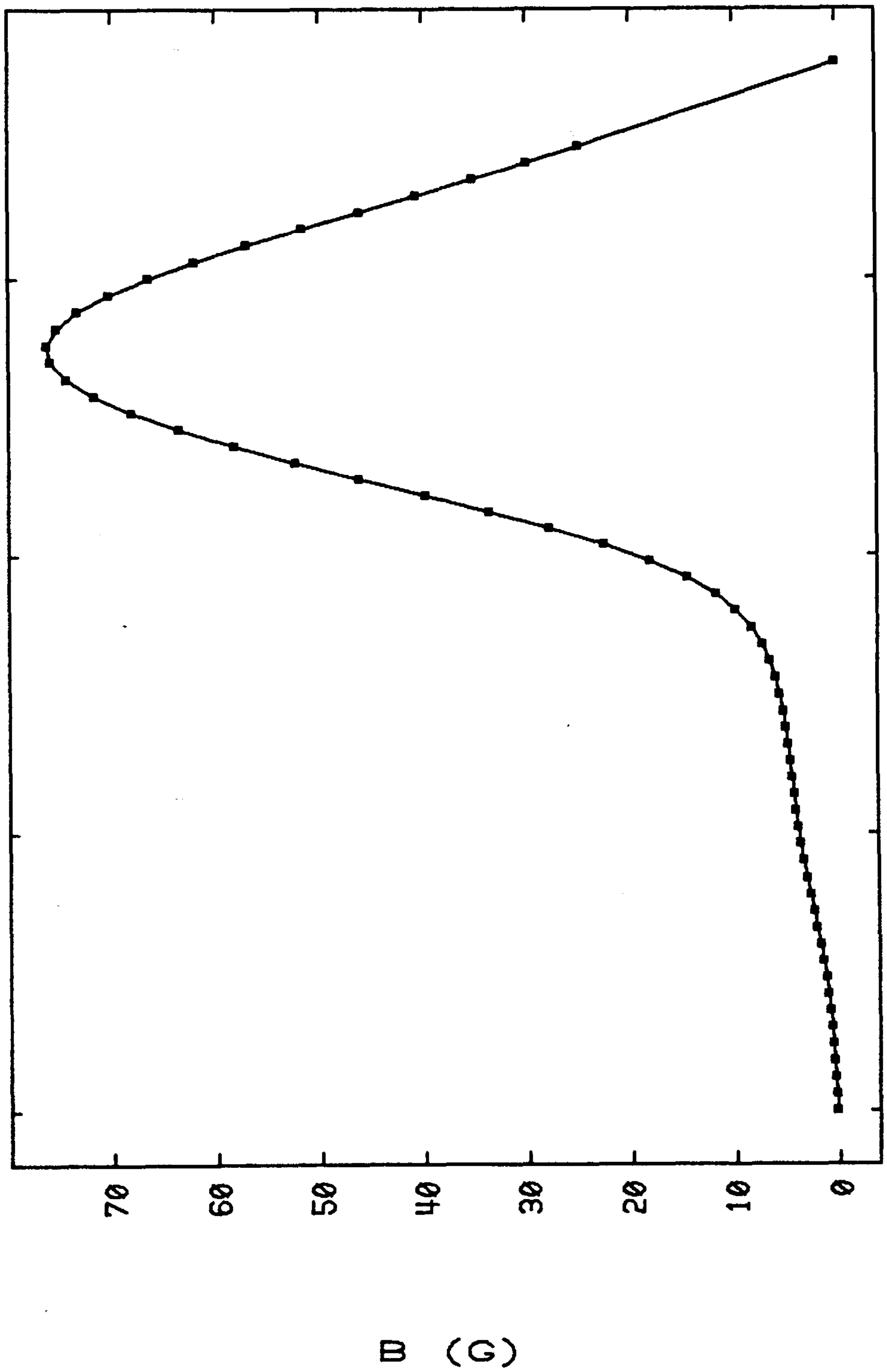

Figure 3.18: Magnetic Measurements for GTL_CORR2

and indicates that the equivalent angular kick for a zero-length steering magnet is 18mm ahead of the geometric center of the magnet (which coincides with the peak of the magnetic field vs z). Hence, GTL_CORR2 can be simulated by a zero-length steering magnet that is L_1 + 18mm from the alpha-magnet crossing point. I will thus let $L_1 \rightarrow L_1$ + 18mm, and treat GTL_CORR2 as a zero-length deflector.

Because GTL_CORR2 is in close proximity to both the alpha-magnet and the immediately preceding quadrupole, it is advisable to check that the calibration of angular deflection vs driving current (obtained from magnetic measurements) is correct. This was done using the alpha-magnet screen, since the transport to this screen from GTL_CORR2 is described by a simple drift-space matrix:

$$\mathrm{r}^{(2)} = \begin{pmatrix} 1 & L_1 + L_2 & 0 & 0 \\ 0 & 1 & 0 & 0 \\ 0 & 0 & 1 & L_1 + L_2 \\ 0 & 0 & 0 & 1 \end{pmatrix}, \tag{3.188}$$

In this section, I will use $\mathrm{r}^{(i)}$ to represent the r-matrix from GTL_CORR2 to point i, where i is 1, 2, or 3 for the crossing-point, alpha-magnet screen, or chopper-screen, respectively. I leave off the dispersive and path length elements to shorten the notation.

This check was carried out using the magnetic measurements to set GTL_CORR2 to a series of nominal horizontal (or vertical) deflection angles, $\theta_{\mathrm{nom,i}}$, and measuring the resulting horizontal (or vertical) displacement, x_i, at the chopper screen. A linear fit to x_i vs $\theta_{\mathrm{nom,i}}$ gives the nominal value of $\mathrm{r}_{12}^{(\mathrm{nom})}$, uncorrected for errors in the deflection angle. Since it is that $\mathrm{r}_{12}^{(2)} = \mathrm{r}_{34}^{(2)} = 0.337 \pm 0.010$mm/mrad (this is just $L_1 + L_2$) the *actual* angular deflection is readily calculated, giving

$$\theta_{\mathrm{act}} = \theta_{\mathrm{nom}} \frac{\mathrm{r}_{12}^{(\mathrm{nom})}(\mathrm{mm})}{0.337 \pm 0.010\mathrm{mm/mrad}} \tag{3.189}$$

Linear least-squares fits to the data from these experiments gave $\mathrm{r}_{12}^{(\mathrm{nom})} = 0.305 \pm 0.006$mm/mrad and $\mathrm{r}_{34}^{(\mathrm{nom})} = 0.322 \pm 0.015$mm/mrad, from which I conclude that

$$\theta_{\mathrm{x,act}} = \theta_{\mathrm{x,nom}} 0.91 \pm .03, \tag{3.190}$$

and

$$\theta_{y,act} = \theta_{y,nom} 0.96 \pm .05. \tag{3.191}$$

3.7.2 Comparison of Experimental Results and Theory

Having corrected the calibration of GTL_CORR2, I then did a series of measurements of $r_{12}^{(3)}$ and $r_{34}^{(3)}$ for various alpha-magnet gradients for constant beam momentum. For these experiments, the low-energy scraper inside the alpha-magnet was set to allow only about $\pm 5\%$ momentum spread through, to lessen any possible ambiguity about what the momentum of the particles seen on the chopper screen was. Spectrum measurements allow the determination of the median momentum of the particles let through, and this quantity was used as the effective momentum of the beam centroid. Table 3.10 summarizes the results.

In order to compare these results to theory, it is necessary to use **serrors**-calculated scaled matrices for the appropriate values of the error parameter M (i.e., $M = \alpha$, for hole-induced errors), to scale these matrices to the values of α listed in the table, and to finally concatenate these matrices with drift space matrices:

$$r = d(L_3)A^{-1}(\alpha)R(M)A(\alpha)d(L_1), \tag{3.192}$$

where d(L) represents the matrix for a drift space of length L. Table 3.11 gives the results of this procedure, listing the r_{12} and r_{34} values corresponding to each of the cases in Table 3.10. Also listed for comparison are the values for a perfect alpha-magnet. These results are displayed in figures 3.19 and 3.20.

As seen from Figure 3.20, the $r_{34}^{(3)}$'s are very sensitive to errors, hence the agreement seen here may be fortuitous. In the same vein, some disagreement is hardly unexpected.

With the exception of the anomalous point at $\alpha = 0.166$, all of the measured r_{12}'s are 5–10% smaller than the theoretical values for the alpha-magnet with errors. The first explanation of the discrepancies in the horizontal plane one might entertain is that the momentum (or, equivalently, the alpha-magnet gradient calibration) is in error by 5–10%. This, however, would not explain the discrepancies observed.

First, the correction of the calibration of GTL_CORR2 would eliminate any effects of momentum errors on deflection angle. Hence, any momentum errors would come into play only through the alpha-magnet. However, as seen from the slope of r_{12} vs α for the theoretical data in Figure 3.19, a very large momentum error would be required to explain the observed discrepancy. For the point with $\alpha = .121$, for example, one would need to postulate a momentum error of about a factor of two, which I do not consider remotely possible. A remaining possibility is that the calibration of GTL_CORR2 is in error, due to inaccurate knowledge of the position of the alpha-magnet screen. A 5–10% error in this calibration would require a 15–30mm error in the position of the screen. This is not inconceivable, given the lack of precision in the screen assembly.

Table 3.10: **Alpha Magnet r_{12} and r_{34} Measurements**

gradient (G/cm)	$<p>$ MeV/c	α 1/cm	$r_{12}^{(3)}$ mm/mrad	$r_{34}^{(3)}$ mm/mrad
255.1 ± 1.3	3.00 ± 0.04	0.160 ± 0.001	-0.743 ± 0.014	0.006 ± 0.005
202.9 ± 1.0	2.71 ± 0.04	0.150 ± 0.001	-0.672 ± 0.012	0.070 ± 0.002
172.8 ± 0.9	2.83 ± 0.04	0.135 ± 0.001	-0.716 ± 0.012	0.120 ± 0.004
149.1 ± 0.7	2.81 ± 0.04	0.126 ± 0.001	-0.730 ± 0.016	0.149 ± 0.004
129.9 ± 0.6	2.80 ± 0.04	0.118 ± 0.001	-0.739 ± 0.018	0.180 ± 0.005

Table 3.11: **Calculated Alpha-Magnet r_{12} and r_{34}**

	alpha-magnet with errors		perfect alpha-magnet	
α 1/cm	$r_{12}^{(3)}$ mm/mrad	$r_{34}^{(3)}$ mm/mrad	$r_{12}^{(3)}$ mm/mrad	$r_{34}^{(3)}$ mm/mrad
0.160	-0.736	0.171	-0.739	-0.021
0.150	-0.745	0.197	-0.749	0.014
0.135	-0.763	0.244	-0.766	0.076
0.126	-0.775	0.279	-0.778	0.120
0.118	-0.788	0.315	-0.790	0.164

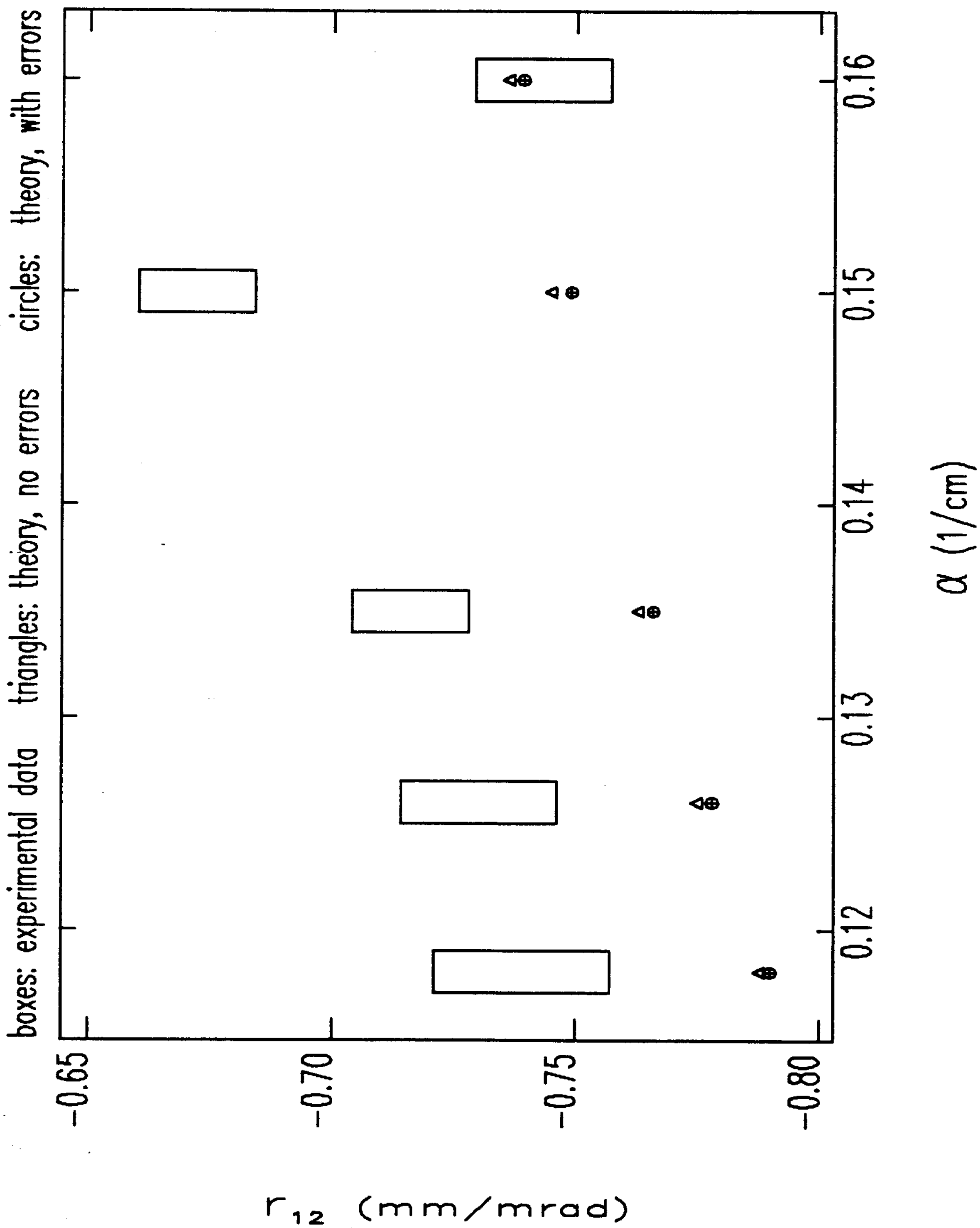

Figure 3.19: Measured and Theoretical Alpha-Magnet r_{12}'s

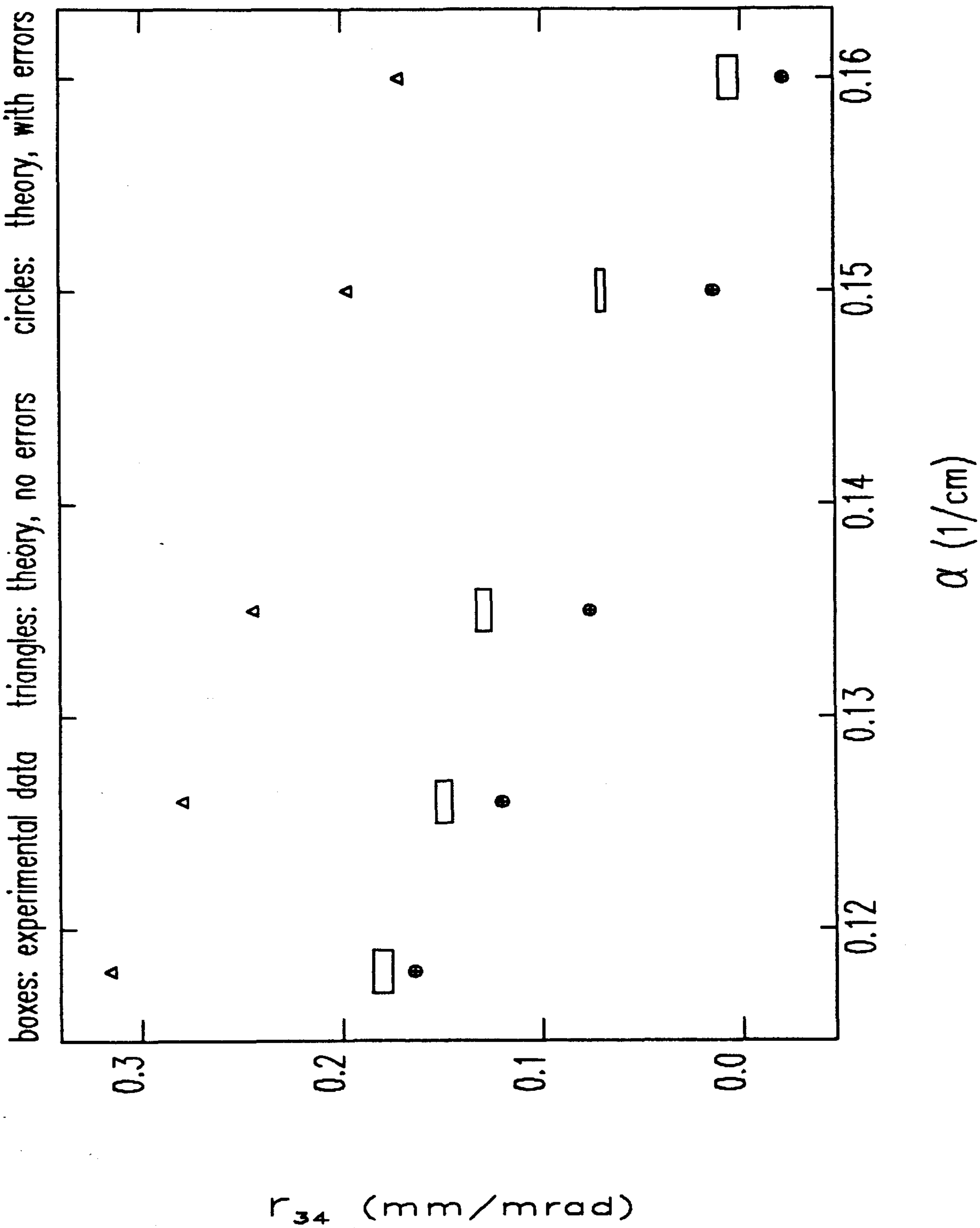

Figure 3.20: Measured and Theoretical Alpha-Magnet r_{34}'s

Chapter 4

Longitudinal Dynamics

In Chapter 2, I described the longitudinal phase-space distribution of the RF gun beam, and indicated that this phase-space ill-suits the beam to direct injection into a S-Band linear accelerator section (here-after referred to simply as "the linac"). In this chapter, I will show why this is so, and how the gun longitudinal phase-space may be transformed into something that is amenable to further acceleration. At issue is the need for a small fractional energy spread, which is required for efficient transport through a subsequent beamline, use as the drive for FELs, and other applications. I shall also show how the rather long (25 ps or so) bunch at the end of the gun can—at least in the absence of excessive errors and space-charge effects—be compressed to a very short 1-2 ps bunch, thus promising the potential of very high peak currents, something that is desirable in FEL applications, among others.

Discussion of the transformation of the gun longitudinal phase-space cannot take place without an understanding of the longitudinal dynamics of electrons in magnetic systems and linear accelerators. I will first discuss longitudinal dynamics in linear accelerators, and in particular how one can predict the longitudinal phase-space at the end of a finite-length accelerator when starting with a beam that is not fully relativistic. This discussion will show why the RF gun beam is unsuited to direct injection into the linac.

I will then discuss how magnetic beamline elements can be used to alter a beam's longitudinal phase-space. Using results from Chapter 3, I will demonstrate that an alpha-magnet has advantages in such an application. I will present the results of optimized alpha-magnet-based bunch compression, with inclusion of detailed longitudinal dynamics calculations, and show how this achieves significantly better results compared to the first-order method of simply injecting the shortest possible bunch into the linac.

Finally, I will present results that include consideration of aberrations in the gun-to-linac transport line, and use these results to compare the SSRL preinjector to other projects.

4.1 Longitudinal Dynamics in Linear Accelerators

There is extensive literature on longitudinal dynamics in linear accelerators[56, 55, 41, 69]. Rather than attempting to duplicate that work here, I shall simply make use of some of the results. In particular, I shall use the commonly-made assumption [41, 55] that the longitudinal electric field of a traveling-wave linear accelerator may be approximated by the first space-harmonic,

$$E_z(z,t) = E \cdot \cos(kz - \omega t), \quad 0 \leq z \leq L, \tag{4.1}$$

where k is the propagation constant, $\omega/(2\pi)$ is the RF frequency, L is the length of the structure (which starts at z=0), and E is a constant. For a velocity-of-light structure such as the SLAC constant-gradient structure used for the SSRL linac, $\omega = kc$, c being the speed of light. While the actual field contains components with propagation constants $k_n = k + \frac{2\pi n}{p}$, where n is an integer and p is the periodic length of the structure[56], these components have phase-velocities ω/k_n less than the speed of light, and hence a relativistic particle will not remain in phase with any but the first space-harmonic. Because of this, the higher space-harmonics impart no net energy to a relativistic beam. Traveling wave accelerators are specifically designed to have small amplitudes in the non-synchronous space-harmonics, since these carry away RF power without contributing to acceleration[56].

The equations of motion for an electron in the presence of this field are found from the Lorentz force. For $0 \leq z \leq L$,

$$\frac{dp}{dt} = -\frac{eE}{m_e c}\cos(kz - \omega(t - t_o) + \phi_o) \tag{4.2}$$

$$\frac{dz}{dt} = \frac{pc}{\sqrt{p^2+1}}, \tag{4.3}$$

where $p \equiv \beta\gamma$ is the momentum and ϕ_o is the initial RF phase for the fiducial particle, which enters the accelerator at $t = t_o$. I will assume that $-eE \geq 0$, so that the fiducial particle is accelerated for $\phi_o = 0$. If $\phi_o < 0$, then the fiducial particle is "behind the crest", meaning that if it is sufficiently non-relativistic, it may fall further behind; if it falls back far enough (or if $\phi_o < \pi/2$) the particle will be decelerated. Similarly, if $\phi_o > 0$, the fiducial particle is "ahead of the crest", meaning that if it is not fully relativistic, it may fall back to be nearer the maximum accelerating phase.

4.1.1 Approximate Treatment for Highly-Relativistic Particles

In general, these equations are unsolvable by analytic means, being coupled and non-linear. However, for $p^2 \gg 1$, the electrons are fully relativistic, and $z = c(t - t_i)$, where t_i is the time at which the particle enters the accelerator. In this case, the acceleration experienced by any particle is constant:

$$\frac{dp}{dt} = -\frac{eE}{m_e c}\cos(-\omega(t_i - t_o) + \phi_o). \tag{4.4}$$

The solution, for $t_i \leq t \leq t_i + L/c$,

$$p(t) = p(t_i) - (t - t_i)\frac{eE}{m_e c}\cos(-\omega(t_i - t_o) + \phi_o), \tag{4.5}$$

may be used to determine the final momentum after an accelerating section of length L:

$$p_f = p_i - \frac{eEL}{m_e c^2}\cos(-\omega(t_i - t_o) + \phi_o), \tag{4.6}$$

where $p_i = p(t_i)$ and $p_f = p(t_f)$.

Since the "useful" electrons out of the RF gun typically have $p \geq 4$, giving $\beta \geq 0.97$, this result is of more than academic interest. Though it is far from exact, it is a useful approximation, and aids the understanding of the detailed results.

The quantity $\phi_i = -\omega(t_i - t_o) + \phi_o$ is the initial phase for some particular particle, even if the particle is non-relativistic. However, for a particle that is initially fully relativistic, the initial phase is also the RF phase throughout the accelerator section. Hence, if it is desired to accelerate a bunch of relativistic particles with small final momentum spread, it is necessary to inject these particles into the accelerator over a sufficiently small time-interval. Suppose that the bunch initially has no momentum spread, and that $\phi_o = 0$ to obtain maximum acceleration of the fiducial particle. Assume further that the fiducial particle is at the center of the bunch, which has length δt. Then the spread in final momenta will be

$$\delta p = (p_f - p_i)(1 - \cos(\omega\delta t/2)), \tag{4.7}$$

where $p_f = p_i - \frac{eEL}{m_e c^2}$ is the final momentum of the fiducial particle. For $\omega\delta t \ll 1$, this implies a fractional momentum spread of

$$\frac{\delta p}{p_f} = \frac{p_f - p_i}{p_f}\frac{\delta\phi^2}{8}, \tag{4.8}$$

where $\delta\phi = \omega\delta t$ is the phase spread of the incoming beam. If the beam is accelerated to very high momentum relative to p_i, then this becomes

$$\frac{\delta p}{p_f} = \frac{\delta\phi^2}{8}, \tag{4.9}$$

and one sees that the final fractional momentum spread is, to first order, quadratic in the initial phase spread if one injects the fiducial (and central) particle at the crest. Hence, in order to obtain a small final momentum spread, one must inject a sufficiently short bunch into the accelerator:

$$\delta\phi \leq \sqrt{8\left(\frac{\delta p}{p_f}\right)_{\text{desired}}}. \tag{4.10}$$

For the SSRL Injector, a fractional momentum spread of less than 0.5% was needed, to accommodate the acceptance of the synchrotron[26]. Hence, from this analysis one would conclude that an initial total phase-spread of less than about 12° is required, *if* one ignores the initial momentum spread in the RF gun beam. I shall show below that, however, that one cannot ignore the initial momentum spread, if one really desires such low final momentum spread. Note that injection with the central particle off the crest will only increase the final momentum spread for a beam with no initial momentum spread, while for a beam that has some initial, time-correlated momentum spread, injection off the crest can be used to compensate the initial momentum spread, as will be seen below.

4.1.2 Numerical Solution and the Contour Approach

Computer methods can easily solve equations (4.2) and (4.3) to high precision, so it is not necessary to attempt to find a solution that is valid for non-relativistic electrons. For the current project in particular, the input longitudinal phase-space distribution is itself not amenable to analytical treatment, but is rather obtained from numerical simulations. Hence, I will move on to discuss computer-aided treatment of this problem.

For some of my computer studies, I employed another pair of equations[41], which are useful if longitudinal motion is one's only interest. Rather than start with the Lorentz equation, one starts with[31]

$$\frac{\mathrm{d m_e c^2}\gamma}{\mathrm{dt}} = -\mathrm{e}\mathbf{v}\cdot\mathbf{E}, \tag{4.11}$$

and assumes the velocity to be parallel to electric field. One form of the resultant equations is (reference [41] gives these equations and a detailed discussion of them)

$$\frac{\mathrm{d}\gamma}{\mathrm{d}\zeta} = \mathcal{E}\cos 2\pi(\zeta-\tau) \tag{4.12}$$

$$\frac{\mathrm{d}\tau}{\mathrm{d}\zeta} = \frac{1}{\beta}, \tag{4.13}$$

where $\zeta = \frac{z}{\lambda}$, $\lambda = \frac{2\pi}{k}$, $\mathcal{E} = -\frac{eE\lambda}{m_e c^2}$, and $\tau = \frac{\omega t}{2\pi}$. The RF phase for any particle at z=0 is particle is $\phi = -2\pi\tau$, which is consistent with the convention I used above. In terms of normalized electric-field $\mathcal{E}$, the change in γ in a section of length L for an initially relativistic particle is

$$\Delta\gamma = \mathcal{E}\Delta\zeta = \mathcal{E}\frac{L}{\lambda} \tag{4.14}$$

There is no particular advantage to these equations over a similarly-scaled form of equations (4.2) and (4.3) for numerical work—I state them because I happened to use them in some of my computations. Specifically, I have written a computer program (`linac_cg`, where "CG" stands for "constant-gradient") that integrates equations (4.12) and (4.13) for a set of particles distributed on a grid over some region of initial (ϕ, p) space. The program computes the final momentum and phase for each particle, and displays the results in contour-plot form. From these, one can deduce the resultant momentum spread and phase spread for any particular injected bunch simply by finding which contours are intersected when the phase-space distribution for the injected bunch is overlayed on the contour graphs. Note that a different plot must be generated for each value of E. For the SLAC-type constant-gradient sections used for the SSRL pre-injector[70], the nominal energy gain per section is given by[6]

$$\Delta\gamma = 20.4\sqrt{\mathrm{P(MW)}}, \tag{4.15}$$

where P is the RF power to the section. Combining this with the previous equation, using L = 3.048m and $\lambda = 0.105$m, I obtain

$$\mathcal{E} = 0.703\sqrt{\mathrm{P(MW)}}. \tag{4.16}$$

While nominal RF power per section for the SSRL Pre-injector Linac is 30 MW, the RF power to the first section is limited operationally to 20 to 25 MW. Since the energy gain scales only as the square-root of the momentum, the differences among these are relatively minor. For this reason, and for brevity, I present only the results for 20 MW RF power, and display these in Figures 4.1 and 4.2.

The horizontal axis for these graphs is the phase, ϕ_i, at which the particle is injected, while the vertical axis is the initial momentum, p_i. As before, $\phi_i > 0$ indicates injection ahead of the RF crest. The contours show lines in (ϕ_i, p_i) space of constant final momentum, p_f, or final phase, ϕ_f. The momentum contours are spaced by $\Delta p_f = 4.2$ and the phase contours by $\Delta\phi_f = 10°$. The labels for the contours are positioned so that the contour closest to the lower left corner of the first letter in the label is the one to which the label applies.

A bunch with an initial longitudinal phase-space distribution that matches a constant final momentum contour will be accelerated to zero momentum spread, and similarly for a bunch that matches a constant final phase contour. Regions where many lines occur in a small area indicate rapidly changing final parameters as a function of initial parameters. Regions where the contour lines are widely spaced indicate slowly changing final parameters as a function of initial parameters.

Examination of Figure 4.1 shows that, as expected from the above analysis, the final-momentum contours are most widely spaced for ϕ_i near zero. The region of widest contour spacing moves to positive ϕ_i as the initial momentum decreases because, for a bunch of non-relativistic electrons, injection at slightly positive ϕ_i results in the bunch center falling back toward $\phi_i = 0$ as the electrons gain energy. If such a bunch were injected at $\phi_i = 0$, it would fall back to $\phi_i < 0$ before reaching relativistic velocities, and as a result the bunch momentum would be decreased while its momentum spread would increase.

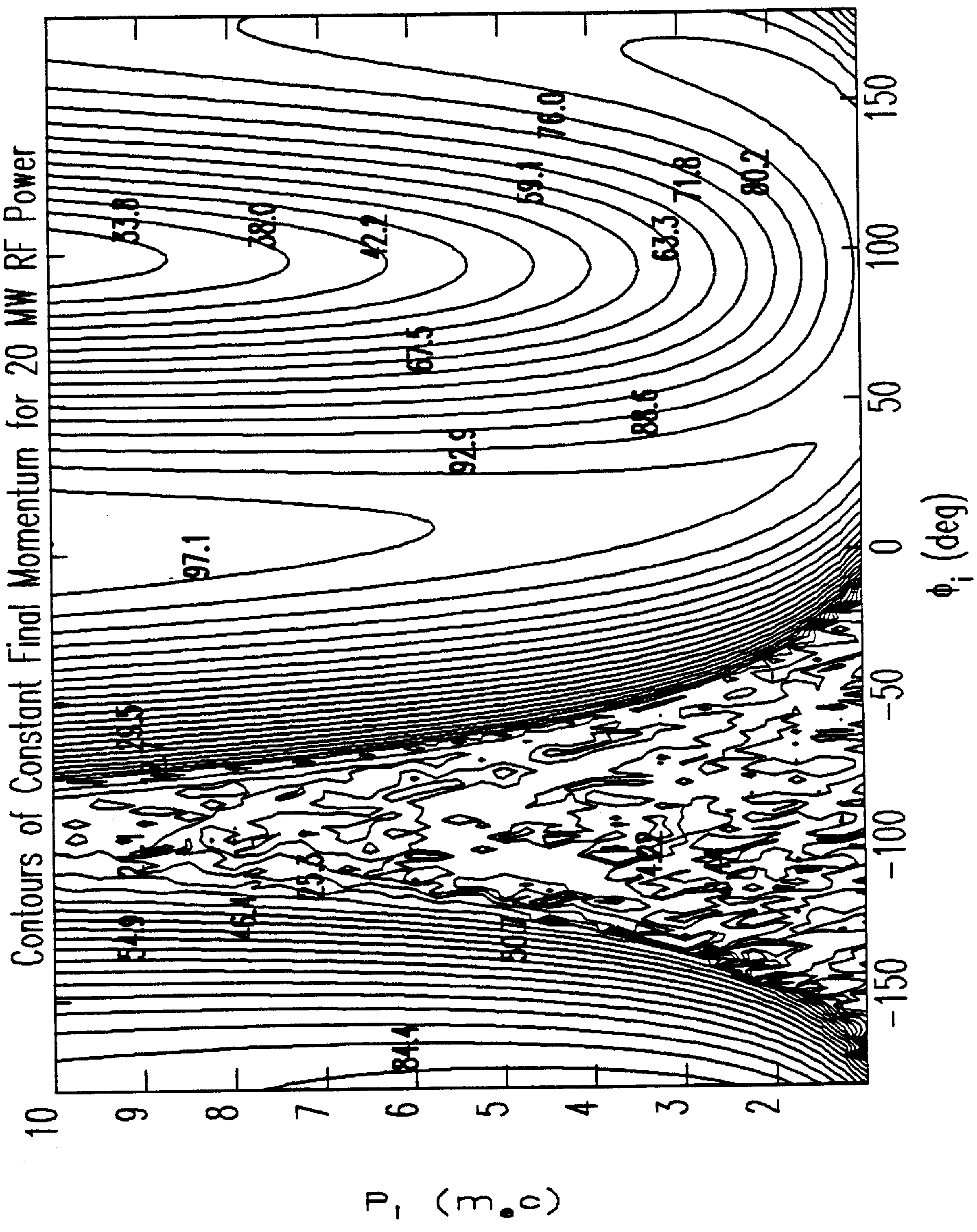

Figure 4.1: Constant Final Momentum Contours

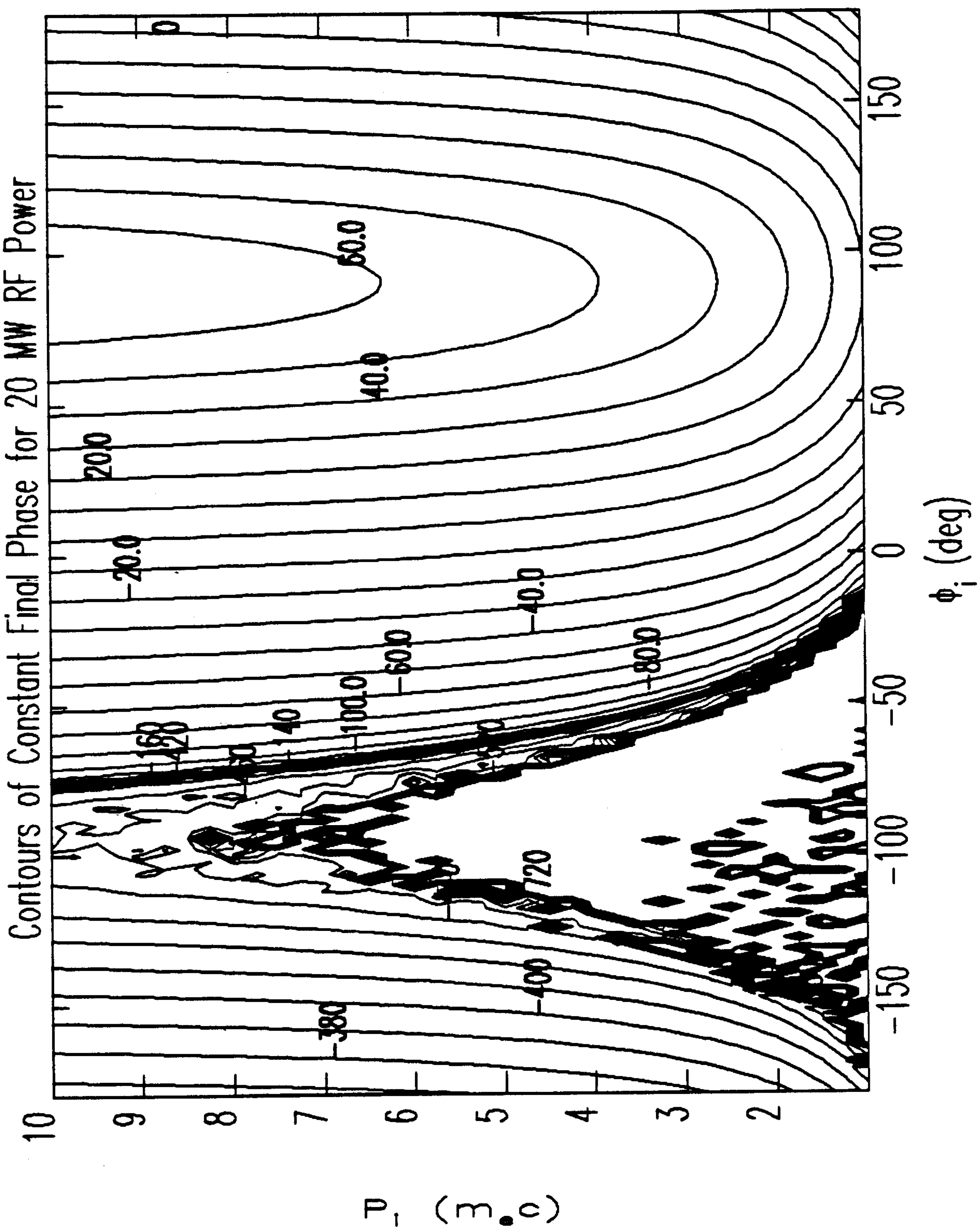

Figure 4.2: Constant Final Phase Contours

For a bunch centered at some phase $-55^\circ \lesssim \phi_i < 0$, the smallest final momentum spread will be achieved when the higher-momentum particles come in behind the lower-momentum particles. Similarly, for a sufficiently high-momentum bunch centered on some phase $0 \lesssim \phi_i \lesssim 30^\circ$, the smallest final momentum spread will be achieved when the higher-momentum particles come in ahead of the lower-momentum particles. In both cases, one can understand this by imagining that a sinusoidally-varying momentum change is simply being added to the initial momenta, as illustrated in Figure (4.3).

For the second of these regions, as the bunch center is moved to smaller momentum and/or larger ϕ_i, one sees another effect come into play. The slope of the constant final-momentum contours changes so that higher-momentum particles must be injected behind lower-momentum particles. In this regime, velocity variation is important. It is necessary to inject the higher-momentum particles so that they will catch up to the lower-momentum particles as the bunch travels down the accelerator. This bunching can contribute to small momentum spread, since once bunched the particles will travel the remainder of the accelerator section at the same phase (provided they are all relativistic by the time they are bunched), thus experiencing the same energy gain in the remainder of the section. (In the jargon of the field, one says that members of such a group of particles all have the same "asymptotic phase".)

The same velocity effect also occurs in the first of the regions mentioned in the paragraph before last, it simply does not cause a change in the slope of the contours, since the slope is required to be the same from both considerations of sinusoidal field variation and velocity variation in the bunch.

For $\phi \gtrsim 90^\circ$, the slope of the constant final momentum contours changes again. In this region, higher-momentum particles must be injected first so that they are decelerated more than lower-momentum particles.

Centered around $\phi_i = -90^\circ$ is a "chaotic" region, where the final momentum and phase of an injected particle depends strongly on the initial momentum and phase. Particles injected into this region are first decelerated, then accelerated again as they fall back relative to the traveling wave. Some of the particles injected here are back-accelerated, exiting the accelerator section at $z = 0$, while others finally exit at $z = L$ only after many cycles of acceleration and deceleration. As expected, the width of this

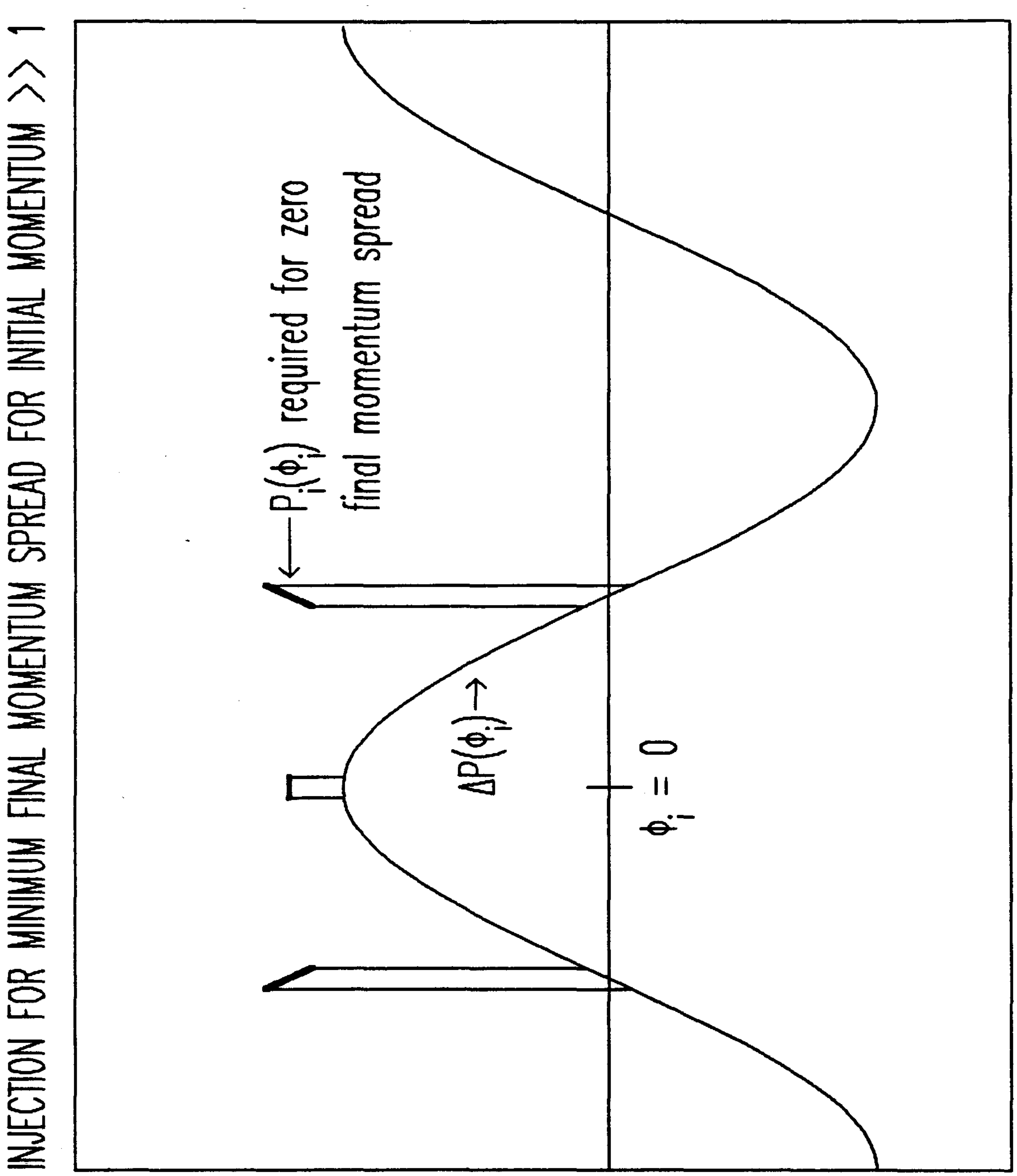

Figure 4.3: Explanation of Slopes of Constant Final-Momentum Contours

region decreases at the initial momentum increases, since particles of higher initial momentum loose less velocity when decelerated by the same fields, and eventually become captured at an accelerating phase.

Figure 4.2 gives additional insight into the longitudinal dynamics. One sees that the contour $\phi_f = 0$ lies in the region $\phi_i \geq 0$, approaching $\phi_i = 0$ as p_i increases. This is because in order for a slow-moving particle to end up at $\phi_f = 0$, it must be injected ahead of the crest so that the velocity-of-light RF wave catches up to it as it becomes relativistic. This effect is less important when the particle is initially highly-relativistic, which is why the contour approaches $\phi_i = 0$ as p_i increases.

This Figure shows that, by and large, in order to obtain a short bunch, one must first *have* a relatively short bunch. The slight slope to the constant ϕ_f contours around $\phi_i = 0$ indicates that it is best to inject the lower momentum particles ahead of the higher-momentum particles in OP bunch, so that the former will fall back to the same phase as the later before the entire bunch becomes relativistic.

In order to get both a short bunch and a small final momentum spread, it is necessary that one inject the bunch along a constant ϕ_f contour in a region where the constant p_f contours are widely spaced. Ideally, one would find two contours, one for constant ϕ_f and one for constant p_f, that coincide over the required interval of p_i, and inject one's bunch with the required phase-space distribution, ϕ_i vs p_i.

Typical operating conditions for the RF gun produce a peak momentum of $p = 5$, with momenta down to $p = 4$ accepted (giving approximately $\pm 10\%$ momentum spread about $p = 4.5$ for the "particles of interest"). As was demonstrated in Chapter 2, the higher momentum particles exit the gun first, with the particles of interest occupying roughly 25 ps, or roughly 25° of S-Band phase. From the above discussion, it is clear that this longitudinal phase-space distribution must be altered so that the higher-momentum particles enter the linac after the lower-momentum particles. (The region $\phi_i > 90$ is ruled out because the particles are decelerated before being accelerated, which is undesirable as it would lead to increased space-charge effects.) This can be accomplished by means of magnetic compression, as will be shown in the next section of this chapter. For present purposes, I shall assume that the magnetic compression system can supply the desired momentum-time correlation, and attempt to locate the optimum phase for injection in order to get the smallest final momentum spread and bunch length.

I used `linac_cg` to compute the constant final-momentum and final-phase contours for the region $-50^\circ \leq \phi_i \leq 90^\circ$ and $3 \leq p_i \leq 6$, with $\Delta\phi_i = 1^\circ$ and $\Delta p_i = 0.1$. For reasons discussed below, the region $-10 \leq \phi_i \leq 20$ is of particular interest. This region is shown in Figures 4.4 and 4.5.

From the previous set of Figures, one sees that for $\phi_i \lesssim -20^\circ$, the contours of constant p_f and those of constant ϕ_f are most nearly parallel. This indicates that if the initial phase-space distribution could be shaped to match the contours in this region, then this might be the best place to inject. The problem with injection in this region is that since the contours of constant p_f are equispaced in Δp_f, the fractional momentum spread between the contours in this region is larger than for those just ahead of the crest. In addition, these contours are much more closely-spaced in ϕ_i than those nearer the crest. Hence, injection in this region is unlikely to yield good results in practice, since it is unlikely that the initial bunch phase-space could be tailored to the contours sufficiently well to obtain low final momentum spread.

From the Figures, I conclude that injecting closer to the crest, but still behind it by a few degrees looks promising, as does injection ahead of the crest by perhaps 15-20 degrees. The latter region suffers more from crossing of the contours of constant ϕ_f and constant p_f. Clearly, some compromise will have to be made between minimum final phase-spread and minimum final momentum spread. How one makes this compromise depends on one's application. For example, if additional accelerator sections follow, then it is probably best to inject into the first section so as to minimize the phase-spread at exit, so that all particles have, as much as possible, the same phase in all subsequent accelerator sections. This will ensure that the absolute momentum spread does not grow, in additional to giving the shortest bunch. As the bunch goes through subsequent sections, the fractional momentum spread will be further decreased.

The SSRL preinjector has a total of three accelerator sections. Hence, I will attempt to optimize injection into the first section primarily in order to obtain a short bunch. Having narrowed down the range of initial phase to be considered, it is next necessary to include details of the initial bunch phase-space distribution. This requires discussion of magnetic compression, which I go into immediately in the next section, returning to the combined problem in the section after next.

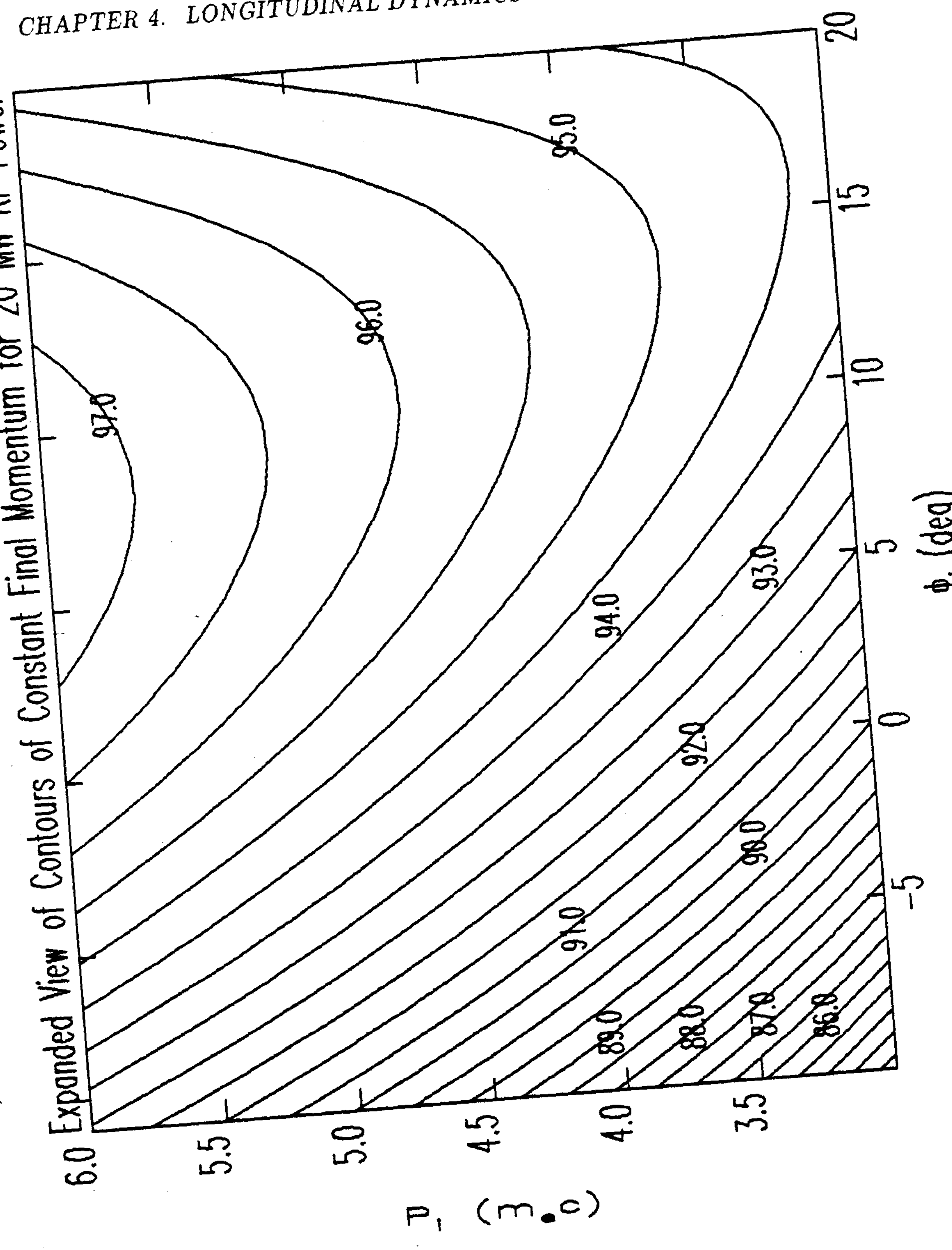

Figure 4.4: Expanded View of Constant Final Momentum Contours

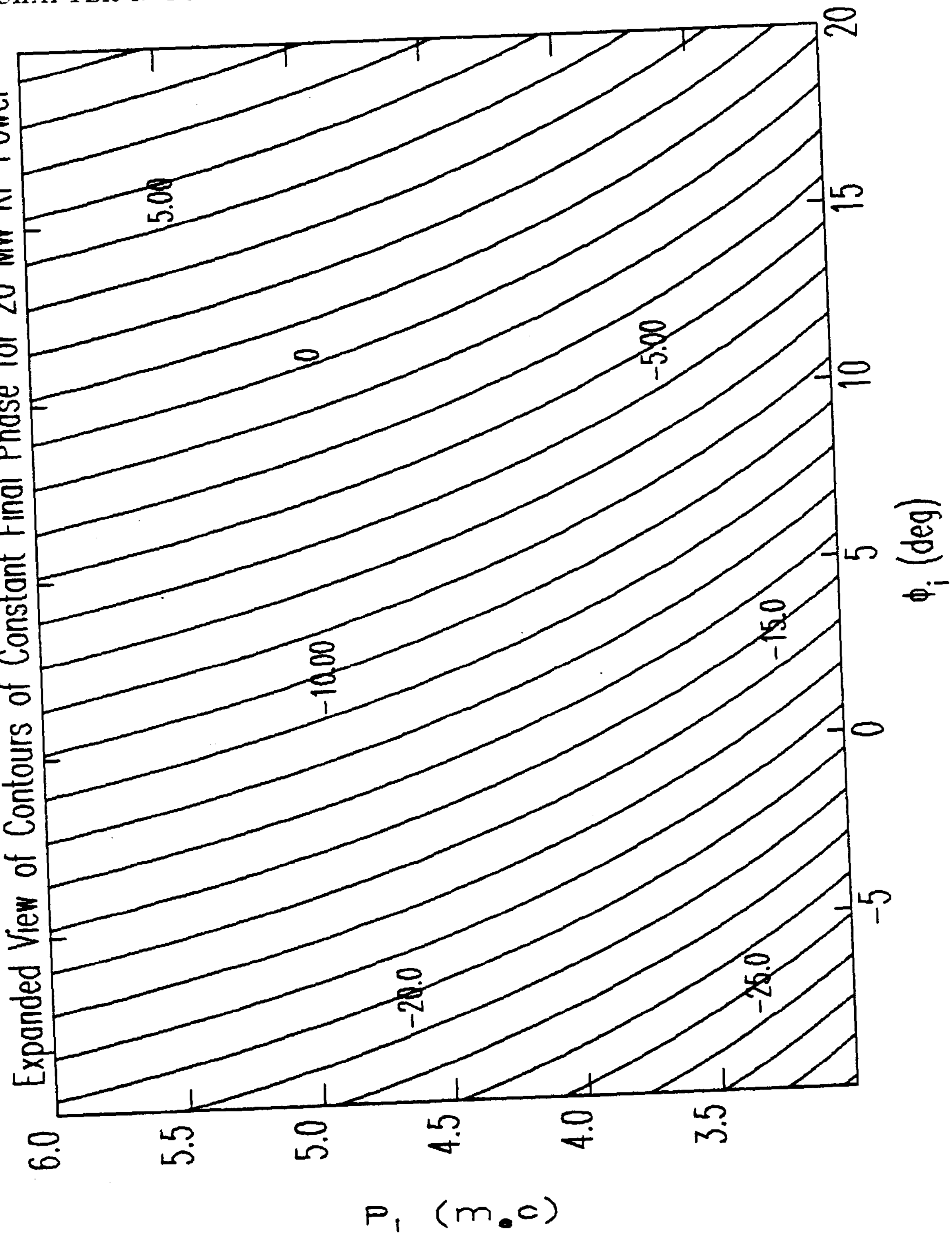

Figure 4.5: Expanded View of Constant Final Phase Contours

4.2 Magnetic Bunch Compression

In the previous section I have shown that, roughly speaking, what one wants is to deliver to the linac the shortest possible bunch. More precisely, one wants a bunch with a longitudinal phase-space distribution at the beginning of the linac that will be compressed further during initial acceleration. This depends upon being able to reverse the time-order of electrons within each RF gun bunch, so that the lowest momentum particles enter the linac first and subsequently fall back to the same phase as the highest momentum particles. Hence, a magnetic bunching system will have to be able to accomplish some degree of time-order reversal of particles in the bunch, over a sufficiently large momentum interval. However, this is typically only slightly more difficult that producing a very short bunch at the entrance of the linac, and so it is convenient to think in terms of how to produce a very short bunch. This allows a separation of the problem of magnetic bunching from the details of longitudinal dynamics in the linac, and hence prevents the issues from being obscured by too much detail at the outset. Once the mechanism of magnetic bunching has become clear, it is then possible to go back and consider the effects of longitudinal dynamics in the first part of the linac.

4.2.1 First Order Solution for Bunch Compression

Consider, then, that it is desired to produce a very short bunch at the entrance of the linac. It is known that the bunches from the gun have a particular momentum vs. exit-time characteristic, namely, that higher-momentum electrons exit the gun ahead of lower-momentum electrons. It is convenient to use the momentum deviation, $\delta \equiv (\mathrm{p} - \mathrm{p_o})/\mathrm{p_o}$, in terms of which, for a sufficiently small momentum interval about the central momentum $\mathrm{p_o} \equiv (\beta\gamma)_\mathrm{o}$,

$$\mathrm{t_{exit}}(\delta) \approx \mathrm{t_o} + \left(\frac{\mathrm{dt_{exit}}}{\mathrm{d}\delta}\right)_\mathrm{o} \delta, \tag{4.17}$$

where $\mathrm{t_{exit}}$ refers to the time of a particle's exit from the gun and

$$\left(\frac{\mathrm{dt_{exit}}}{\mathrm{d}\delta}\right)_\mathrm{o} < 0. \tag{4.18}$$

(Examination of the longitudinal phase-space distributions shown in previous chapters shows that, for the ±10% momentum spread that will be used, this linear approximation is not exact. However, it is again not my purpose now to deal with this detail, but rather to explain the principle.) What is desired in order to have a very short bunch at the end of the bunching system is that

$$t_{\text{arrival}}(\delta) = t_{\text{exit}}(\delta) + \Delta t_{\text{flight}}(\delta) = \text{constant}, \tag{4.19}$$

where the subscript "arrival" refers to arrival at the end of the bunching system (i.e., the entrance to the linac) and where I use Δt_{flight} to indicate that the time-of-flight is an interval rather than the time of some event. Combining these and using the linear approximation of equation (4.17), I obtain

$$t_{\text{arrival}}(\delta) = t_o + \left(\frac{dt_{\text{exit}}}{d\delta}\right)_o \delta + \Delta t_{\text{flight}}(\delta) = \text{constant}, \tag{4.20}$$

and hence

$$\left(\frac{dt_{\text{arrival}}}{d\delta}\right)_o = \left(\frac{dt_{\text{exit}}}{d\delta}\right)_o + \left(\frac{d\Delta t_{\text{flight}}}{d\delta}\right)_o = 0. \tag{4.21}$$

From this last equation and equation (4.18), one can see that

$$\left(\frac{d\Delta t_{\text{flight}}}{d\delta}\right)_o = -\left(\frac{dt_{\text{exit}}}{d\delta}\right)_o > 0 \tag{4.22}$$

must be obtained at the end of the bunching system. In words, since higher momentum particles come out ahead of lower momentum particles, they must be put through a system in which the time of flight is longer for high-momentum particles in order for all particles to arrive at the end at the same time.

For particles that are not fully relativistic, time-of-flight depends upon both velocity and the length of the path taken

$$\Delta t_{\text{flight}} = \frac{s(\delta)}{\beta c} \tag{4.23}$$

where $s(\delta)$ represents the length of the path taken by a particle with momentum deviation δ. Since $\beta = p/\sqrt{(p^2+1)}$, it follows, to first order in δ, that

$$\frac{1}{\beta} = \frac{1}{\beta_o} + (\beta_o - \frac{1}{\beta_o})\delta. \tag{4.24}$$

Expanding $s(\delta)$ to first order as well, one obtains

$$\left(\frac{d\Delta t_{flight}}{d\delta}\right)_o = \frac{s_o}{c}(\beta_o - \frac{1}{\beta_o}) + \frac{1}{\beta_o c}\left(\frac{ds}{d\delta}\right)_o . \tag{4.25}$$

The first term of this expression shows that for highly relativistic particles, for which $\beta_o \to 1$, the effect of velocity variation on time-of-flight disappears, as would be expected. For non-relativistic particles, this term is negative, indicating that velocity effects will fight the bunching process. This is again expected, since the higher velocity of higher-momentum particles will help them to "pull ahead" even further. Clearly, if *bunching* is to occur, it will come from the variation of path-length with momentum.

4.2.2 Achieving Momentum-Dependent Path Length

Until now, I have said nothing about how one achieves a momentum-dependent path-length, although the name of this section is an indication. If particles of different momenta are to have different path-lengths in going through a transport line, they must of course first be made to take different paths through that system. In addition, these different paths must have different lengths. For example, merely sending particles of different momentum through a drift space at different transverse positions will not produce the desired effect. To see what is needed, consider first the expression for the path length in a transport line without bending magnets, where the central particle travels a straight-line path:

$$s(\delta) = \int_0^{s_o} \sqrt{1 + x'^2(s_o, \delta)} ds_o, \tag{4.26}$$

where the integration is with respect to the path length for the central particle. To first order there is no variation of path-length with momentum in such a beamline.

Now allow the central particle to traverse a section of a wedge bending magnet that bends it through an angle $\Delta\theta_o$, as illustrated in Figure 4.6. The path length for the central particle is given by $\Delta s_o = \rho_o \Delta\theta_o$, where ρ_o is the bending radius for the central particle. For an arbitrary particle, the path length is given by $\Delta s = \rho\Delta\theta$, where

$$\rho = \rho_o(1 + \delta), \tag{4.27}$$

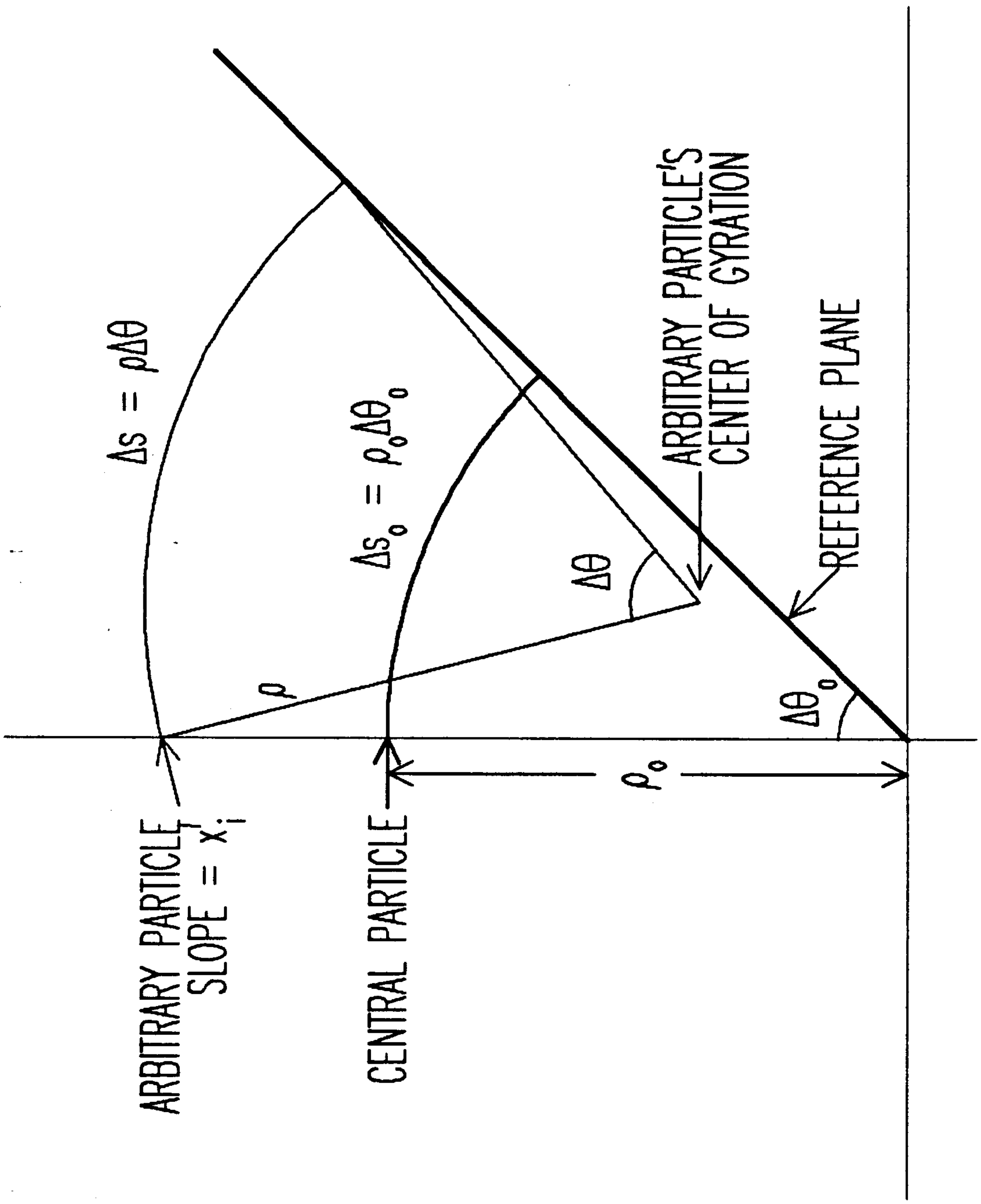

Figure 4.6: Particle Motion in a Wedge Bending Magnet

and where θ is the angle the particle is bent through in reaching the reference plane, as illustrated in Figure 4.6.

Particles other than the central particle will in general enter the bending magnet with different momenta, positions, and slopes relative to the central particle. Let x_i and x_i' be the initial position and slope of a particular particle, respectively. Some trigonometry reveals that the angle through which an arbitrary particle is bent is

$$\Delta\theta = \Delta\theta_o + \mathrm{atan}(x_i') + \mathrm{asin}\left\{\frac{\rho_o + x_i}{\rho}\sin(\Delta\theta_o) - \sin\left[\Delta\theta_o + \mathrm{atan}(x_i')\right]\right\}. \quad (4.28)$$

So far, no approximations have been made beyond assuming an ideal, hard-edge magnetic field. In order to get a first-order expression for the differential path-length in an infinitesimal section of a bending magnet, I expand to first-order in $\Delta\theta_o$, x_i, and x_i', obtaining

$$\Delta s = \rho\Delta\theta = \Delta\theta_o(\rho_o + x_i). \quad (4.29)$$

The initial coordinate x_i is at this point arbitrary. I am interested, however, only in momentum-dependent effects, and hence I will assume that the position of any particle at the entrance is a function only of its momentum, through the dispersion function D, defined by

$$x_i(\delta) = D\delta + \mathcal{O}(\delta^2). \quad (4.30)$$

Hence, the differential path-length is

$$\Delta s = \Delta s_o(1 + \frac{D}{\rho_o}\delta), \quad (4.31)$$

from which I conclude that

$$\frac{ds}{d\delta} = \int_0^{s_o} \frac{D(s_o)}{\rho_o} ds_o, \quad (4.32)$$

(I use the total derivative because x_i and x_i' are assumed to depend on δ, i.e., this quantity is not necessarily the matrix element r_{56} (it is equal to r_{56} only when the integration starts from a point where D=0).)

Referring back to equations (4.22) and (4.25), one sees that positive $\frac{ds}{d\delta}$ is required for bunch compression. This is obtained when D and ρ have the same sign, which is always the case for dispersion generated within the magnet itself (otherwise $\frac{ds}{d\delta}$ could be negative for a lone bending magnet, which is absurd). I define the sign of D with respect to a right-handed coordinate system (x, y, z), with $\hat{\mathbf{z}}$ along the direction of motion and $\hat{\mathbf{y}}$ along the upward vertical, so that for positive dispersion a larger momentum deviation implies a larger x coordinate. Hence, positive dispersion is generated by a bend to the right. The sign of ρ, as well as the sign of θ, for a bending magnet is then required to be the same as the sign of the dispersion it generates. This ensures that Δs_o is positive and that a lone bending magnet produces positive $\frac{ds}{d\delta}$. This is consistent with the conventions used by the beamline program MAD[71] and the tracking program **elegant**[49].

4.2.3 Options for Implementing Magnetic Compression

From this discussion it is clear that a single bending magnet could be used to provide bunch compression. However, there is inevitably dispersion at the end of a system with a single bending magnet, which is undesirable as it increases beam-size, effectively increasing the beam emittance. The next obvious step is to use two bending magnets of the same sign, with a focussing quadrupole between them to match the dispersion to zero at the end of the second bend (see Steffen[67] for examples of such systems). Such a system has a number of advantages, a principle one being that chromatic aberrations can be corrected through the addition of sextupoles between the bending magnets. However, there is the disadvantage that, since the bending angles of the magnets are fixed by the requirement of steering the central momentum down the center of the beamline, the bending radius ρ is fixed for each magnet, and hence D and $\frac{ds}{d\delta}$ are also fixed. Such a system is thus unsuitable for situations requiring variable compression, such as is needed for the RF gun, where $\frac{dt_{exit}}{d\delta}$ varies with p_o (i.e., as a function of the RF field level in the gun). Since the RF gun was still under development when the bunch compression system was being designed, it was not known before-hand what the operating momentum would be, and hence a system with variable compression was desirable.

For this reason it was decided to use a different type of magnetic-bunch compression scheme, namely one employing an alpha-magnet. The properties of this magnet are covered in detail in a Chapter 3. For present purposes, I will simply state that it is first-order achromatic but has momentum-dependent path-length described by

$$s_\alpha(\delta) = K_\alpha \sqrt{\frac{p_o(1+\delta)}{g}}, \tag{4.33}$$

where s is in meters, g is the gradient in G/cm, $K_\alpha = 1.91655$, and, as above, $p_o = (\beta\gamma)_o$. From this, it is seen that for the alpha-magnet

$$\left(\frac{ds_\alpha}{d\delta}\right)_o = \frac{1}{2} K_\alpha \sqrt{\frac{p_o}{g}}. \tag{4.34}$$

Like bending-magnet-based schemes, an alpha-magnet provides momentum-dependent path-length because of bending and the resultant dispersion. However since the alpha-magnet is a gradient magnet, the bending radius varies with position along the central trajectory. The alpha-magnet has the advantage that the gradient, and hence $\frac{ds_\alpha}{d\delta}$, can be varied without changing the central trajectory outside of the alpha-magnet. While there are other systems with this property[72], the alpha-magnet is probably the simplest. It also has the advantage of relatively small aberrations, but has the disadvantage that there is no simple way to incorporate sextupoles for correction of chromatic aberrations in external quadrupoles that might be required as part of the beamline.

Evaluating (4.33) for $\delta = 0$, and inserting the result along with equation (4.34) into (4.25), and thence into (4.22), I obtain the requirement for bunching

$$\frac{1}{c}\left(K_\alpha \sqrt{\frac{p_o}{g}} + L_{drift}\right)\left(\beta_o - \frac{1}{\beta_o}\right) + \frac{K_\alpha}{2\beta_o c}\sqrt{\frac{p_o}{g}} = -\frac{dt_{exit}}{d\delta}, \tag{4.35}$$

where I have used

$$s(\delta) = L_{drift} + s_\alpha(\delta) \tag{4.36}$$

to incorporate the effects of any drift spaces between the gun and alpha-magnet and between the alpha-magnet and linac. It will prove useful to group the alpha-magnet terms together, as in

$$\frac{L_{drift}}{c}\left(\beta_o - \frac{1}{\beta_o}\right) + \frac{K_\alpha}{c}\sqrt{\frac{p_o}{g}}\left(\beta_o - \frac{1}{2\beta_o}\right) + \frac{dt_{exit}}{d\delta} = 0. \tag{4.37}$$

Solving for the gradient, I obtain

$$g = \frac{p_o K_\alpha^2 \left(\beta_o - \frac{1}{2\beta_o}\right)^2}{\left[c\frac{dt_{exit}}{d\delta} + L_{drift}\left(\beta_o - \frac{1}{\beta_o}\right)\right]^2}. \tag{4.38}$$

This equation reveals a number of aspects of bunch-compression with an alpha-magnet. Since $\frac{dt_{exit}}{d\delta} < 0$ and $\beta_o - \frac{1}{\beta_o} < 0$, the denominator will be zero only if $L_{drift} = 0$ and the initial bunch has zero length, i.e., only if bunching is not needed. One also sees that the longer the drift spaces, the lower the alpha-magnet gradient must be, in order to compensate for the debunching.

The term $(\beta_o - \frac{1}{2\beta_o})^2$ in the numerator combines the effects of debunching in the alpha-magnet due to differential velocity with that of bunching in the alpha-magnet due to differential path-length. Note that the solution (4.38) is not valid for $\beta_o < 1/\sqrt{2}$, since then all terms on the left-hand side of (4.37) are negative. Hence, for $\beta_o < 1/\sqrt{2}$, the alpha magnet *cannot* bunch, as the effects of velocity variation will always overcome the effects of path-length variation. (This is false only if $\frac{dt_{exit}}{d\delta} > 0$, a situation that does not apply for the RF gun.)

Taking the limit of equation (4.38) as $\beta_o \rightarrow 1$, one obtains

$$\lim_{\beta_o \rightarrow 1} g = \frac{p_o K_\alpha^2}{\left(2c\frac{dt_{exit}}{d\delta}\right)^2}, \tag{4.39}$$

which indicates that for constant bunch length and constant fractional momentum spread (implying constant $\frac{dt_{exit}}{d\delta}$), the gradient must increase with increasing central momentum. If, however, the *absolute* momentum spread is kept constant (as happens with acceleration of relativistic particles near the crest of the RF field), then $\frac{dt_{exit}}{d\delta}$ scales as p_o, which indicates that the gradient must scale inversely with momentum. A smaller gradient implies a larger alpha magnet, since the size of the central trajectory scales as $1/\sqrt{g}$ (see Chapter 3). Hence, bunching before acceleration is advantageous in that it decreases the size of the alpha-magnet, at the cost of requiring a higher gradient. Similarly, as $\beta_o \rightarrow 1/\sqrt{2}$ from $\beta_o > 1/\sqrt{2}$, the gradient must become vanishingly small, implying a increasingly large alpha-magnet.

4.3 Optimized Bunch Compression for the RF Gun

In the previous two sections, I discussed the principles that must be employed in choosing the injection phase and the alpha-magnet gradient for production of short bunches with low final momentum spread. I attempted to separate the two aspects, for simplicity in the discussion. In this section, I demonstrate how to obtain optimum performance with simultaneous consideration of acceleration and magnetic bunching, along with inclusion of the detailed initial phase-space. Not surprisingly, this optimization is best done numerically.

I have written a program, **`alpha_opt`**, that accepts initial longitudinal phase-space information in terms of (ϕ_i, p_i) pairs for macro-particles (e.g., from MASK or **`rfgun`**) and attempts to find the optimum alpha-magnet gradient for a specified accelerator phase and energy gain. It optimizes for either the minimum mean absolute phase deviation or the minimum total phase-length of the final bunch, though I have used the latter criterion exclusively in this work. Equation (4.33) is used without approximation in (4.36) to give the momentum-dependent path-length. Equation (4.1) is used for the traveling wave field. To simulate particle motion in the accelerator, I employ equations (4.2) and (4.3) (scaled for more efficient computation), which I integrate using the so-called "leap-frog" method[61], which is second-order accurate in the time-step. Typically, I find that taking time-steps smaller than 30 ps makes no change in the results (i.e., no change of more than ± 0.001ps in the bunch length).

4.3.1 Use of `alpha_opt` to Optimize Bunch Compression

The combined distance, L_{drift}, from the gun to the alpha-magnet and from the alpha-magnet to the center of the first linac cell (where the traveling wave begins) was chosen based on simulations of the gun longitudinal phase-space, the anticipated strength and good-field-region of the alpha-magnet, and the need for a sufficiently long drift-space to accommodate the quadrupoles and chopper. Because the gun was still under development at the time the alpha-magnet and GTL were being specified, I chose L_{drift} so that compression would be feasible over a wide range of gun operating momenta, rather than finding an optimum for any particular beam momentum. If L_{drift} were chosen to be too short, then an excessively strong alpha-magnet would be needed in order to reduce the compression, while if L_{drift} were chosen to be too long, an unreasonably large good-field region would be needed to provide more compression. $L_{drift} = 1.5m$ was initially chosen based on preliminary simulations with **rfgun** and **alpha_opt**, along with knowledge of the (then preliminary) magnetic design of the alpha-magnet. Later, L_{drift} was increased to 1.7m in order to provide more space for other GTL components.

More specifically, there is a 0.6m drift space from the gun to the alpha-magnet crossing point, and a 1.1m drift from the alpha-magnet to the linac. See Chapter 5 for more discussion of the layout of the GTL.

I performed a series of **alpha_opt** runs starting with the MASK-generated longitudinal phase-space distribution for the RF gun operated at $E_{p2} = 75MV/m$ and $J = 10A/cm^2$. The linac simulation parameters were such that an initially relativistic particle injected at the crest would gain 45 MeV (which corresponds to 20.7 MW RF power). I took the highest-momentum particle as the fiducial particle, and chose to attempt to compress the beam for a variety of momentum spreads, namely $\pm 10\%$, $\pm 5\%$, and $\pm 2.5\%$. That is, I applied a perfect momentum-filter to the MASK-generated beam, accepting only particles such that $p_c(1-f) \leq p \leq p_c(1+f)$, with $p_c \equiv p_{max}/(1+f)$, where $\pm f$ is the fractional momentum spread accepted. In this way, the selected momentum range always contains the highest momentum particles. (This same capability exists on the actual beamline, where a scraper inside the alpha-magnet can be moved into the beam from the low-momentum side.)

For each value of f, I first found the alpha-magnet gradient which produced the shortest bunch at the entrance to the linac. I then used this gradient and sent the bunch down the linac with the highest-momentum particle injected at the crest, fully expecting that the result would be a less than optimally compressed bunch. The simulations confirmed this expectation, as the data listed in Table 4.1 shows. (In this and all subsequent Tables and Figures, Δt and ΔP are the full spread of the values, e.g., $\Delta t = t_{max} - t_{min}$.) In addition, one sees that the absolute moment spread has increased. The phase-space distributions at the linac entrance and exit are represented graphically in Figure 4.7. Note that these graphs are of *time* and momentum, rather than phase and momentum, and that particles to the left are ahead of particles to the right. As expected, the initially higher-momentum particles pull ahead of the initially lower-momentum particles, resulting in a longer final bunch.

Table 4.1: **Optimization for a Short Bunch at the Linac Entrance**

$\Delta p/p$ (%)	Q (pC)	g_α (G/cm)	Δt_i (ps)	Δp_i ($m_e c$)	Δt_f (ps)	Δp_f ($m_e c$)
±10	110.9	335.40	1.050	0.978	3.030	1.808
±5	80.3	338.32	0.724	0.513	1.285	0.818
±2.5	50.4	321.22	0.493	0.263	0.750	0.436

The conclusion to be gained from this result is that it is not sufficient to design a compression system that will generate a short bunch at the entrance to the linac. It is necessary to take into account the longitudinal dynamics in the linac in order to ascertain whether one can indeed produce a very short bunch at the end of the linac. In the present case, one expects that what is needed is to increase the compression (by using smaller gradients in the alpha-magnet) so that the lower-momentum particles enter the accelerator ahead of the higher-momentum particles. This expectation is confirmed by `alpha_opt`.

I directed `alpha_opt` to optimize the alpha-magnet for the shortest bunch at the end of the linac. The same linac parameters were used as before. The optimum alpha-magnet gradients are smaller than previously found. Table 4.2 lists the results for this optimization. The phase-space distributions at the linac entrance and exit are represented graphically in Figure 4.8. One sees that for this optimization the increase in the absolute momentum spread is significantly smaller than for the previous optimization. The explanation is that the final bunch length is achieved a relatively short distance into the accelerator section (because the particles are already relativistic), and hence in the previous optimization the bunch had a large phase-spread during most of the acceleration, resulting in an increase in momentum spread.

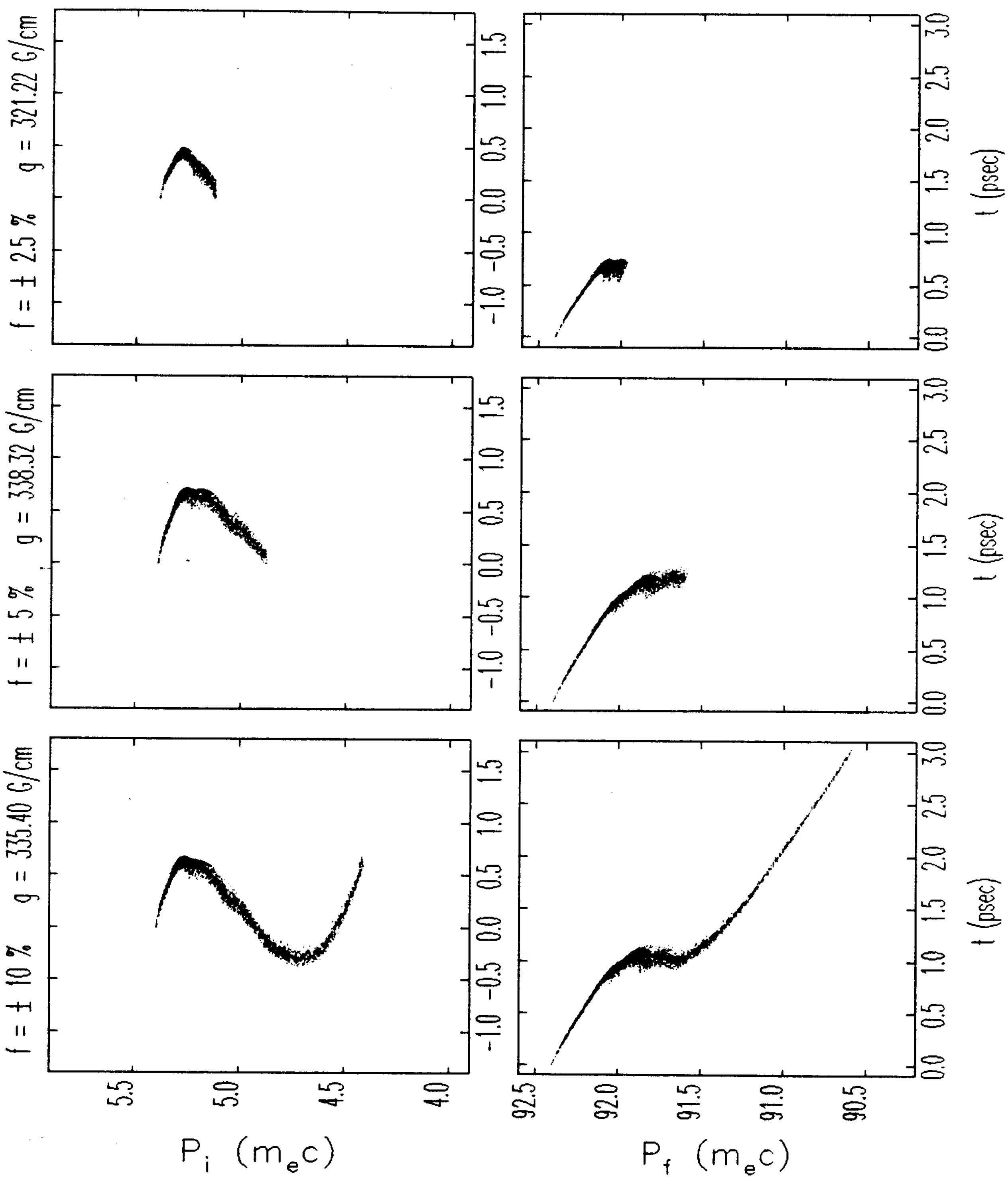

Figure 4.7: Result for Compression Optimized for a Short Bunch at Linac Entrance

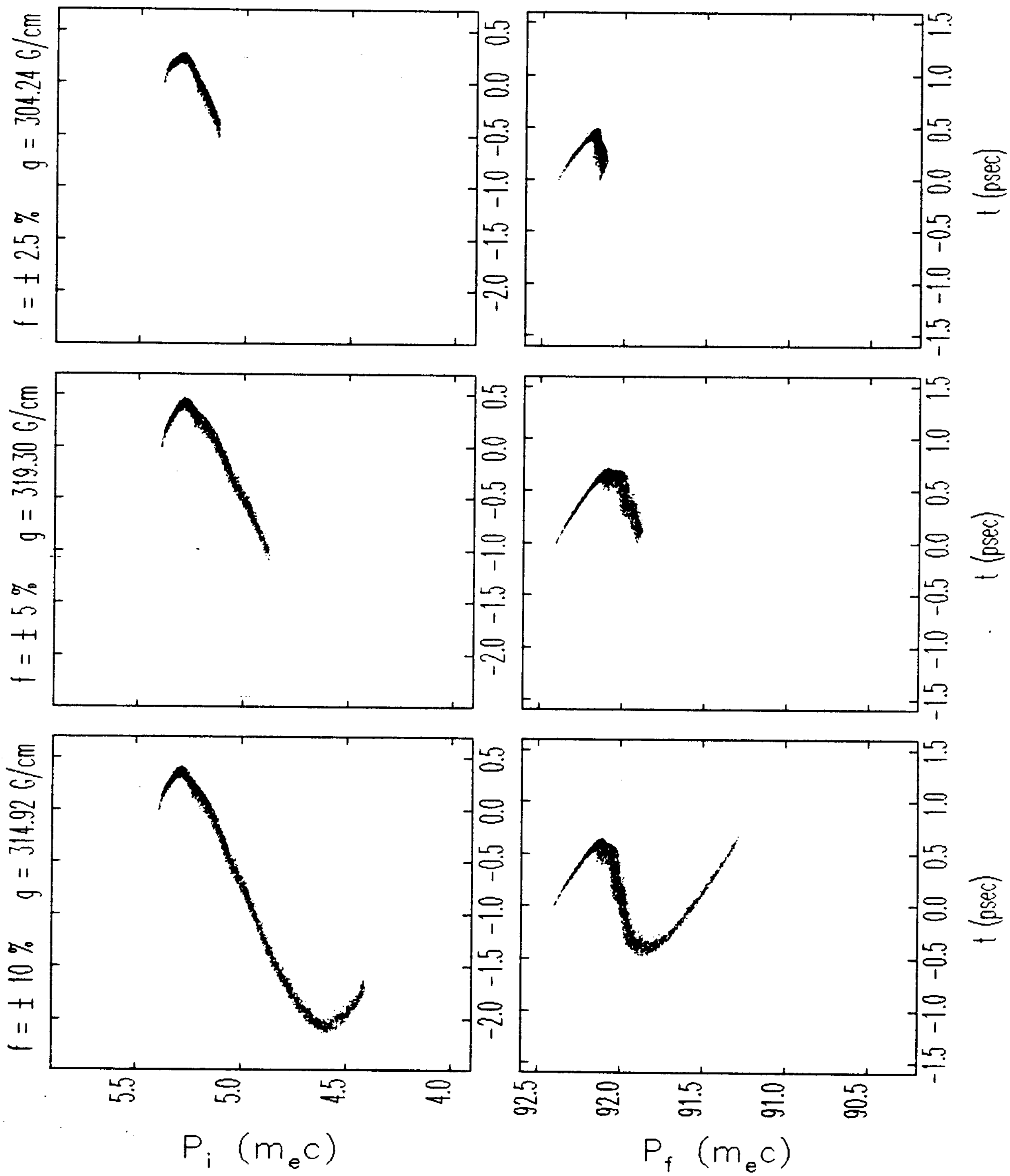

Figure 4.8: Results for Compression Optimized for a Short Bunch at Linac Exit

Table 4.2: **Optimizations for a Short Bunch at the Linac Exit**

$\Delta p/p$ (%)	g_α (G/cm)	Δt_i (ps)	Δp_i ($m_e c$)	Δt_f (ps)	Δp_f ($m_e c$)
± 10	314.92	2.548	0.978	1.139	1.112
± 5	319.30	1.556	0.513	0.719	0.527
± 2.5	304.24	0.810	0.263	0.496	0.297

4.3.2 Optimization of the Injection Phase

For $\Delta p/p = \pm 10\%$, I have done an additional series of simulations, designed to investigate the effect of the initial phase of the fiducial particle. In particular, I repeated the optimization for a series of values of the initial phase of fiducial particle. The results are listed in Table 4.3 and displayed graphically in Figure 4.9. Notice that the smallest final momentum spread and the highest average final momentum are achieved by injecting the bunch $10 - 15°$ ahead of the crest, so that it falls back to the crest before becoming fully relativistic. The smallest final bunch length is achieved for $\phi_o = 20°$. As might have been expected from the contour method of the previous section, the optimizations for highest total momentum gain, smallest final momentum spread, and smallest final bunch length are to some extent incompatible, though not grossly so. While some advantage in terms of final bunch length is obtained by accelerating well off the crest, the advantage is small and is obtained at the expense of considerably higher final momentum spread. That this should be so is confirmed by the contour-plots of the first section, where one sees that the contours of constant final phase become more widely spaced as ϕ_i increases from zero up to around 90°. The explanation is, perhaps, that injecting further from the crest allows a longer time for the particles to bunch before they are fully relativistic. Presumably, if this explanation is correct, one would find the optimum injection phase for the shortest bunch becoming smaller as one decreased the rate of acceleration.

The reader may notice that the numbers for $\phi_o = 0$ in Table 4.3 are different from those in Table 4.2. The reason for this is that for the optimizations presented in Table 4.3, I used a sample of the MASK-generated longitudinal phase-space distribution containing only 20% of the macro-particles in order to economize computer resources, whereas in the previous two Tables I used all the macro-particles (3461 macro-particles for ±10% initial momentum spread). Each set of data is self-consistent in the size of the sample used.

Table 4.3: **Optimizations for Δp/p = ±10% for Various Injection Phases**

ϕ_o (degrees)	g_α (G/cm)	Δt_i (ps)	Δt_f (ps)	$\langle p_f \rangle$ ($m_e c$)	Δp_f ($m_e c$)
-25	313.36	2.641	1.230	76.858	1.489
-20	314.08	2.580	1.193	81.339	1.416
-15	314.60	2.536	1.162	85.082	1.340
-10	314.90	2.511	1.137	88.104	1.257
-5	315.11	2.494	1.116	90.403	1.182
0	315.22	2.485	1.096	91.994	1.110
5	315.07	2.497	1.079	92.899	1.034
10	314.80	2.520	1.063	93.127	0.964
15	314.40	2.553	1.046	92.701	0.918
20	313.81	2.603	1.029	91.649	0.973
25	313.01	2.670	1.011	90.000	1.087
30	312.00	2.757	0.991	87.800	1.201
35	310.68	2.871	0.971	85.085	1.320
40	308.92	3.026	0.945	81.909	1.431
45	306.67	3.326	0.916	78.333	1.537

4.3.3 Optimizations for Various Current Densities

To obtain predictions of the maximum peak currents that might be obtained with the SSRL system, I have done a series of optimizations for $(\Delta p/p)_i = \pm 10\%, \pm 5\%$ and $\pm 2.5\%$ using MASK-generated initial longitudinal distributions for $E_{p2} = 75$MV/m and $0 \leq J \leq 80$A/cm^2. Since the initial longitudinal distribution is affected by space-charge in the gun, it is necessary to do the optimization for each current level. I chose $\phi_o = 15°$ as a compromise between minimum bunch length, maximum momentum gain, and minimum momentum spread. As before, I assumed 45 MeV as the linac energy gain. The results are summarized in Table 4.4 and in Figures 4.10 through 4.12. (Note that the data points in the figures are connected as an aid to the eye,

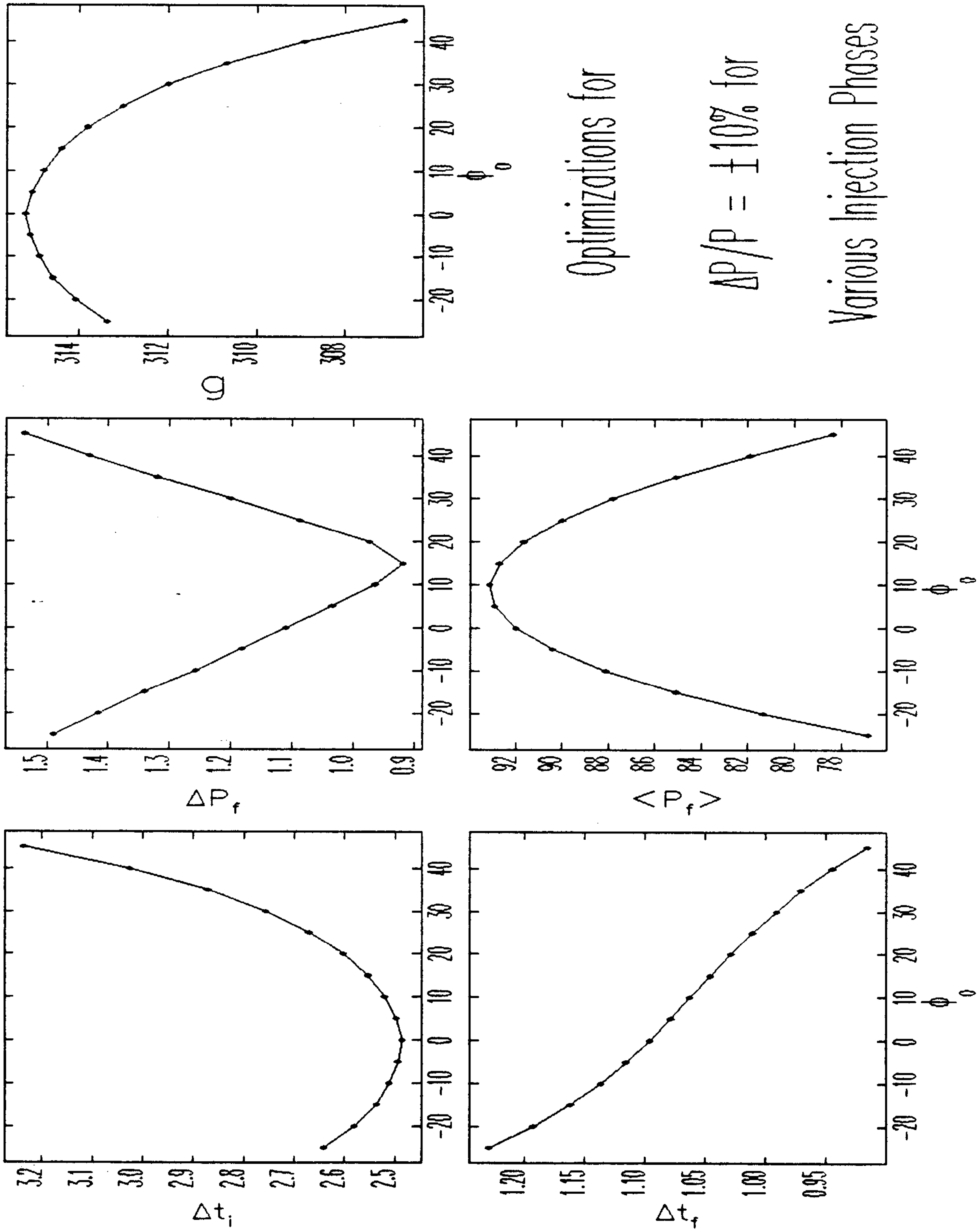

Figure 4.9: Optimization for a Short Bunch at the Linac Exit for Various ϕ_o

and not to indicate any assumed variation in the quantities between data points.)

Table 4.4: **Optimizations for Various Cathode Current Densities**

J (A/cm^2)	g_α (G/cm)	Δt_f (ps)	$\Delta t_{f,mad}$ (ps)	$\langle p_f \rangle$ ($m_e c$)	Δp_f ($m_e c$)	$\Delta p_{f,mad}$ ($m_e c$)	Q (pC)	$\langle I \rangle$ A
$(\Delta p/p)_i = \pm 10\%$								
0.2	313.20	1.070	0.292	92.737	0.906	0.263	2.3	2.1
10	314.36	1.097	0.278	92.700	0.922	0.262	110.9	101.1
20	315.20	1.121	0.287	92.661	0.951	0.267	217.8	194.3
40	318.61	1.193	0.277	92.630	0.979	0.265	416.6	349.2
80	321.28	1.272	0.315	92.573	1.027	0.275	762.8	600.7
$(\Delta p/p)_i = \pm 5\%$								
0.2	313.40	0.879	0.183	92.896	0.556	0.130	1.7	1.9
10	318.51	0.685	0.142	92.879	0.537	0.128	80.3	117.2
20	318.30	0.802	0.157	92.842	0.577	0.138	155.6	194.0
40	329.60	0.567	0.100	92.850	0.540	0.128	289.3	510.2
80	339.68	0.494	0.090	92.850	0.531	0.126	501.6	1015.4
$(\Delta p/p)_i = \pm 2.5\%$								
0.2	293.80	0.531	0.100	92.949	0.280	0.066	1.1	2.1
10	303.48	0.475	0.084	92.943	0.276	0.066	50.4	106.1
20	309.94	0.432	0.086	92.934	0.278	0.069	94.6	219.0
40	325.18	0.457	0.086	92.953	0.262	0.065	162.8	356.2
80	335.18	0.409	0.087	92.960	0.281	0.062	260.7	637.4

4.3.4 Effects of Transport Aberrations

These predictions of high peak currents neglect space-charge forces in the gun-to-linac transport line and in the linac itself. They also neglect the effects of non-chromatic t_{5jk} and u_{5jkl} terms ("aberrations") in the alpha-magnet, and of field errors in the alpha-magnet (see Chapter 3). Other effects that are not included in the analysis are wake-fields in the accelerator section. In Chapter 3, I discuss the effect of field errors, and show that the effect of field errors on r_{5j} matrix elements is small, from which I conclude that the ability of the alpha-magnet to compress the bunch is unaffected by field errors.

To evaluate the effects of space-charge, both in the GTL and in the accelerator

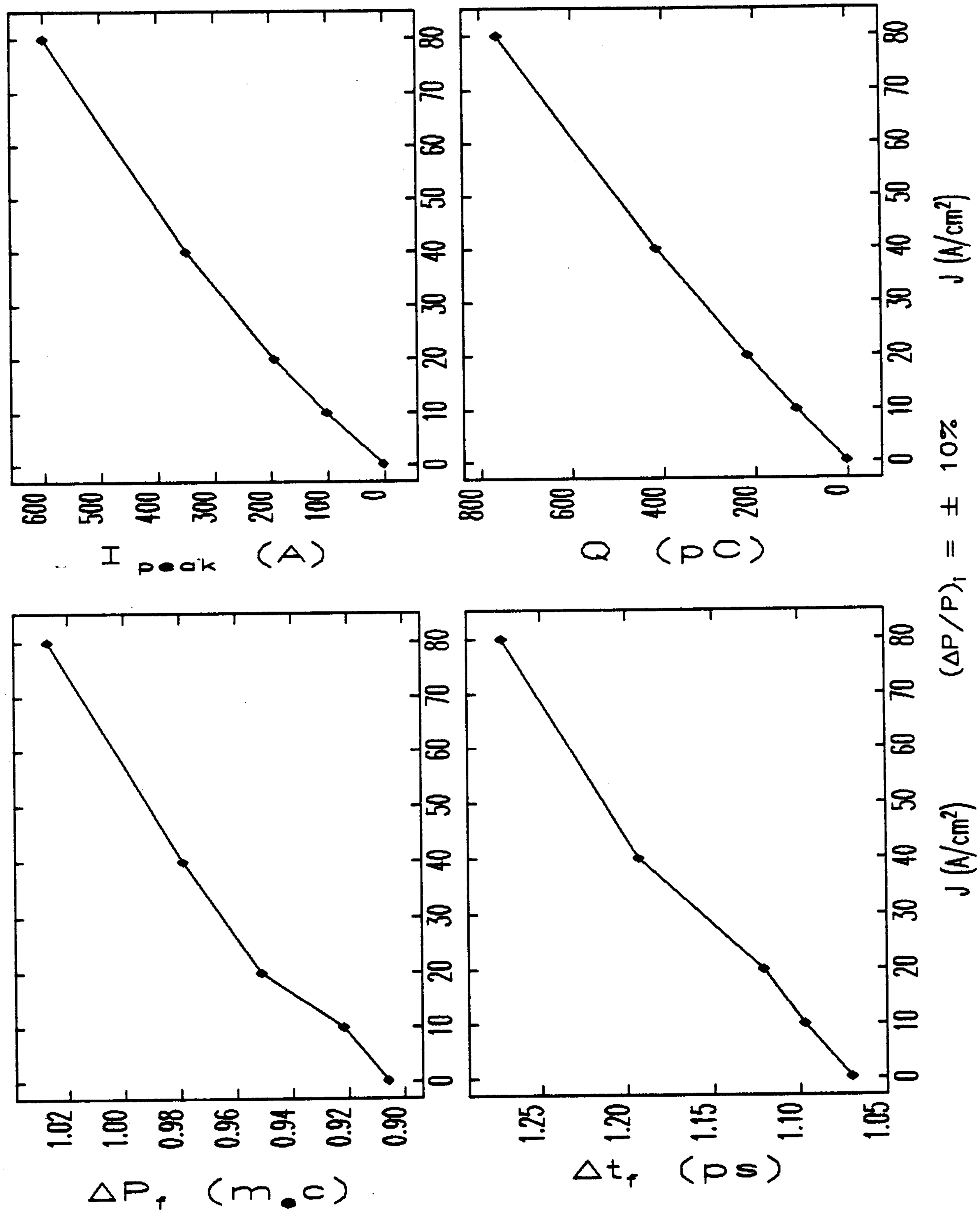

Figure 4.10: Results of Optimized Compression for Various Cathode Current Densities, for $(\Delta P/P)_i = \pm 10$ %

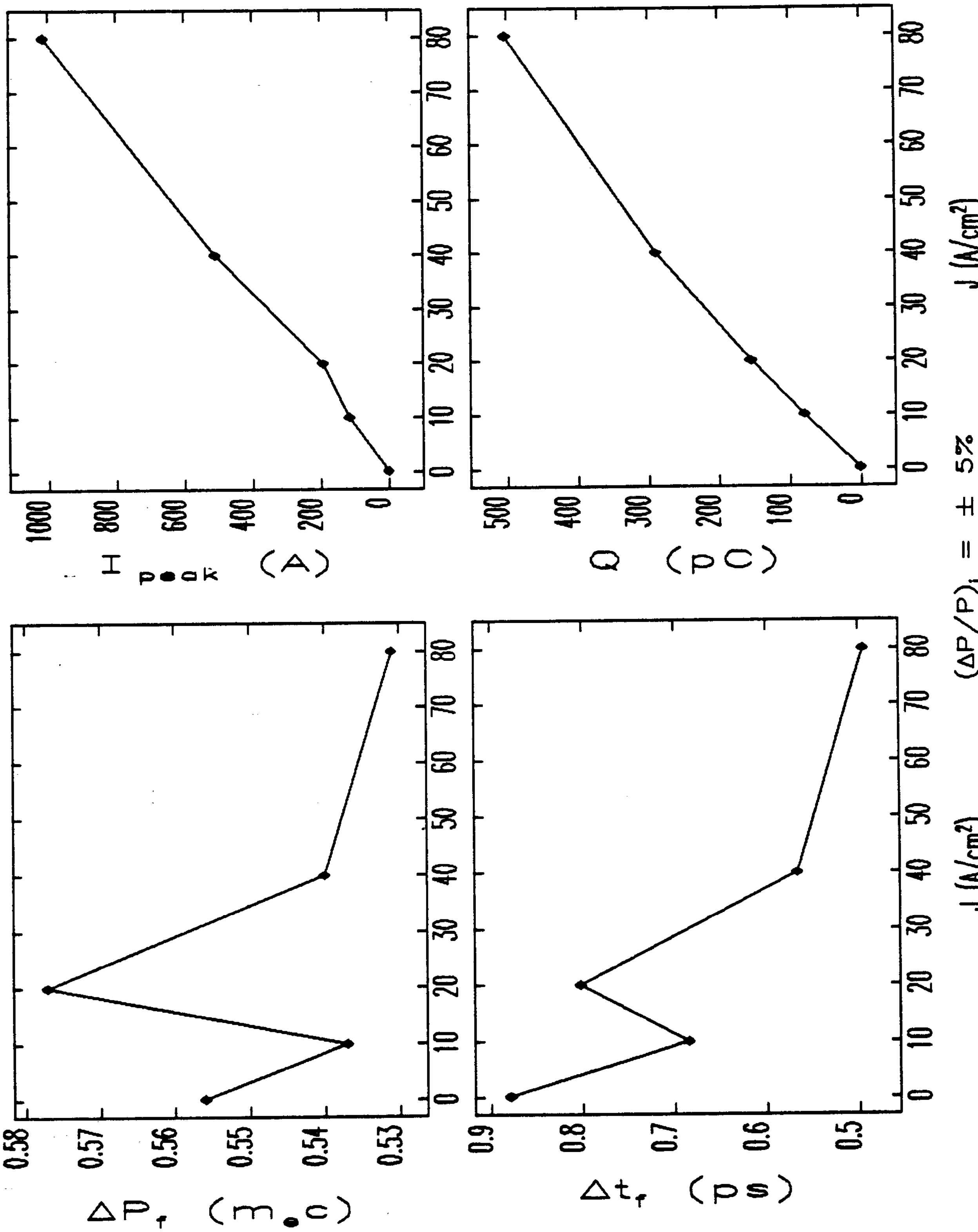

Figure 4.11: Results of Optimized Compression for Various Cathode Current Densities, for $(\Delta P/P)_i = \pm 5$ %

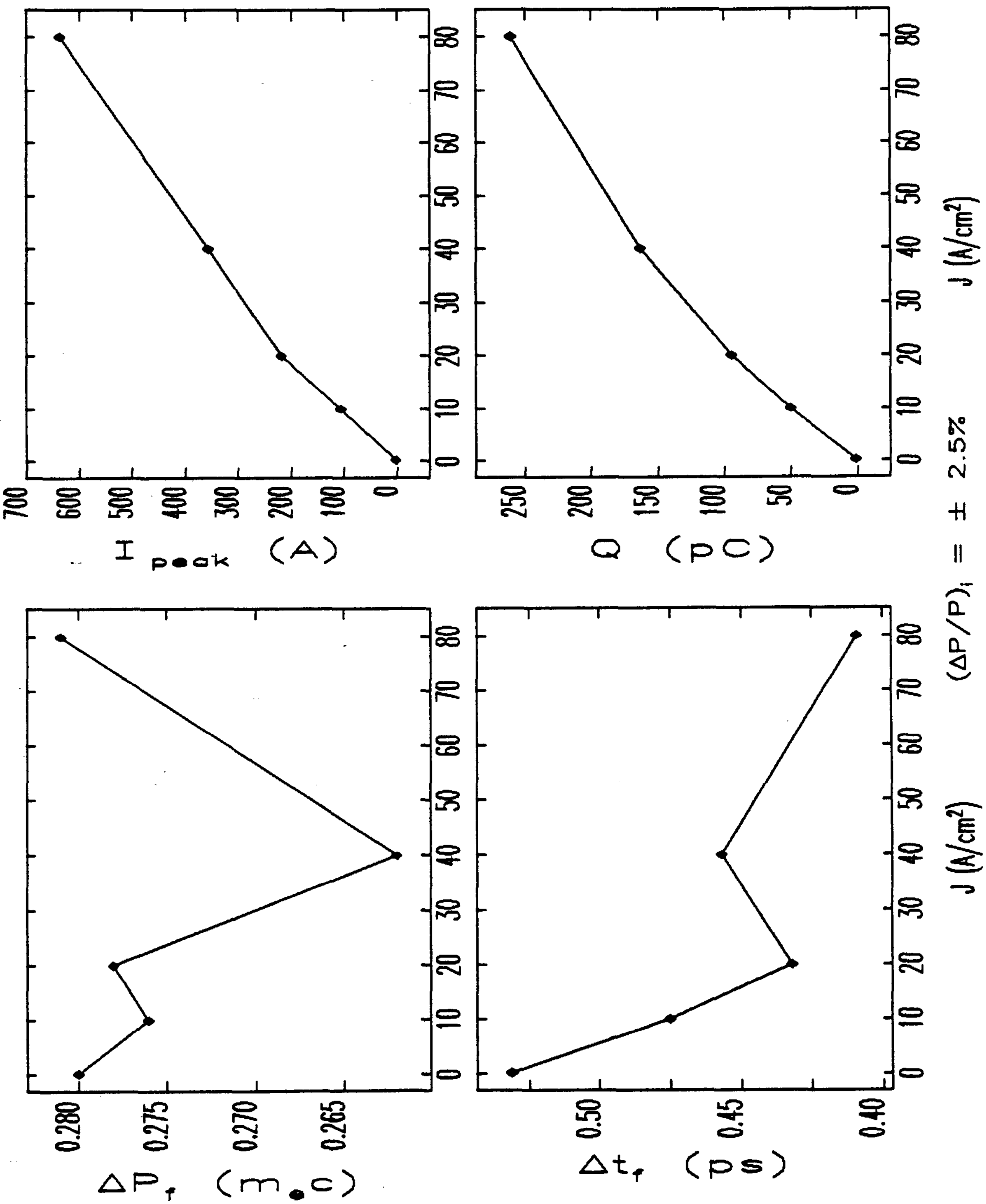

Figure 4.12: Results of Optimized Compression for Various Cathode Current Densities, for $(\Delta P/P)_i = \pm 2.5$ %

section, it would be necessary to employ a program such as PARMELA that is capable of simulating beam-transport with space-charge. Unfortunately, PARMELA does not include alpha-magnets, nor does time permit me to modify the program to remedy this deficiency (more would be required than simply inserting the transport matrix). In addition, the space-charge algorithm used by PARMELA is not well-suited to use for thermionic RF guns, where there is a large velocity spread in the beam. Finally, I have not found that PARMELA performs accurately in calculating simple test cases, such as the spread of a uniform cylindrical beam. Hence, evaluation of the effects of space-charge in the GTL must await the development of a suitable program, and will not be pursued here.

However, the program **elegant**[49] is capable of accurately simulating the GTL, ignoring space-charge. **elegant** includes chromatic aberrations (see Chapter 5) in the quadrupoles and alpha-magnet as well as other aberrations in the alpha-magnet (see Chapter 3). I will discuss the GTL optics and such issues as chromatic aberrations in Chapter 5. For the present, I simply present the results of **elegant** simulations of the GTL and the first linac section, which use the same initial phase-space data as was used in the previous calculations. That is, the **elegant** simulations took initial phase-space data generated by MASK for $E_{p2} = 75$MV/m, for a range of current densities, and for initial momentum spreads of $\pm 5\%$ and $\pm 10\%$. The results are shown in Figures 4.13 and 4.14, which are to be compared to Figures 4.10 and 4.11, respectively.

In addition to showing the peak current at the end of the linac section, I have shown the peak current at the gun exit, and the cathode current (i.e., $\pi R_c^2 J$), to illustrate the increase in peak current due to the bunching processes in the gun and GTL/linac. I have not shown the momentum spread, in order to use the space for other quantities, and because it is essentially the same as the previous results.

One sees that the peak currents predicted by **elegant** are considerably less than those obtained previously. The reason is that path-length aberrations in the GTL increase the broadness of the momentum versus time curves, making compression to very short bunches more difficult. In addition, the transmission through the first section is only 70% (particles are lost on the approximately 18 mm diameter apertures between linac cells), which reduces the amount of charge reaching the end of the

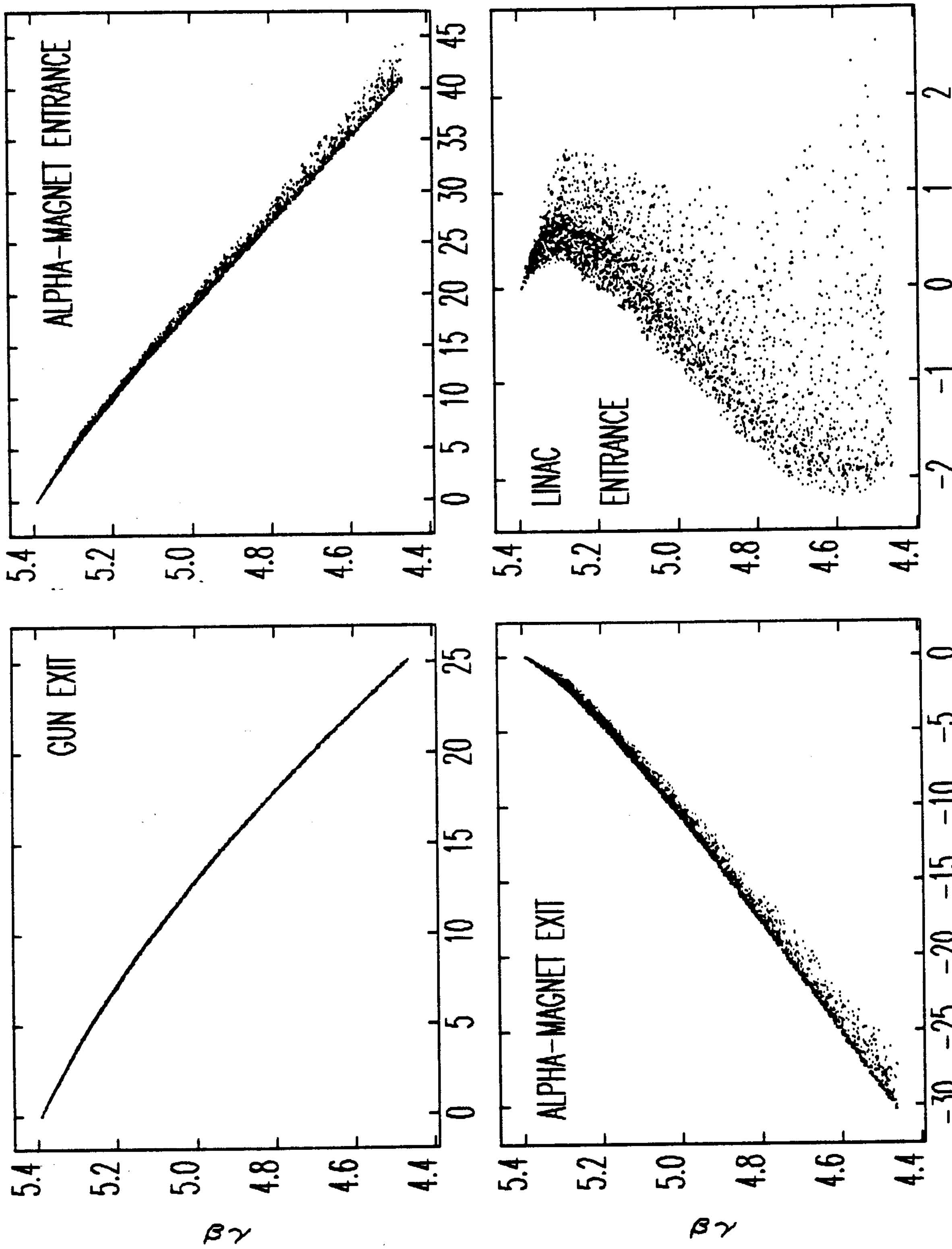

Figure 4.13: **elegant**/MASK Results after First Accelerator Section, for Various Cathode Current Densities and $E_{p2} = 75$MV/m, for $(\Delta P/P)_i = \pm 10$ %

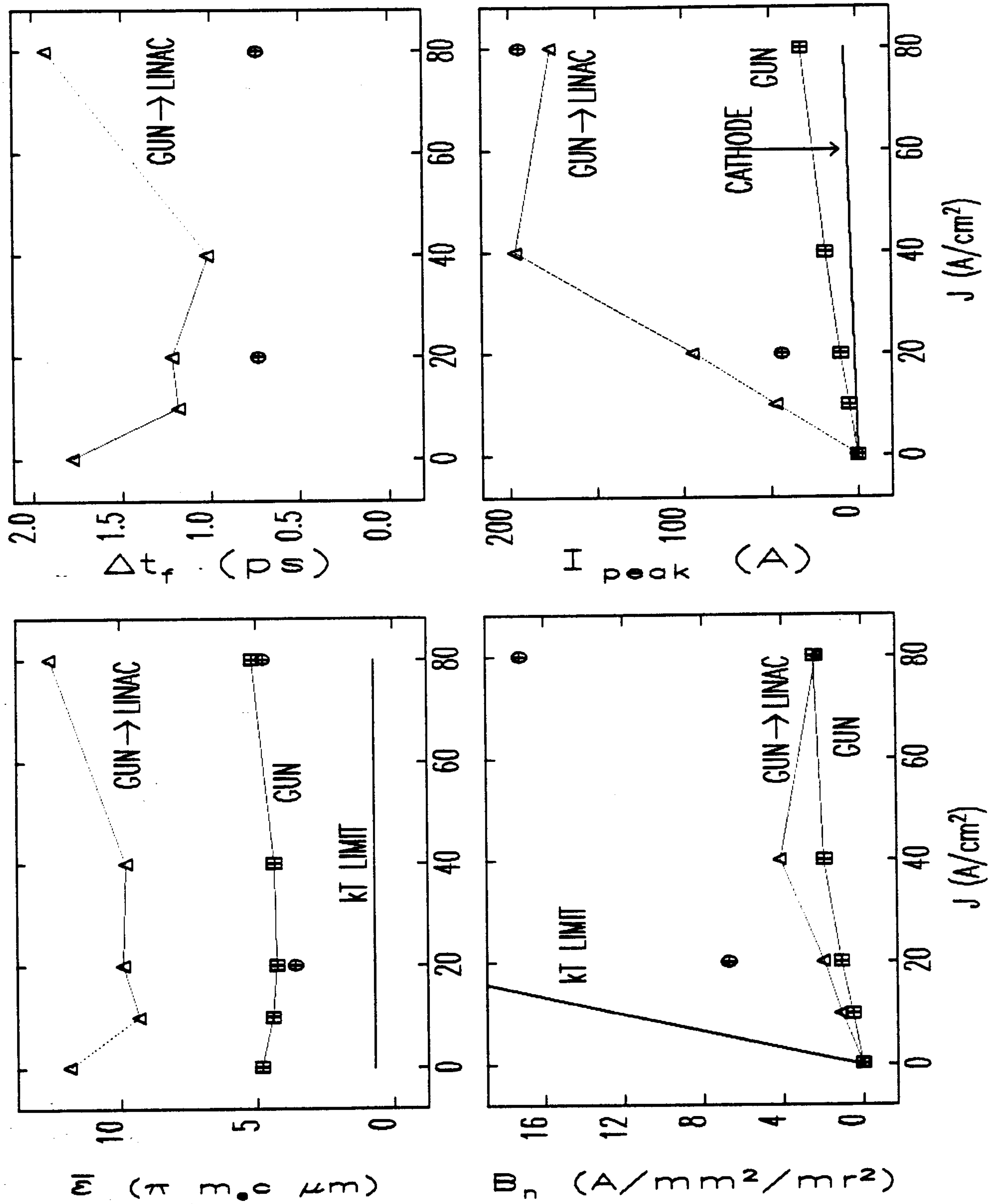

Figure 4.14: **elegant**/MASK Results after First Accelerator Section, for Various Cathode Current Densities and E_{p2} = 75MV/m, for $(\Delta P/P)_i = \pm 5$ %

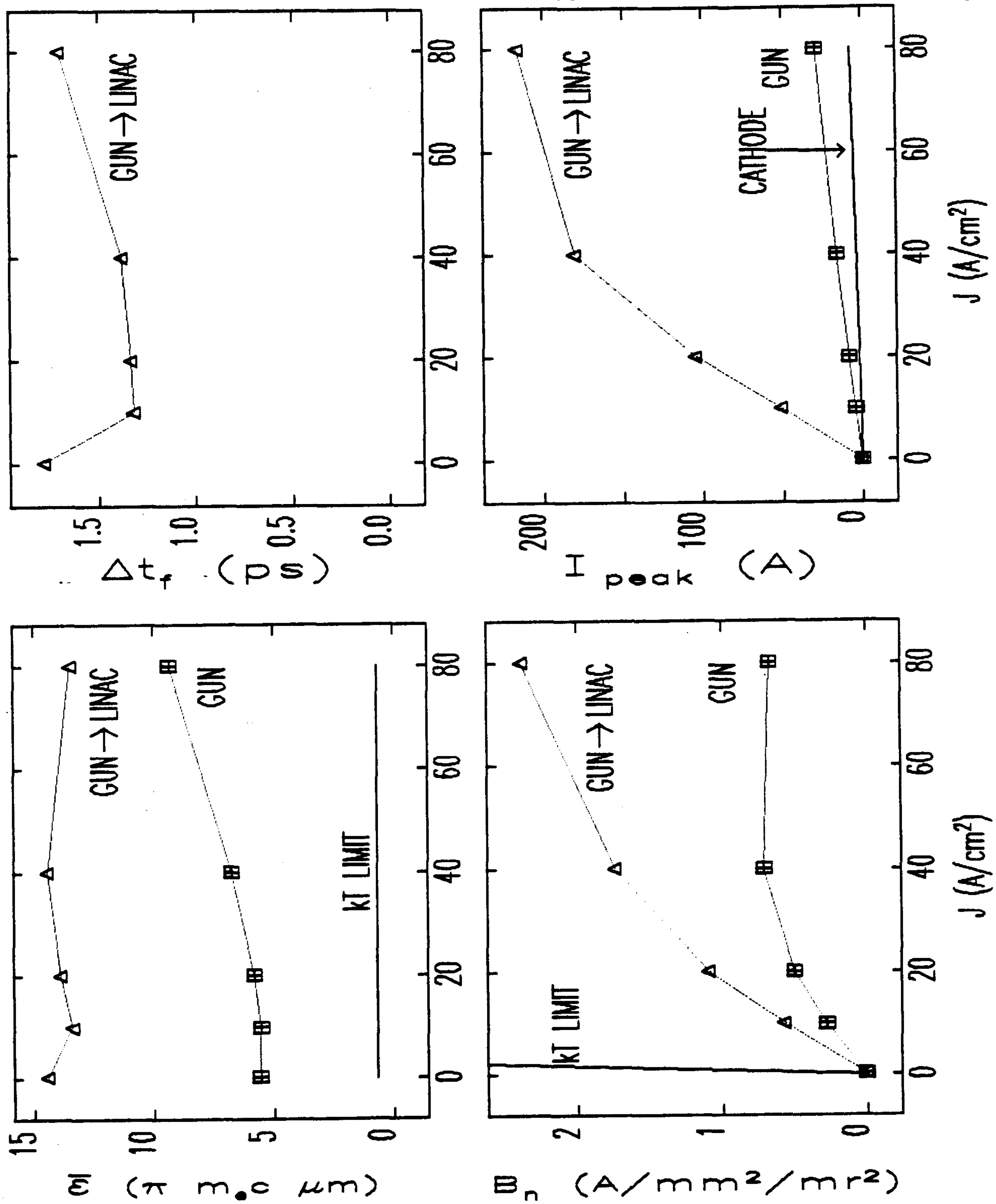

Figure 4.15: Longitudinal Phase-Space at Various Points in the GTL (`elegant`/MASK results for $E_{p2} = 75$MV/m, $J = 10$A/cm^2, and $(\Delta P/P)_i = \pm 10$ %).

linac. Figure 4.15 shows the evolution of the longitudinal phase-space in the GTL, for $\mathrm{J} = 10\mathrm{A/cm}^2$ and $\Delta\mathrm{P/P} = \pm 10\%$. As one would expect, the bunch length at the alpha-magnet entrance is greater than that at the gun exit, due to the higher velocity of the lead particles in the bunch.

The broadening of the longitudinal phase space is due to path-length-affecting aberrations in the quadrupoles and drift spaces between the gun and alpha-magnet. To see that this is reasonable, note that for a drift space of length $\mathrm{L_o}$, the path length traveled by a particle with non-zero slope is

$$\mathrm{L} = \mathrm{L_o}\sqrt{1 + \mathrm{x}'^2 + \mathrm{y}'^2} \approx \mathrm{L_o} + \frac{\mathrm{L_o}}{2}(\mathrm{x}'^2 + \mathrm{y}'^2). \tag{4.40}$$

At the gun exit, $\mathrm{x}'_{\mathrm{rms}} = \mathrm{y}'_{\mathrm{rms}} \approx 10$ mrad, and the straight-line distance from the gun exit to the alpha-magnet entrance is 60 cm. The path-length increase for $\mathrm{x}' = \mathrm{x}'_{\mathrm{rms}}$ and $\mathrm{y}' = \mathrm{y}'_{\mathrm{rms}}$ is 60μm, which corresponds to a time delay of 0.2 ps. Since there are particles in the beam with x' and y' the several times the RMS value, the broadening seen is larger than this estimate. As a result of such aberrations, the phase-space at the linac entrance differs considerably from the results show in Figure 4.8, because the latter results did not include any consideration of transverse motion.

Figures 4.13 and 4.13 also show the normalized RMS emittance and brightness at the end of the first linac section, as well as results at the gun exit, for comparison with those at the end of the linac. Recall that the emittance is defined as

$$\varepsilon_{\mathrm{n,x}} = \pi \mathrm{m_e c}\sqrt{\langle \mathrm{x}^2\rangle\langle \mathrm{p_x^2}\rangle - \langle \mathrm{p_x x}\rangle^2} \tag{4.41}$$

and the brightness as

$$\mathrm{B_n} = \frac{2\mathrm{I_{peak}}}{\varepsilon_{\mathrm{n,x}}\varepsilon_{\mathrm{n,y}}}(\pi \mathrm{m_e c})^2. \tag{4.42}$$

The emittance shown in the Figures is the geometric mean of the emittances for the x and y planes, $\bar{\varepsilon_{\mathrm{n}}} = \sqrt{\varepsilon_{\mathrm{n,x}}\varepsilon_{\mathrm{n,y}}}$.

The emittance at the end of the linac section is larger than that at the gun exit, but not as large as the emittance at the entrance to the linac. The emittance is "filtered" in the linac because particles with large transverse amplitudes are lost on the linac disc apertures. Put another way, the emittance numbers do not refer to the same particles, since 30% are lost. One sees that the emittance depends only weakly on the current density; this is due to the overwhelming effect of chromatic aberrations. The emittance at the entrance to the linac is about twice that at the end of the section. These points are discussed further in Chapter 5.

In addition to showing the simulation results for the emittance, I have shown the thermal limit on the emittance for a cathode of $R_c = 3$mm, using[16]

$$\varepsilon_{n,x} = \varepsilon_{n,y} = \frac{1}{2} R_c \sqrt{\frac{kT}{m_e c^2}}, \tag{4.43}$$

where T is the cathode temperature, which is 1200°K for the SSRL gun. One sees quite clearly that the thermal limit is far from being approached: the emittance is dominated by RF focusing, non-linear fields in the gun, and chromatic aberrations in the GTL.

Figure 4.14 also shows two data points obtained by simulating the gun with a smaller emitting area on the cathode. (These appear as crossed circles in the graphs.) In particular, an emitter radius of 1.5 mm was used, with the physical cathode size kept at 3mm radius. In effect, the region from $r = 1.5$mm to $r = 3$mm was taken to be a "dead region" on the cathode. In this situation, particles are emitted much closer to the axis in the gun, so that non-linear fields in the gun have less of an effect, resulting in a smaller emittance. In addition, the smaller emittance leads to smaller effects from path-length-affecting aberrations in the GTL, so that shorter bunch-lengths are achieved. While the amount of charge drops due to the decrease in emitting area, this is balanced to some extent by the shorter bunch-length, so that the peak current at $J = 80\text{A/cm}^2$ is increased. Because of the strong effect on the emittance, the brightness is dramatically increased. These results make a strong case for operating the gun with such a cathode, especially since the cathode is currently operated well below its maximum current density, meaning that a reduced emitting area could be used with no loss of total charge.

4.3.5 Comparison with Other Injectors

The data of Figures 4.13 and 4.14 permit comparison of the predicted performance of the SSRL preinjector (i.e., the RF gun, GTL, and linac) with other RF-linac-based preinjectors. In order to do this, I have reviewed recent literature giving parameters of existing and planned injectors. There is always the chance of confusion in any such compilation, especially since many authors do not state their definition of the emittance or bunch length. Where doubt exists, I have assumed that the quoted emittance is the 4-σ or "edge-emittance" and that the bunch length refers to 90-95% of the beam, since these appear to be the most commonly used definitions.

One extremely useful resource in this regard was C. Travier's review article on RF guns[14], which gives extensive performance data for RF guns and state-of-the-art DC gun systems (i.e., those with high-performance guns and multiple subharmonic bunchers). I have also taken data from T. I. Smith's review[46], which lists several systems planned for or already in use as FEL drivers; these are not necessarily state-of-the-art systems. (Where Travier and Smith differ on the same system, I have used Travier's data, which is more recent.) I also show data points for several other systems that are intended for FEL use[73, 74, 75] as well as SLAC's SLC[76] (including damping rings) and the original SLAC injector[48].

Note that I will compare *injectors*, rather than *guns*. From an applications-oriented viewpoint, this is the most appropriate comparison to make among systems using various types of guns, since it includes all of the effects that come into play when one actually makes use of the beam from a gun. It also avoids issues such as whether a multi-cell thermionic RF gun should be compared to a DC gun with prebunchers, given that the multi-cell RF gun is in some sense a combined gun and prebuncher.

The data for DC-gun-based and microtron-based systems are in Table 4.5, while those for RF guns are in Table 4.6. Two data points are listed for the SSRL system. Both are for $E_{p2} = 75$MV/m and f=0.05, but one assumes $J = 40$A/cm^2 with $R_c = 3$mm, while the other assumes $J = 80$A/cm^2 with $R_c = 1.5$mm. (These are both consistent with less than 4 MW incident RF power, which is the anticipated upper limit that will be supplied to the gun after some recent, but untested, hardware upgrades.) Figure 4.16 shows some of this data in graphical form, with addition points supplied for the SSRL system, as explained on the graph.

One sees that the SSRL system is predicted to perform quite well in terms of peak current and brightness, achieving levels comparable to those achieve by much more sophisticated and complicated systems. One also sees, however, that the high brightness and high peak current are achieved by generating very short pulses, which are not appropriate to FEL work at wavelengths that are not very long compared to the electron bunch length (see Chapter 1 for a discussion).

Table 4.5: **Performance of DC-Gun and Microtron- Based Injectors**

Project	$\bar{\varepsilon}_n$ $\pi \cdot m_e c \cdot \mu m$	I_{peak} A	Q nC	δt ps	B_n $A/mm^2/mr^2$
SLC (1986)[76]	30	2400	8	3.3	5.3
SLC 2[14]	75	580	10.4	18	0.21
SLC 1[14]	43	430	7.7	19	0.47
Boeing[14]	13	350	4.9	14	4.2
LANL[14]	60	300	9.0	30	0.17
ALS[14]	40	200	4.0	20	0.25
CLIO[14]	7.5	100	1.5	15	3.46
Trieste FEL[74]	50	15	0.15	10	0.012
UK FEL[46]	13	10	-	-	0.12
Frascatti[75]	1.4	6	-	-	6.1
SCA/TRW[46]	1.3	4	-	-	4.73
Orig.SLAC[48]	5.7	0.3	-	-	0.018
NIST-NRL[73]	5	0.3	14	15	0.024

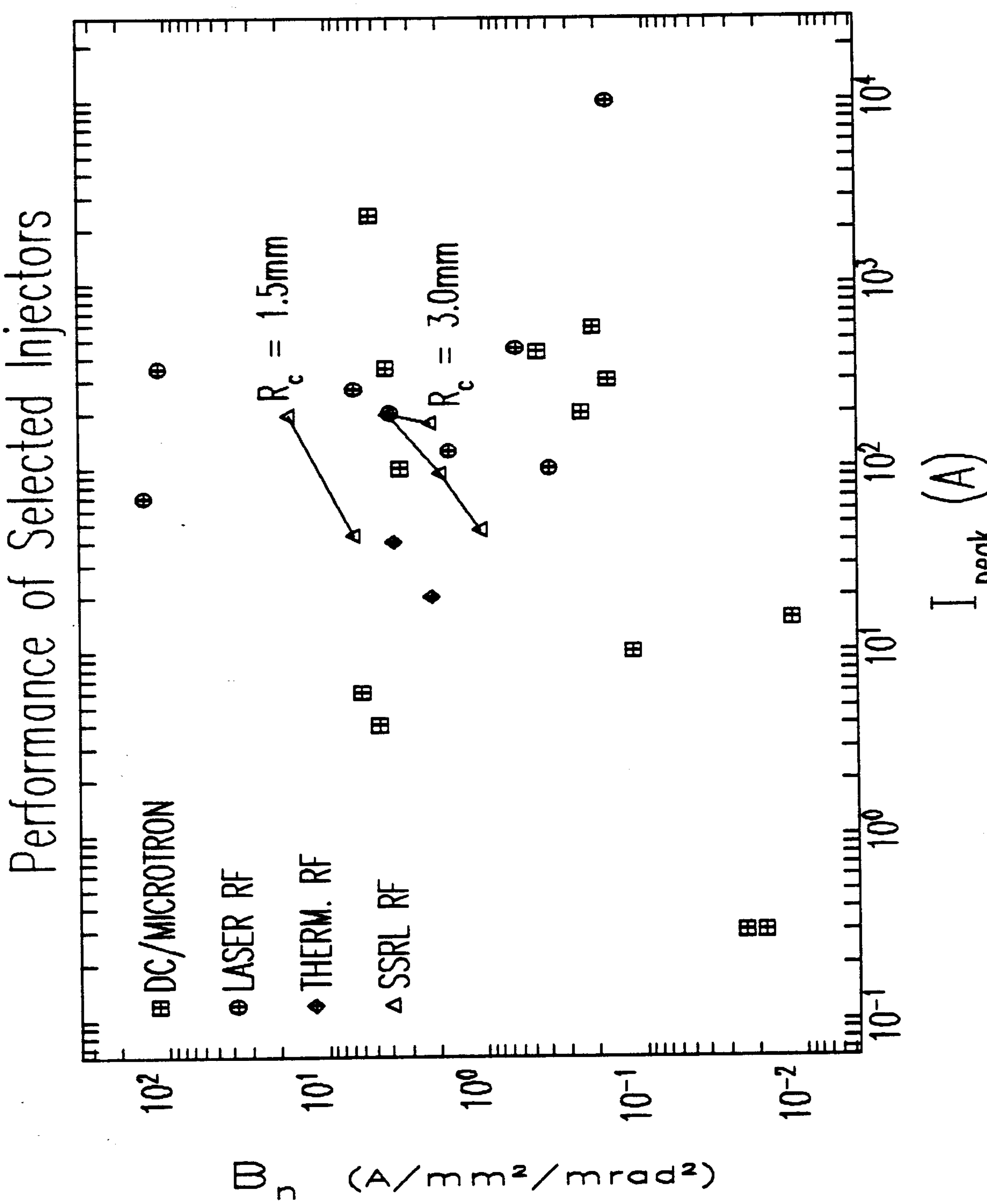

Figure 4.16: Brightness and Peak Current for Various Injectors

Table 4.6: **Performance of RF-Gun-Based Injectors**

Project	$\bar{\varepsilon}_n$ $\pi \cdot m_e c \cdot \mu m$	I_{peak} A	Q nC	δt ps	B_n $A/mm^2/mr^2$	type
ANL[14]	340	$10 \cdot 10^3$	100	8	0.17	laser
CERN[14]	37.5	450	9	30	0.64	laser
LANL:						
AFEL[14]	2.5	350	5	16	112	laser
HIBAF[14]	9.0	270	4	15	6.7	laser
PHASE I[14]	10.0	200	11	70	4.0	laser
SSRL:						
3mm, $40A/cm^2$	9.5	196	0.2	1.0	4.4	therm.
1.5mm, $80A/cm^2$	4.8	144	0.2	0.7	17.2	therm.
BNL[14]	12.0	125	1	8	1.7	laser
CEA[14]	22.5	100	10	100	0.4	laser
DFELL[14]	1.0	70	0.17	2.5	140	laser
DFELL[14]	4.6	20-40	.05-.1	2-3	1.9-3.8	therm.
IHEP[14]	4.3	10-20	.080-.1	4-5	1.1-2.2	therm.